

Study on spontaneous exciton dissociation in polar organic semiconductor solid-state films

山中, 孝彦

<https://hdl.handle.net/2324/5068189>

出版情報 : Kyushu University, 2022, 博士 (工学) , 課程博士
バージョン :
権利関係 :

2022

Doctor thesis

Study on spontaneous exciton dissociation in polar organic
semiconductor solid-state films

Takahiko Yamanaka

Department of Chemistry and Biochemistry
Graduate School of Engineering
Kyushu University

Table of contents

Chapter 1 Introduction	5
1-1. Background	6
1-1-1. Emitters for organic light-emitting diodes (OLEDs)	6
1-1-2. Fundamental photophysics of TADF molecules	8
1-1-3. Exciton characteristics in organic molecules	10
1-1-4. Exciton binding energy	12
1-1-5. Theory of exciton dissociation	13
1-1-6. Exciton dissociation in OPVs	16
1-1-7. Organic long persistent luminescence (OLPL)	18
1-1-8. Molecular polarization in solid-state film	20
1-2. Purpose and outline of this thesis	23
References	25
Chapter 2 Slow recombination of spontaneously dissociated organic fluorophore excitons	31
2-1. Introduction	32
2-2. Results and discussion	33
2-2-1. Photo-physical properties of TPA-DCPP	33
2-2-2. External-electric-field-modulated TRPL	37
2-2-3. The role of SOP in exciton dissociation event	43
2-3. Summary	47
2-4. Sample preparation and experimental methods	48
2-4-1. Materials	48
2-4-2. Sample fabrication	48

2-4-3. Measurement of photoluminescence properties.....	49
2-4-4. External-electric-field-modulated luminescence characterization.....	49
2-4-5. Displacement current measurement.....	49
References	50
Chapter 3 Significant role of spin-triplet state for exciton dissociation in organic solids.....	52
3-1. Introduction	53
3-2. Results and discussion.....	56
3-3. Summary	76
3-4. Sample preparation and experimental methods	77
3-4-1. Materials	77
3-4-2. Sample fabrication	77
3-4-3. Measurement of fundamental PL properties.....	78
3-4-4. TRPL measurement and PL intensity measurement under electric fields ...	78
3-4-5. Fluorescence lifetime measurements under an electric field	79
3-4-6. DCM characterization.....	79
3-4-7. IQE measurements	79
References	80
Chapter 4 Electron lifetime of over one month in disordered organic solid-state films	83
4-1. Introduction	84
4-2. Result and discussion	86
4-2-1. Characterization of charge carrier lifetime	86
4-2-2. Evaluation of spatial storage ability.....	98

4-2-3. High-speed pulse-driven OLED using charge accumulation.....	105
4-3. Summary	112
4-4. Sample preparation and experimental methods	112
4-4-1. Materials	112
4-4-2. Sample preparation	113
4-4-3. DCM characterization.....	113
4-4-4. Pulse-driven EL measurement	114
4-4-5. EL Imaging	114
References	115
Chapter 5 Summary	118
5-1. Summary of this thesis	119
5-2. Future perspectives.....	120
References	126
Appendix	127
Publication lists	128
Acknowledgements	129

Chapter 1

Introduction

1-1. Background

1-1-1. Emitters for organic light-emitting diodes (OLEDs)

An organic fluorophore that can emit bright emission after receiving external energy such as photons plays an essential role in various scenes of our daily life and has been used for a wide variety of applications in displays, lighting devices, X-ray measurement apparatus¹, fluorescence microscopies², and dye lasers³.

An organic light-emitting diode (OLED) is known as one of the representative devices including the organic emitters. Since C. W. Tang and S. A. VanSlyke successfully demonstrated an advanced OLED having high luminance at a low driving voltage of ~5 V by employing two thin-film layers in 1987⁴, OLEDs have been significantly developed by not only academia but also industries aimed at the commercialization for display and lighting applications⁵. To apply OLEDs to such applications, the emitter exhibiting high photoluminescence (PL) quantum yield (PLQY) in whole visible wavelengths are essentially required⁶⁻⁹.

In OLEDs, the light emission, i.e., electroluminescence (EL), occurs via the recombination of a hole and an electron. Therefore, the external EL quantum efficiency (EQE) defined as the ratio of injected charge carriers to emitted photons is one of the critical parameters for the evaluation of OLED performances. EQE is given by

$$\eta_{EQE} = \gamma \times \eta_r \times \Phi \times \eta_{OC}$$

where γ is a carrier balance factor of injected carriers (holes and electrons), η_r is the ratio of radiative exciton production, Φ is PLQY defined as the number of emitted photons as a fraction of the number of absorbed photons, and η_{OC} is light outcoupling efficiency. Here, η_r is limited by an excited spin-state of organic emitters such as fluorescence and phosphorescence. Injected holes and electrons have a random spin state, and the

recombination events yield two types of excited spin-states; a lowest singlet excited state (S_1) and a lowest triplet excited state (T_1) with the branching ratio of 1:3. Since the radiative transition from a T_1 to a ground state (S_0) is generally spin-forbidden, the 75% of electrically generated triplet excitons are nonradiatively decay to the ground state. Therefore, even if the emitter possesses an ideal PLQY of 100% for fluorescence, the η_r is limited to only 25% in OLEDs.

To overcome this theoretical limitation, the room-temperature phosphorescent emitter was proposed, in which radiative transition from T_1 to S_0 is allowed with the help of the heavy atom effect. In 1998, M. A. Baldo et al. demonstrated the efficient phosphorescent OLEDs using a Pt complex, 2,3,7,8,12,13,17,18-octaethyl-21H,23H-porphine platinum(II) (PtOEP), having good PLQY even at room temperature¹⁰. Later, the performance of phosphorescent OLED was drastically improved by employing an iridium complex Ir(ppy)₃¹¹, realizing nearly 100% internal EL quantum efficiency (IQE)¹². In recent years, strikingly a novel emitter of thermally-activated delayed fluorescence (TADF), which can also realize 100% electron-photon conversion, has been demonstrated using simple aromatic compounds. TADF efficiently promotes upconversion of triplets into an S_1 state even with the thermal energy at room temperature¹³. The transition between the different electronic spin-states of a triplet and a singlet is generally forbidden. However, by taking account of the perturbation theory, intersystem crossing (ISC) and reverse intersystem crossing (RISC) processes can be allowed with the proper molecular design¹⁴.

The first-order mixing coefficient between singlet and triplet excited states (λ) is given by

$$\lambda \approx \frac{H_{\text{SOC}}}{\Delta E_{\text{ST}}}$$

where ΔE_{ST} is the energy splitting between singlet and triplet excited states, and H_{SOC} is a spin-orbit coupling (SOC) element. According to this equation, the small ΔE_{ST} and large H_{SOC} are necessary to facilitate the RISC process. Here, the magnitude of ΔE_{ST} is dependent on the exchange integral between the highest occupied molecular orbital (HOMO) and lowest unoccupied molecular orbital (LUMO). Since the H_{SOC} values are described as an overlap integral between an initial ground state and a final excited state, the spatial separation of HOMO and LUMO provides the requirement for realizing a large λ . However, this strategy simultaneously causes the reduction of an oscillator strength which determines the luminous efficiency of molecules. Here, the oscillator strength (f) is proportional to the square of a transition dipole moment (TDM) which is enhanced in accordance with the expansion of the spatial overlap between HOMO and LUMO. Therefore, a moderate overlap between HOMO and LUMO is required to obtain emissive molecules. To obtain the balanced λ and f , a combination of electron-donating (D) and electron-accepting (A) units is often adopted in the design of TADF molecules¹⁵. In these molecular systems, the S_1 and T_1 states generally form a charge transfer (CT) state which possesses lower energy than the locally excited (LE) triplet state of a D or an A unit.

1-1-2. Fundamental photophysics of TADF molecules

The molecular structure and photophysical property of 2,4,5,6-tetra(9H-carbazol-9-yl)iso-phthalonitrile (4CzIPN), which is representative of TADF emitter¹⁶, are illustrated in **Figure 1-1**. In the transient PL (TRPL) measurement, the TADF molecule exhibits the dual components in its emission decay, i.e., prompt emission with the time constant (τ_p) of nanoseconds and delay emission with the time constant (τ_d) of microseconds, whereas only a prompt decay component is observed in conventional

organic emitters. The origin of each component can be ascribed to the radiative transition of immediate relaxation from S_1 to S_0 (k_p) and the delayed relaxation from S_1 to S_0 via multiple ISC and RISC cycles between S_1 and T_1 (k_d), respectively. The k_p and k_d are derived as below using the rate equations^{17, 18},

$$k_p = k_r^S + k_{nr}^S + k_{ISC}$$

$$k_d = k_r^T + k_{nr}^T + \left(1 - \frac{k_{ISC}}{k_r^S + k_{nr}^S + k_{ISC}}\right) k_{RISC}$$

Here, k_r^S , k_{nr}^S , k_{ISC} , k_r^T , k_{nr}^T , and k_{RISC} correspond to the rate constants of radiative emission from S_1 to S_0 , nonradiative relaxation from S_1 to S_0 , ISC from S_1 to T_1 , radiative emission from T_1 to S_0 , nonradiative relaxation from T_1 to S_0 , and RISC from T_1 to S_1 . k_{RISC} is also expressed by the Arrhenius equation,

$$k_{RISC} = A \times \exp\left(-\frac{\Delta E_{ST}}{k_B T}\right)$$

where A is a pre-factor, k_B is Boltzmann constant and T is temperature. Since the delayed emission process is an endothermic process, the lifetime of the delayed emission is much longer than the prompt emission intrinsically.

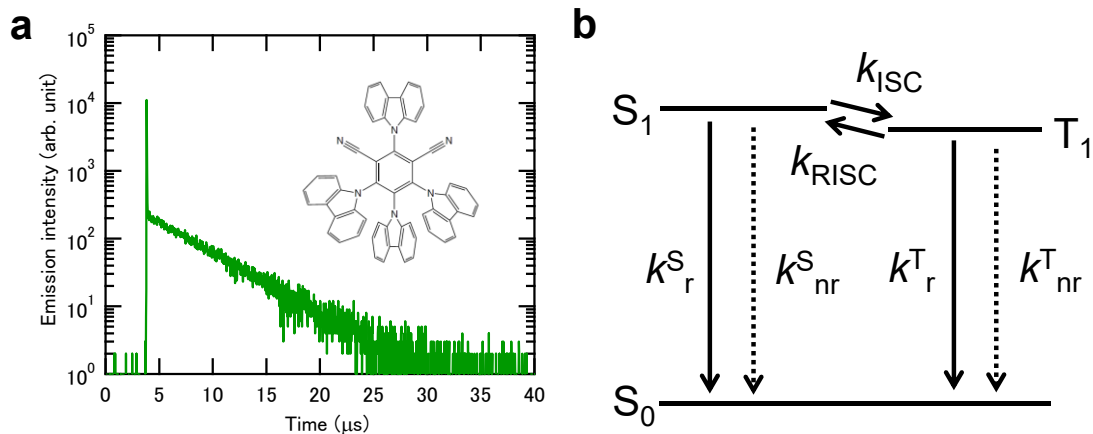


Figure 1-1. (a) PL lifetime of 4CzIPN in toluene. (b) Rate constants from singlet and triplet energy states.

The photophysical properties depicted in **Figure 1-1** are the dynamics in a liquid state, i.e., a nearly single molecular state. However, additional photophysics occurs in solid states as in the case of a solid-state film, e.g., OLEDs. For instance, the spectral redshift of emission wavelength with decreasing molecular distance is observed due to a stabilization of the excited states. Moreover, the triplet excitons generated under electrical excitation are quenched by the interaction with polaron or themselves, namely triplet-polaron quenching (TPQ) and triplet-triplet annihilation (TTA), respectively^{19, 20}. Therefore, the long-lived triplets in OLEDs cause various unwanted effects such as device degradation and EQE rolloff²¹⁻²⁴. In the recent advanced TADF molecules, a relatively fast spin-flip process between LE and CT states achieved a significantly large k_{RISC} of $\sim 10^7$ (s^{-1}), in which the suppression of EQE rolloff in OLEDs was successfully demonstrated²⁵⁻²⁹. These results indicate that the precise design of TADF excited states can improve OLED performance, and a deeper understanding of the CT excited states in TADF molecular systems will provide a novel possibility for organic semiconductor devices.

1-1-3. Exciton characteristics in organic molecules

Once a photon is absorbed by an organic molecule, an electron is excited to the upper energy level of the molecule and then an electrically bound hole-electron pair is formed. After the arbitral lifetime passed, any of the following processes occur: 1) radiative relaxation from an excited state to a ground state, 2) nonradiative relaxation via multiple vibrational relaxations with heat dissipation, 3) exciton dissociation and charge carrier generation. In typical organic molecules, while the radiative and nonradiative processes have been recognized as two distinct decay processes in their relaxation, an

exciton dissociation event has been ignored. Due to their strong Coulomb binding energy, it would be reasonable to assume such an event does not happen frequently. Here, Coulomb attraction potential V_{att} is given by³⁰,

$$V_{\text{att}} = \frac{e^2}{4\pi\epsilon_r\epsilon_0 r}$$

where e is the elementary charge, ϵ_r is a relative permittivity, ϵ_0 is the vacuum permittivity, and r is an electron-hole separation distance. The low relative permittivity ($\epsilon_r \approx 3-4$) in typical organic molecules leads to large Coulomb attraction compared to $\epsilon_r > 10$ of conventional inorganic materials. As a result, the excitons in organic molecules generally possess large binding energy that is significantly greater than the thermal energy at room temperature ($k_B T \sim 25$ meV), namely, Frenkel excitons^{31, 32}. On the other hand, the Coulomb binding energy for CT excitons should be lower than that of Frenkel excitons by virtue of a larger exciton radius, i.e., similar to Wannier excitons³³ (**Figure 1-2**). Indeed, the dissociation of CT excitons in an anthracene crystal was firstly observed in 1967³⁴ also TADF molecules are prone to form an intermolecular CT-excited state based on the spatial separation of HOMO and LUMO. Therefore, the electron-hole distance r is enlarged, and the Coulomb attraction is expected to be suppressed in the CT excited states.

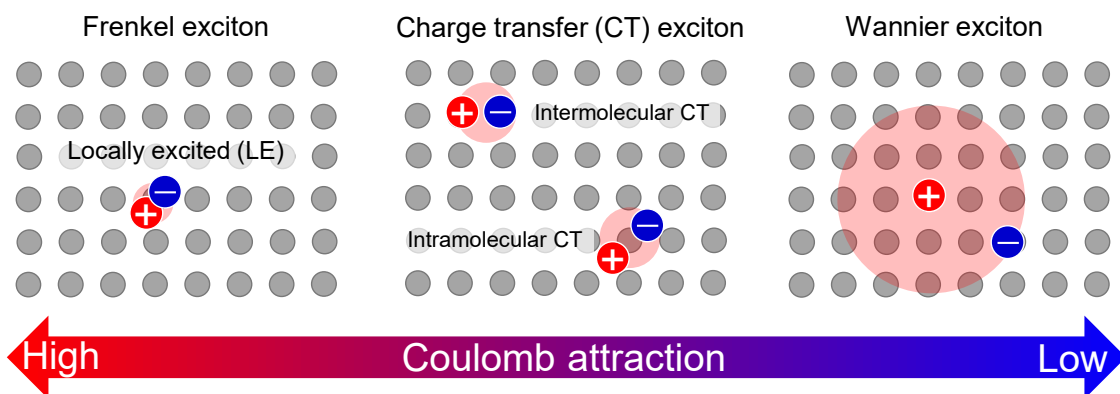


Figure 1-2. Three representative types of molecular excitons and their Coulomb binding.

1-1-4. Exciton binding energy

The exciton binding energy, E_B , is typically defined as “the energy for exciton dissociation to free carriers”, expressed by the following equation;³⁵

$$E_B = E_B^{\text{intra}} + E_B^{\text{CT}} - W$$

where E_B^{intra} is the intramolecular exciton binding energy in one molecule, E_B^{CT} is the potential energy difference between a CT excited state and the ionic state of two adjacent molecules, and W is the effect of intermolecular band structure induced by a wave function overlap of each molecule (**Figure 1-3**). E_B^{intra} can be estimated by a quantum chemical calculation as an energy difference between quasiparticle excitation (i.e., the individual excitation of electron and hole) and coupled hole-electron excitation^{36, 37}. The E_B^{CT} is approximated as the energy difference between a CT state and a charge-separated (CS) state, in which the energy of a CS state corresponds to the difference between the electron affinity of an acceptor (EA_A) and the ionization potential of a donor (IP_D)³⁸. The W means that the energy of fully dissociated charges is stabilized by the delocalization of a D or an A molecule in the view of intermolecular charge hopping. E_B is roughly estimated as the energy difference between an IP_D - EA_A gap and an optical gap. However, the binding energy is strongly influenced by ambient conditions. For instance, the effective Coulombic interaction between the hole and the electron is suppressed by dielectric screening³⁹, facilitating the reduction of the binding energy. Furthermore, for the strict discussion of the binding energy, it is necessary to consider not only the Coulomb potential but also the overall free energy, i.e., entropy contribution in Gibbs free energy.

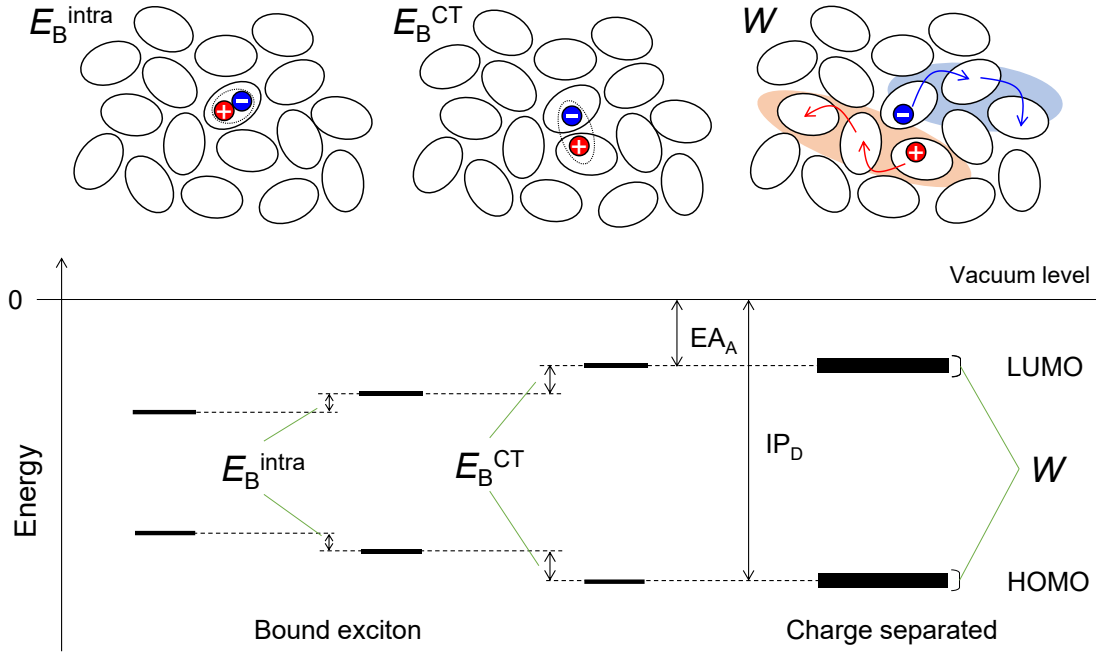


Figure 1-3. Schematic illustration and energy level diagram of exciton binding energy.

1-1-5. Theory of exciton dissociation

The photogenerated exciton must overcome the binding energy for the dissociation to the free carriers. The model which quantitatively denotes an escape probability from the Coulomb attraction was formulated by Onsager in the 1930s^{40, 41}. In this model, it is described that the competition between the dissociation of a hole-electron pair and its recombination back to the ground state depends upon the magnitude of the Coulombic attraction. Onsager proposed the definition for a Coulomb capture radius r_c (also known as Onsager radius), defined as the distance at which the Coulomb attraction energy equals the thermal energy $k_B T$, following the equation;

$$r_c = \frac{e^2}{4\pi\epsilon_r\epsilon_0 k_B T}$$

As same as the description of the exciton binding energy, the large r_c can be obtained by the low dielectric constant in organic semiconductor layers. The escape probability $P(E)$

based on the r_c is given by⁴²

$$P(E) = \exp\left(\frac{-r_c}{a}\right) \left(1 + \frac{er_c}{2k_B T} E\right)$$

where a is the initial separation of a hole-electron pair, E is the strength of the applied electric field. This equation means that the Coulomb potential barrier is electric-field dependent, and the fraction of escaping charge carriers is elevated by applying the electric field. Further, in this model, photon absorption generates a localized hole and a hot electron (or a localized electron and a hot hole) by virtue of its excess thermal energy, then the electron can move rapidly until it is stabilized at the distance a (called a thermalization length) from the localized hole. If the thermalization length is larger than the Coulomb capture radius, the dissociation of the charge carriers happens prominently. On the other hand, when the thermalization length is smaller than the Coulomb capture radius, the exciton dissociation occurs with an escape probability of $P(E)$ while the geminate recombination to reform the ground state occurs with a probability of $1-P(E)$, as shown in **Figure 1-4**. Therefore, the exciton dissociation can occur from either the vibrationally excited hot state (i.e., the Franck-Condon state) or the thermally equilibrated (geometrically relaxed) cold state.

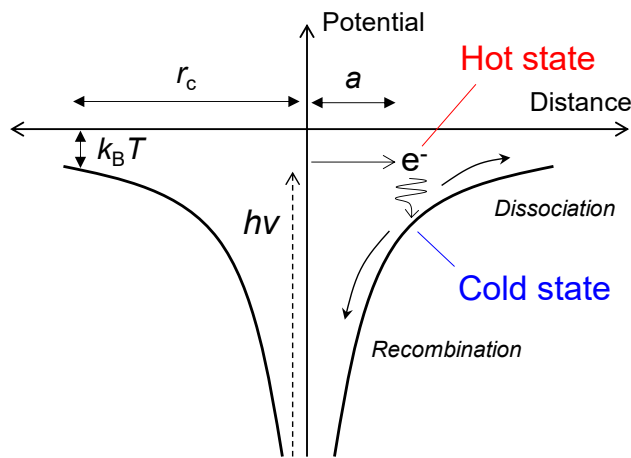


Figure 1-4. Potential energy diagram summarizing Onsager theory.

The Onsager theory was modified in 1984 by Braun, who highlighted the importance of a finite lifetime for CT states, especially in solid states⁴³. In the original Onsager model, the recombination of a hole-electron pair occurs irreversibly. However, Braun considered that this assumption is inappropriate from the basis of the decay process in CT states and redefined $P(E)$ by putting both a rate constant for dissociation ($k_{CS}(E)$) and geminate recombination back to the ground state ($k_f(E)$).

$$P(E) = \frac{k_{CS}(E)}{k_f + k_{CS}(E)} = k_{CS}(E)\tau(E)$$

where $\tau(E)$ is the lifetime of the CT state, and k_f is assumed to be field-independent for simplicity. The k_{CS} is given by an approximated equilibrium constant for the dissociation of Wannier excitons at zero applied field, as below;

$$k_{CS}(E) = \frac{3\langle\mu\rangle e}{4\pi\langle\epsilon_r\rangle\epsilon_0 a^3} \exp\left(\frac{-\Delta E}{k_B T}\right) \left[1 + b + \frac{b^2}{3} + \frac{b^3}{18} + \dots\right]$$

where $\langle\mu\rangle$ is the spatially averaged sum of the electron and hole mobilities, $\langle\epsilon_r\rangle$ is the spatially averaged dielectric constant, ΔE is the Coulomb attraction of the initially generated ion pair after thermalization, $\Delta E = e^2/4\pi\langle\epsilon_r\rangle\epsilon_0 a$, and $b = e^3 E/8\pi\langle\epsilon_r\rangle\epsilon_0 k_B^2 T^2$, where the final summation is the approximation of a first-order Bessel function. As a noteworthy point, Braun's model is crucially different in that the dissociation of a CT state into free carriers is a reversible process. Moreover, a number of modification in Onsager's original model has been attempted so far, e.g., taking into account electron trajectory for the application in the materials with high mobility⁴², or distribution of CT-state separation distance in disordered materials⁴⁴. However, even though the Onsager theory is recognized as the effective prediction for exciton dissociation in specific systems, it does not include a comprehensive interpretation of dynamic lattice distortions/relaxations addressed in the nonadiabatic theory (i.e., the concept of

reorganization energy in the Marcus theory).

1-1-6. Exciton dissociation in OPVs

CT excitons have been attractively investigated in the research field of organic photovoltaics (OPV) rather than OLEDs, because low exciton binding energy is preferable for the conversion from photon to charge carriers. The elementary process of photoelectron conversion is mainly divided into 1) photo-absorption, 2) exciton diffusion, 3) formation of CT excitons, 4) dissociation to free carriers, and 5) charge transport^{30, 45}, as illustrated in **Figure 1-5**.

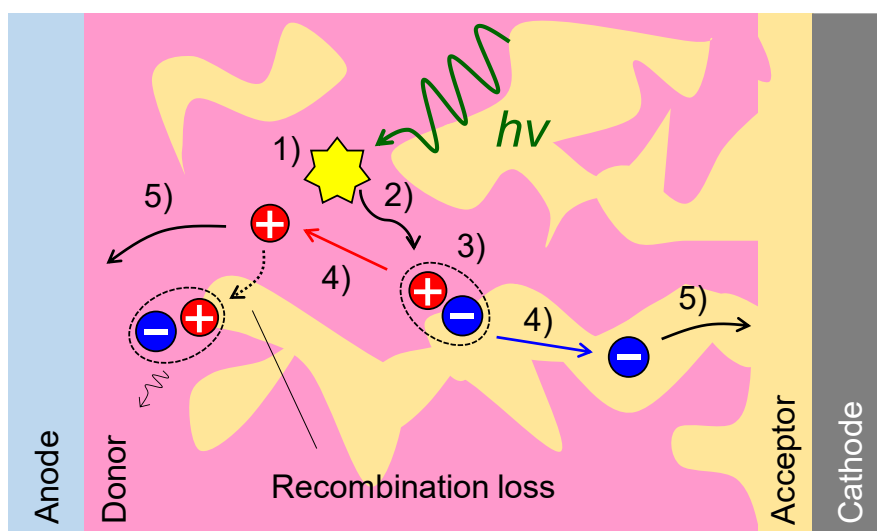


Figure 1-5. Photoelectron conversion process in OPVs.

Toward an increase in incident photon-to-current conversion efficiency (IPCE) and a comprehensive understanding of conversion dynamics, each process has been studied by a large number of groups. Especially, the charge separation process from the CT excitons is the most attractive topic. Conventional OPVs are based on the architecture of

bulk heterojunction systems including a D polymer and an A molecule such as poly(3-hexylthiophene) and fullerene derivatives, respectively^{46, 47}. In these systems, the binding energy of the CT states is usually lower than the singlet excitons of D and A molecules⁴⁸, facilitating the CS process (**Figure 1-6**). It is noted that an exciton binding energy in OPVs is defined as the potential energy difference between a neutral singlet exciton and the two fully dissociated states, i.e., ionic states, of two different molecules. Therefore, managing the HOMO level in a D molecule and the LUMO level in an A molecule is essential for efficient charge separation. Here the suppression of energy loss will be mentioned in the latter part.

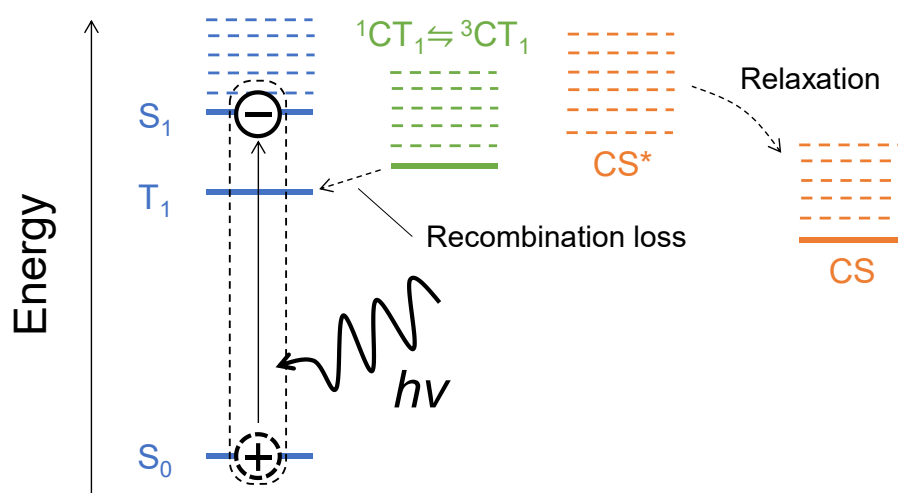


Figure 1-6. Energy level diagram in OPVs based on a D-A bimolecular system.

As explained in **Section 1-1-5**, two major types of the separation path, i.e., a hot process and a cold process, have been considered^{30, 49}. In the hot process, CT excitons can dissociate with the aid of the excess energy on the photo-excitation. H. Ohkita et al. reported that the amount of photo-generated free carriers increases with enlarging the LUMO offset between conjugated polymers and fullerene⁵⁰. In addition, G. Grancini et

al. revealed that the charge separation efficiency was enhanced on high-energy excitation due to the contribution of higher-lying CT energy states⁵¹, i.e., a hot CT process. The hot CT process is also accelerated by delocalization of the wavefunction induced by the crystallization of p-type polymer or the aggregation of n-type fullerene derivatives^{52, 53}. As a result, the effective charge separation is observed in the molecular system displaying small energy offset between D and A in recent years⁵⁴⁻⁵⁶. In the cold process, on the other hand, an electric field is necessary for the charge separation as noted in **Section 1-1-5**. In this model, the charge separation from CT excited states is the thermally activated event for overcoming Coulomb potential, indicating that the cold process undergoes somehow slowly. Since the hot process proceeds with a significantly rapid timescale because of the competition against vibrational relaxation in a sub-picosecond timescale, it is expected that the hot process is predominant in the charge carrier generation. However, the dissociation characteristics of CT excitons affect not only the charge generation but also the charge transport, as noted in **Section 1-1-5** that the photo-generated charge carriers *re-form* the CT excitons by geminate recombination. As a result, the CT excitons cause energy loss by relaxation to the local T₁ state of D or A molecules (**Figure 1-6**), i.e., back electron transfer (BET)^{57, 58}. In this case, the management of exciton dissociation via the cold process must be important due to the less excess energy such as the hot process.

1-1-7. Organic long persistent luminescence (OLPL)

A series of unique excitonic processes from exciton generation to charge separation and recombination events which are reminiscent of the OPVs system can be observed in an organic thin film. Organic long persistent luminescence (OLPL) known as one of the most promising long-lived-emission at room temperature was first reported by R. Kabe

and C. Adachi in 2017 ⁵⁹ (**Figure 1-7**). The OLPL system is based on a bimolecular exciplex consisting of a D molecule and an A molecule with a molar ratio of 1:99. In this system, the photogenerated carriers are remained in the solid-state film for a long time and gradually consumed by the charge recombination due to the low encountering probability of hole-electron pairs, resulting in the long-lived-emission. Hence, the emission decay in OLPL follows a power-law, not an exponential function applied in a typical fluorescence decay. The OLPL can be observed even without high-power photoexcitation as in the case of two-photon ionization, because the charge generation originates in the dissociation of intermolecular CT-excitons, i.e., nearly the same system as OPVs. Recently, several ideas have been proposed for enhancing OLPL duration, such as the reduction of a Coulombic interaction by using a cationic acceptor and an anionic donor, and introduction of carrier-trapping materials⁶⁰. However, the driving force of initial charge separation and subsequent carrier diffusion is not discussed sufficiently in OLPL films. Furthermore, a convincing reason for the OLPL lasting for over a few hours is still veiled.

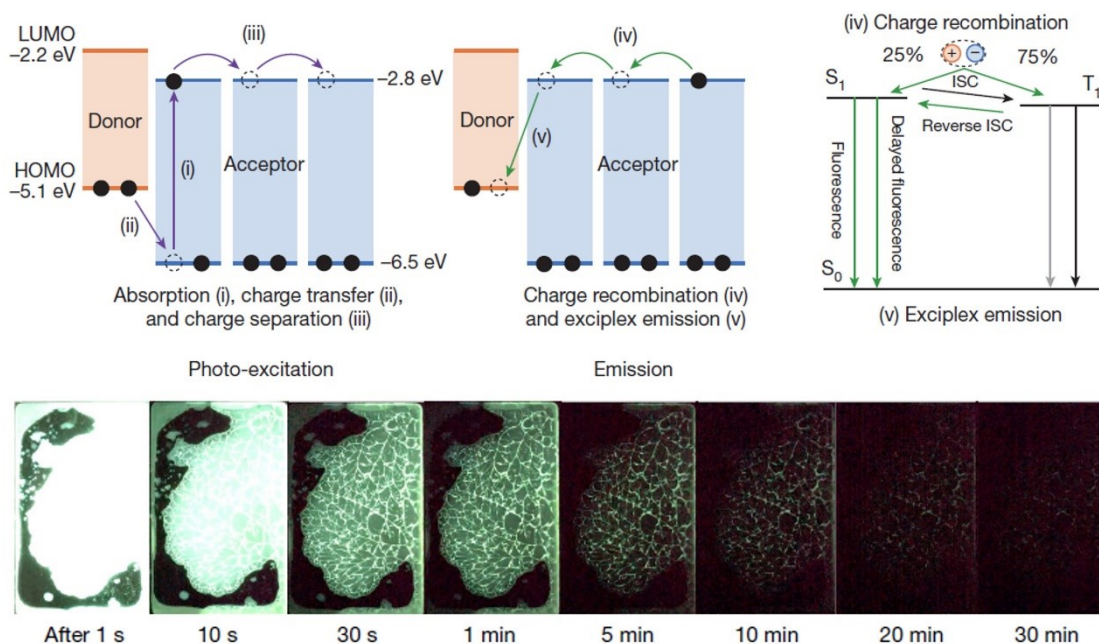


Figure 1-7. A mechanism and photographs of OLPL. (These figures were cited from R. Kabe and C. Adachi, *Nature* **550**, 384-387 (2017)⁵⁹)

1-1-8. Molecular polarization in solid-state film.

Depending on the symmetry of molecules, it is expected that molecules possess a permanent dipole moment (PDM) intrinsically due to the combination of each moiety with different electron affinity, resulting in polarization in a solid film. The polarization of emitters in OLEDs has been attracted since a giant surface potential (GSP) which is proportional to the film-thickness was confirmed in tris-(8-hydroxyquinolate)aluminum (Alq₃) by E. Ito et al⁶¹. The GSPs were assigned to the spontaneous ordering of a PDM by Y. Noguchi et al. in 2008, named spontaneous orientation polarization (SOP)⁶². The orientation polarization P_0 in a solid-state film shown in **Figure 1-8a** is defined as⁶³

$$P_0 = p\langle \cos \theta \rangle n$$

where p is the PDM of the molecule, $\langle \cos \theta \rangle$ is the average orientation degree of PDM with respect to the normal surface direction, and n is the density of the molecule. Taking

account of a boundary condition at the film surface, the surface potential (V_s) with reference to the substrate is given by

$$V_s = \frac{P_0 d}{\varepsilon}$$

where d is the film thickness, and ε is the dielectric constant. Here, GSP which is proportional to the film thickness can be measured by a Kelvin probe method⁶¹. Moreover, in the case of bilayer devices including polar molecules, the SOP characteristics are examined by a displacement current measurement (DCM)^{64, 65}. The charge carrier accumulation at organic heterointerfaces below threshold voltage should be observed due to the compensation for the surface potential induced by SOP (**Figure 1-8b**). Here, the interface charge density (σ_{int}) is calculated by⁶⁶

$$-\sigma_{\text{int}} = \int_{V_{\text{acc}}}^{V_{\text{th}}} C dV$$

where V_{acc} and V_{th} are accumulation and threshold voltage, respectively, and C is the effective capacitance proportional to the displacement current.

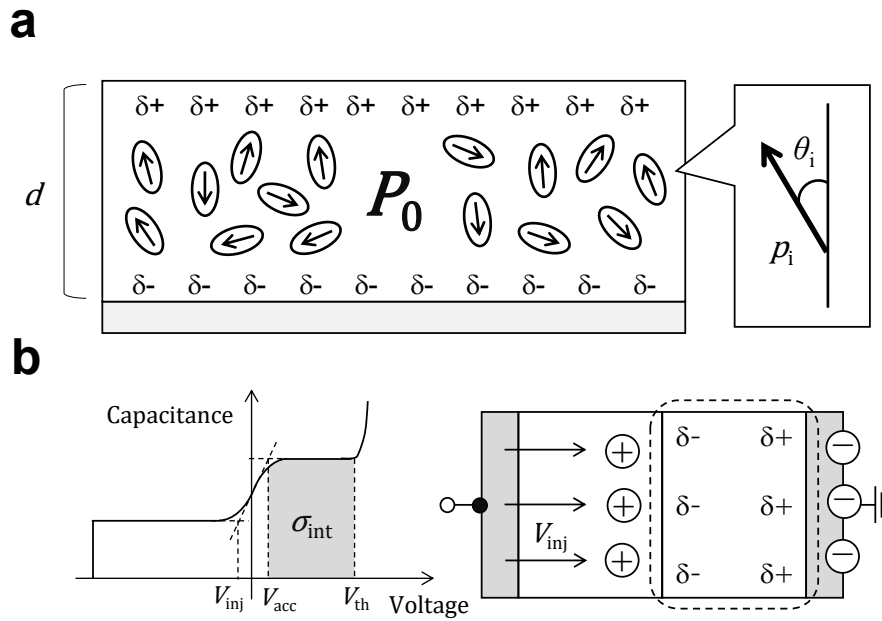


Figure 1-8. (a) Schematic illustration of an organic solid-state film with SOP. (b) Schematic illustration of a typical DCM curve for a bilayer device.

The molecular polarization largely influences the OLED performances such as stability and EQE^{63, 67, 68}. For example, the luminance degradation was observed in the device including a polar 1,3,5-tris(1-phenyl-1H-benzimidazol-2-yl) benzene (TPBi), in which the decomposition and chemical reactions of molecules are facilitated because of a hole capture induced by the SOPs near the interface between an emission layer (EML) and the TPBi⁶⁷. The accumulated charge carriers also interact with the excitons formed in the EML, namely exciton-polaron quenching (EPQ), resulting in the reduction of EQE⁶⁸. Furthermore, the PDMs correlate with not only electrical behavior but also an orientation of the TDM limiting η_{OC} of OLEDs^{69, 70}. Although the correlation between molecular polarity and OLED performance has been investigated by many groups as noted earlier, the dynamics of exciton dissociation in a molecular system exhibiting SOP have not been studied so far.

1-2. Purpose and outline of this thesis

TADF molecules consisted of a D-A combined structure forming the CT excited states as mentioned in the prior section, indicating that photo-active characteristics such as charge separation in OPVs are incorporated intrinsically even though the molecules are designed as an emitter for OLEDs. Although the exciton dissociation processes in intermolecular CT excitons have been studied in detail, those in the intramolecular CT excitons such as TADF molecules are still unclarified. In addition, the polarization which affects the electrical behavior of organic semiconductors tends to be induced in a solid-state film, expected to contribute to the spontaneous exciton dissociation. Thus, this thesis focuses on the investigation of exciton dissociation for polar TADF molecules exhibiting CT excited states in solid-state films.

In **Chapter 2**, the exciton dissociation of a highly-doped polar organic emitter exhibiting TADF in a host matrix was studied by using the method of a TRPL measurement. A long-lived PL decay observed in a solid-state film containing polar TADF emitters was assigned to slow recombination events of photogenerated charge carriers dissociated from the CT excited states spontaneously. While excitons of the conventional emitter are generally believed to be stable because of their high exciton binding energies, this study points out that the dissociation of CT exciton undergoes spontaneously due to the electrical field induced by the molecular polarization, and promotes the long-lived emission.

In **Chapter 3**, the role of excited spin states on the spontaneous exciton dissociation in polar organic films including TADF emitters that exhibit SOP was investigated. The fluorescence lifetime of 4CzIPN was measured under an electric field, pointing out that the excited spin-triplet state is advantageous for the exciton dissociation in the solid films.

Moreover, the exciton dissociations in a triplet-deactivated system were also evaluated by measuring the TRPL characteristics of a co-deposited film including the 4CzIPN and a triplet scavenging host of 9,10-bis(2-naphthyl)anthracene (ADN). This result also supports that the excited spin-triplet state plays an important role in the exciton dissociation.

In **Chapter 4**, a charge storage device using the principle of exciton dissociation was explored. The lifetime of charge carrier photogenerated in the organic films was characterized by a pulse-driven EL measurement. The EL pulse was assigned to the recombination of charge carriers dissociated from CT exciton by EL measurements synchronized with DCM. This study highlighted that the charge carriers dissociated from TADF emitters were stored in the EML stably, in both aspects of temporal and spatial, and a multi-functional organic device combined light-receiving, memory, and emission were proposed.

In **Chapter 5**, this thesis was summarized, and a future perspective was introduced.

References

1. P. R. Bell, The Use of Anthracene as a Scintillation Counter. *Phys. Rev.* **73**, 1405-1406 (1948).
2. H. C. Albert, J. C. Fugh, J. R. Norman and B. Ernst, The Demonstration of Pneumococcal Antigen in Tissues by the Use of Fluorescent Antibody. *J. Immunol.* **45**, 159-170 (1942).
3. F. P. Schäfer, W. Schmidt and J. Volze, ORGANIC DYE SOLUTION LASER. *Appl. Phys. Lett.* **9**, 306-309 (1966).
4. C. W. Tang and S. A. VanSlyke, Organic electroluminescent diodes. *Appl. Phys. Lett.* **51**, 913-915 (1987).
5. S.-J. Zou, Y. Shen, F.-M. Xie, J.-D. Chen, Y.-Q. Li and J.-X. Tang, Recent advances in organic light-emitting diodes: toward smart lighting and displays. *Mater. Chem. Front.* **4**, 788-820 (2020).
6. C. Hosokawa, H. Higashi, H. Nakamura and T. Kusumoto, Highly efficient blue electroluminescence from a distyrylarylene emitting layer with a new dopant. *Appl. Phys. Lett.* **67**, 3853-3855 (1995).
7. T. Wakimoto, R. Murayama, K. Nagayama, Y. Okuda and H. Nakada, Organic EL cells with high luminous efficiency. *Appl. Surf. Sci.* **113-114**, 698-704 (1997).
8. C. W. Tang, S. A. VanSlyke and C. H. Chen, Electroluminescence of doped organic thin films. *J. Appl. Phys.* **65**, 3610-3616 (1989).
9. C. H. Chen, C. W. Tang, J. Shi and K. P. Klubek, Improved red dopants for organic electroluminescent devices. *Macromol. Symp.* **125**, 49-58 (1998).
10. M. A. Baldo, D. F. O'Brien, Y. You, A. Shoustikov, S. Sibley, M. E. Thompson and S. R. Forrest, Highly efficient phosphorescent emission from organic electroluminescent devices. *Nature* **395**, 151-154 (1998).
11. M. A. Baldo, S. Lamansky, P. E. Burrows, M. E. Thompson and S. R. Forrest, Very high-efficiency green organic light-emitting devices based on electrophosphorescence. *Appl. Phys. Lett.* **75**, 4-6 (1999).
12. C. Adachi, M. A. Baldo, M. E. Thompson and S. R. Forrest, Nearly 100% internal phosphorescence efficiency in an organic light-emitting device. *J. Appl. Phys.* **90**, 5048-5051 (2001).
13. A. Endo, M. Ogasawara, A. Takahashi, D. Yokoyama, Y. Kato and C. Adachi, Thermally activated delayed fluorescence from Sn(4+)-porphyrin complexes and their application to organic light emitting diodes--a novel mechanism for electroluminescence. *Adv. Mater.* **21**, 4802-4806 (2009).

14. X.-K. Chen, D. Kim and J.-L. Brédas, Thermally Activated Delayed Fluorescence (TADF) Path toward Efficient Electroluminescence in Purely Organic Materials: Molecular Level Insight. *Acc. Chem. Res.* **51**, 2215-2224 (2018).
15. A. Endo, K. Sato, K. Yoshimura, T. Kai, A. Kawada, H. Miyazaki and C. Adachi, Efficient up-conversion of triplet excitons into a singlet state and its application for organic light emitting diodes. *Appl. Phys. Lett.* **98**, 083302 (2011).
16. H. Uoyama, K. Goushi, K. Shizu, H. Nomura and C. Adachi, Highly efficient organic light-emitting diodes from delayed fluorescence. *Nature* **492**, 234-238 (2012).
17. K. Goushi, K. Yoshida, K. Sato and C. Adachi, Organic light-emitting diodes employing efficient reverse intersystem crossing for triplet-to-singlet state conversion. *Nat. Photonics* **6**, 253-258 (2012).
18. Y. Tsuchiya, S. Diesing, F. Bencheikh, Y. Wada, P. L. dos Santos, H. Kaji, E. Zysman-Colman, I. D. W. Samuel and C. Adachi, Exact Solution of Kinetic Analysis for Thermally Activated Delayed Fluorescence Materials. *J. Phys. Chem. A* **125**, 8074-8089 (2021).
19. R. G. Kepler, J. C. Caris, P. Avakian and E. Abramson, Triplet excitons and Delayed Fluorescence in Anthracene Crystals. *Phys. Rev. Lett.* **10**, 400-402 (1963).
20. V. Ern, H. Bouchriha, J. Fourny and G. Delacôte, Triplet exciton — trapped hole interaction in anthracene crystals. *Solid State Commun.* **9**, 1201-1203 (1971).
21. M. A. Baldo, C. Adachi and S. R. Forrest, Transient analysis of organic electrophosphorescence. II. Transient analysis of triplet-triplet annihilation. *Phys. Rev. B* **62**, 10967-10977 (2000).
22. S. Reineke, K. Walzer and K. Leo, Triplet-exciton quenching in organic phosphorescent light-emitting diodes with Ir-based emitters. *Phys. Rev. B* **75**, (2007).
23. D. Song, S. Zhao, Y. Luo and H. Aziz, Causes of efficiency roll-off in phosphorescent organic light emitting devices: Triplet-triplet annihilation versus triplet-polaron quenching. *Appl. Phys. Lett.* **97**, 243304 (2010).
24. H. Zamani Siboni and H. Aziz, Triplet-polaron quenching by charges on guest molecules in phosphorescent organic light emitting devices. *Appl. Phys. Lett.* **101**, 063502 (2012).
25. J. Gibson, A. P. Monkman and T. J. Penfold, The Importance of Vibronic Coupling for Efficient Reverse Intersystem Crossing in Thermally Activated Delayed Fluorescence Molecules. *Chemphyschem* **17**, 2956-2961 (2016).

26. H. Noda, X. K. Chen, H. Nakanotani, T. Hosokai, M. Miyajima, N. Notsuka, Y. Kashima, J. L. Bredas and C. Adachi, Critical role of intermediate electronic states for spin-flip processes in charge-transfer-type organic molecules with multiple donors and acceptors. *Nat. Mater.* **18**, 1084-1090 (2019).
27. Y. Wada, H. Nakagawa, S. Matsumoto, Y. Wakisaka and H. Kaji, Organic light emitters exhibiting very fast reverse intersystem crossing. *Nat. Photonics* **14**, 643-649 (2020).
28. L.-S. Cui, A. J. Gillett, S.-F. Zhang, H. Ye, Y. Liu, X.-K. Chen, Z.-S. Lin, E. W. Evans, W. K. Myers, T. K. Ronson, H. Nakanotani, S. Reineke, J.-L. Bredas, C. Adachi and R. H. Friend, Fast spin-flip enables efficient and stable organic electroluminescence from charge-transfer states. *Nat. Photonics* **14**, 636-642 (2020).
29. J. U. Kim, I. S. Park, C. Y. Chan, M. Tanaka, Y. Tsuchiya, H. Nakanotani and C. Adachi, Nanosecond-time-scale delayed fluorescence molecule for deep-blue OLEDs with small efficiency rolloff. *Nat. Commun.* **11**, 1765 (2020).
30. T. M. Clarke and J. R. Durrant, Charge Photogeneration in Organic Solar Cells. *Chem. Rev.* **110**, 6736-6767 (2010).
31. J. Frenkel, On the Transformation of light into Heat in Solids. I. *Phys. Rev.* **37**, 17-44 (1931).
32. G. Lanzani, *The Photophysics behind Photovoltaics and Photonics*. (Wiley, 2012).
33. G. H. Wannier, The Structure of Electronic Excitation Levels in Insulating Crystals. *Phys. Rev.* **52**, 191-197 (1937).
34. M. Pope, Charge-transfer exciton and ionic levels in organic crystals. *J. Polym. Sci. C Polym. Symp.* **17**, 233-240 (1967).
35. M. Knupfer, Exciton binding energies in organic semiconductors. *Appl. Phys. A* **77**, 623-626 (2003).
36. M. Rohlffing and S. G. Louie, Optical Excitations in Conjugated Polymers. *Phys. Rev. Lett.* **82**, 1959-1962 (1999).
37. J.-W. v. d. Horst, P. A. Bobbert, M. A. J. Michels and H. Bässler, Calculation of excitonic properties of conjugated polymers using the Bethe–Salpeter equation. *J. Chem. Phys.* **114**, 6950-6957 (2001).
38. I. G. Hill, A. Kahn, Z. G. Soos and J. R. A. Pascal, Charge-separation energy in films of π -conjugated organic molecules. *Chem. Phys. Lett.* **327**, 181-188 (2000).

39. B. Bernardo, D. Cheyns, B. Verreert, R. D. Schaller, B. P. Rand and N. C. Giebink, Delocalization and dielectric screening of charge transfer states in organic photovoltaic cells. *Nat. Commun.* **5**, 3245 (2014).
40. L. Onsager, Deviations from Ohm's Law in Weak Electrolytes. *J. Chem. Phys.* **2**, 599-615 (1934).
41. L. Onsager, Initial Recombination of Ions. *Phys. Rev.* **54**, 554-557 (1938).
42. M. Tachiya, Breakdown of the Onsager theory of geminate ion recombination. *J. Chem. Phys.* **89**, 6929-6935 (1988).
43. C. L. Braun, Electric field assisted dissociation of charge transfer states as a mechanism of photocarrier production. *J. Chem. Phys.* **80**, 4157-4161 (1984).
44. V. D. Mihailetschi, L. J. A. Koster, J. C. Hummelen and P. W. M. Blom, Photocurrent Generation in Polymer-Fullerene Bulk Heterojunctions. *Phys. Rev. Lett.* **93**, 216601 (2004).
45. J.-L. Brédas, J. E. Norton, J. Cornil and V. Coropceanu, Molecular Understanding of Organic Solar Cells: The Challenges. *Acc. Chem. Res.* **42**, 1691-1699 (2009).
46. G. Yu, J. Gao, J. C. Hummelen, F. Wudl and A. J. Heeger, Polymer Photovoltaic Cells: Enhanced Efficiencies via a Network of Internal Donor-Acceptor Heterojunctions. *Science* **270**, 1789-1791 (1995).
47. P. Schilinsky, C. Waldauf and C. J. Brabec, Recombination and loss analysis in polythiophene based bulk heterojunction photodetectors. *Appl. Phys. Lett.* **81**, 3885-3887 (2002).
48. D. Veldman, S. C. J. Meskers and R. A. J. Janssen, The Energy of Charge-Transfer States in Electron Donor-Acceptor Blends: Insight into the Energy Losses in Organic Solar Cells. *Adv. Funct. Mater.* **19**, 1939-1948 (2009).
49. H. Bässler and A. Köhler, "Hot or cold": how do charge transfer states at the donor-acceptor interface of an organic solar cell dissociate? *Phys. Chem. Chem. Phys.* **17**, 28451-28462 (2015).
50. H. Ohkita, S. Cook, Y. Astuti, W. Duffy, S. Tierney, W. Zhang, M. Heeney, I. McCulloch, J. Nelson, D. D. C. Bradley and J. R. Durrant, Charge Carrier Formation in Polythiophene/Fullerene Blend Films Studied by Transient Absorption Spectroscopy. *J. Am. Chem. Soc.* **130**, 3030-3042 (2008).
51. G. Grancini, M. Maiuri, D. Fazzi, A. Petrozza, H. J. Egelhaaf, D. Brida, G. Cerullo and G. Lanzani, Hot exciton dissociation in polymer solar cells. *Nat. Mater.* **12**, 29-33 (2013).

52. S. Gélinas, A. Rao, A. Kumar, S. L. Smith, A. W. Chin, J. Clark, T. S. v. d. Poll, G. C. Bazan and R. H. Friend, Ultrafast Long-Range Charge Separation in Organic Semiconductor Photovoltaic Diodes. *Science* **343**, 512-516 (2014).
53. Y. Tamai, K. Tsuda, H. Ohkita, H. Benten and S. Ito, Charge-carrier generation in organic solar cells using crystalline donor polymers. *Phys. Chem. Chem. Phys.* **16**, 20338-20346 (2014).
54. K. Kawashima, Y. Tamai, H. Ohkita, I. Osaka and K. Takimiya, High-efficiency polymer solar cells with small photon energy loss. *Nat. Commun.* **6**, 10085 (2015).
55. T. F. Hinrichsen, C. C. S. Chan, C. Ma, D. Paleček, A. Gillett, S. Chen, X. Zou, G. Zhang, H.-L. Yip, K. S. Wong, R. H. Friend, H. Yan, A. Rao and P. C. Y. Chow, Long-lived and disorder-free charge transfer states enable endothermic charge separation in efficient non-fullerene organic solar cells. *Nat. Commun.* **11**, 5617 (2020).
56. A. Classen, C. L. Chochos, L. Lürer, V. G. Gregoriou, J. Wortmann, A. Osvet, K. Forberich, I. McCulloch, T. Heumüller and C. J. Brabec, The role of exciton lifetime for charge generation in organic solar cells at negligible energy-level offsets. *Nat. Energy* **5**, 711-719 (2020).
57. A. Rao, P. C. Y. Chow, S. Gélinas, C. W. Schlenker, C.-Z. Li, H.-L. Yip, A. K. Y. Jen, D. S. Ginger and R. H. Friend, The role of spin in the kinetic control of recombination in organic photovoltaics. *Nature* **500**, 435-439 (2013).
58. M. Liedtke, A. Sperlich, H. Kraus, A. Baumann, C. Deibel, M. J. M. Wirix, J. Loos, C. M. Cardona and V. Dyakonov, Triplet Exciton Generation in Bulk-Heterojunction Solar Cells Based on Endohedral Fullerenes. *J. Am. Chem. Soc.* **133**, 9088-9094 (2011).
59. R. Kabe and C. Adachi, Organic long persistent luminescence. *Nature* **550**, 384-387 (2017).
60. K. Jinnai, R. Kabe, Z. Lin and C. Adachi, Organic long-persistent luminescence stimulated by visible light in p-type systems based on organic photoredox catalyst dopants. *Nat. Mater.* **21**, 338-344 (2022).
61. E. Ito, Y. Washizu, N. Hayashi, H. Ishii, N. Matsuie, K. Tsuboi, Y. Ouchi, Y. Harima, K. Yamashita and K. Seki, Spontaneous buildup of giant surface potential by vacuum deposition of Alq₃ and its removal by visible light irradiation. *J. Appl. Phys.* **92**, 7306-7310 (2002).
62. Y. Noguchi, N. Sato, Y. Tanaka, Y. Nakayama and H. Ishii, Threshold voltage shift and formation of charge traps induced by light irradiation during the fabrication of organic light-emitting diodes. *Appl. Phys. Lett.* **92**, 203306 (2008).

63. Y. Noguchi, W. Brütting and H. Ishii, Spontaneous orientation polarization in organic light-emitting diodes. *Jpn. J. Appl. Phys.* **58**, SF0801 (2019).
64. S. Egusa, N. Gemma, A. Miura, K. Mizushima and M. Azuma, Carrier injection characteristics of the metal/organic junctions of organic thin-film devices. *J. Appl. Phys.* **71**, 2042-2044 (1992).
65. S. Egusa, A. Miura, N. Gemma and M. Azuma, Carrier Injection Characteristics of Organic Electroluminescent Devices. *Jpn. J. Appl. Phys.* **33**, 2741-2745 (1994).
66. Y. Noguchi, Y. Miyazaki, Y. Tanaka, N. Sato, Y. Nakayama, T. D. Schmidt, W. Brütting and H. Ishii, Charge accumulation at organic semiconductor interfaces due to a permanent dipole moment and its orientational order in bilayer devices. *J. Appl. Phys.* **111**, 114508 (2012).
67. Y. Noguchi, H.-J. Kim, R. Ishino, K. Goushi, C. Adachi, Y. Nakayama and H. Ishii, Charge carrier dynamics and degradation phenomena in organic light-emitting diodes doped by a thermally activated delayed fluorescence emitter. *Org. Electron.* **17**, 184-191 (2015).
68. J. S. Bangsund, J. R. V. Sambeek, N. M. Concannon and R. J. Holmes, Sub-turn-on exciton quenching due to molecular orientation and polarization in organic light-emitting devices. *Sci. Adv.* **6**, eabb2659 (2020).
69. K. Osada, K. Goushi, H. Kaji, C. Adachi, H. Ishii and Y. Noguchi, Observation of spontaneous orientation polarization in evaporated films of organic light-emitting diode materials. *Org. Electron.* **58**, 313-317 (2018).
70. T. Morgenstern, M. Schmid, A. Hofmann, M. Bierling, L. Jager and W. Brütting, Correlating Optical and Electrical Dipole Moments To Pinpoint Phosphorescent Dye Alignment in Organic Light-Emitting Diodes. *ACS Appl. Mater. Interfaces* **10**, 31541-31551 (2018).

Chapter 2

Slow recombination of spontaneously dissociated organic fluorophore excitons

Takahiko Yamanaka, Hajime Nakanotani & Chihaya Adachi

Nature Communications **10**, 5748 (2019)

Abstract

The harvesting of excitons as luminescence by organic fluorophores forms the basis of light-emitting applications. Although high PLQY is essential for efficient light emission, concentration-dependent quenching of the emissive exciton is generally observed. Here we demonstrate the generation and accumulation of concentration-dependent “long-lived” (i.e., over 1 h) photo-generated carriers and the successive release of their energy as electroluminescence in a solid-state film containing a polar fluorophore. While fluorophore excitons are generally believed to be stable because of their high exciton binding energies, our observations show that some of the excitons undergo spontaneous exciton dissociation in a solid-state film by SOP even without an external electric field. These results lead to the reconsideration of the meaning of “luminescence quantum yield” for the solid films containing polar organic molecules because it can differ for optical and electrical excitation.

2-1. Introduction

Organic fluorophores dispersed in a host matrix form the basis of a variety of molecular optoelectronic systems for light-emitting applications, including light-emitting diodes¹, bio-imaging techniques², photon up-conversion systems³, luminescent solar concentrators⁴, and long-persistent luminescent materials⁵. In all of these applications, the choice of a material system with a high PLQY is essential for achieving highly efficient emission. However, the PLQY of fluorophores in a host matrix is generally sensitive to the doping concentration, limiting the fluorophores that can be used. In this study, we mainly focused on the excited-state dynamics of a highly-doped polar organic fluorophore exhibiting TADF⁶ in host molecules, because TADF has attracted great interest for organic light-emitting applications, such as OLEDs⁷ and OLPL⁵, and has been widely investigated over the last decades^{8, 9}. The interpretation that some of the excitons in the fluorophores undergo nonradiative relaxation to the ground state through a non-adiabatic interaction between two potential surfaces, *i.e.*, internal conversion¹⁰, or the deactivation via dipole–dipole interaction between neighbor fluorophores¹¹ is widely accepted. However, fluorophores exhibiting TADF are generally intramolecular D–A systems and naturally form a CT excited state in both S₁ and T₁. Thus, another nonradiative decay process should be considered: exciton dissociation, *i.e.*, carrier generation, through the CT-type exciton as an intermediate state which has been widely recognized in photovoltaic devices containing a mixture of donor and acceptor molecules¹². While the concentration-dependent quenching of the emissive exciton, generally called concentration quenching, is well known and usually attributed to dipole–dipole interactions, we unveil here an additional, non-negligible concentration quenching mechanism based on spontaneous excitons dissociation that has so far been overlooked.

2-2. Results and discussion

2-2-1. Photo-physical properties of TPA-DCPP

To find evidence of spontaneous exciton dissociation in organic fluorophore alone in a solid matrix, we first evaluated the fundamental PL properties of a model fluorophore, namely, TPA-DCPP¹³ (**Figure 2-1**) because it possesses a large permanent dipole moment (dipole moment = 13.05 D). The PLQY of TPA-DCPP doped in a CBP host matrix at different concentrations (the absorption and emission spectra are shown in **Figure 2-2**) decreased with an increase in the doping concentration as shown in **Figure 2-1a**, indicating the concentration quenching processes such as the deactivation of exciton via dipole–dipole interaction and the internal conversion process coexist in the highly doped films. Here note that the exciton quenching due to a back energy transfer from T₁ of TPA-DCPP (2.25 eV) to T₁ of CBP (2.55 eV) is negligible because the triplet energy level of the CBP matrix is higher than that of TPA-DCPP. Although the time constant of the delayed fluorescence component (τ_d : the radiative decay constant of the singlet excitons that are generated via reverse intersystem crossing from T₁ of TPA-DCPP) was estimated to be 50 μ s in a 10-wt%-TPA-DCPP:CBP film, τ_d becomes shorter with an increase of doping concentration (**Figure 2-1b**). This trend indicates that the deactivation rate of triplet excitons on TPA-DCPP increases with a reduction of the average distance between TPA-DCPP molecules.

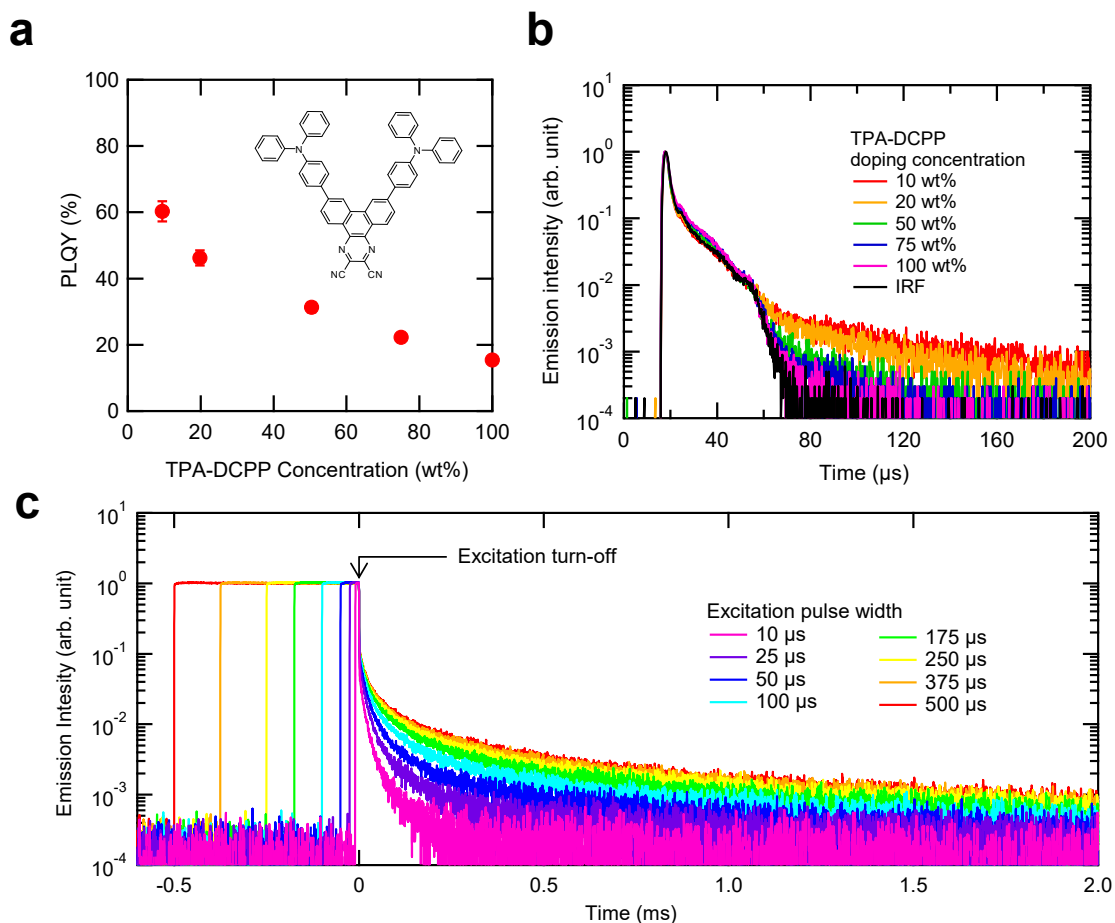


Figure 2-1. Fundamental PL properties of TPA-DCPP-based solid-state films. **(a)** Concentration dependence of PLQY in TPA-DCPP:CBP blends. The error bars are estimated by taking into account instrument accuracy and experimental variability. Inset: chemical structure of TPA-DCPP. **(b)** TRPL profiles in TPA-DCPP:CBP blends with different TPA-DCPP doping concentrations. The black line indicates the instrument response function (IRF) of the fluorescence lifetime spectrometer used for the measurements. **(c)** Dependence of TRPL profile on excitation pulse width for a 50-wt%-TPA-DCPP:CBP blend. A 470-nm light source was used as excitation light, and the power density was fixed at 25 mW cm^{-2} . The lifetime of the long-tailed component saturated for pulses longer than the width of 375 μ s.

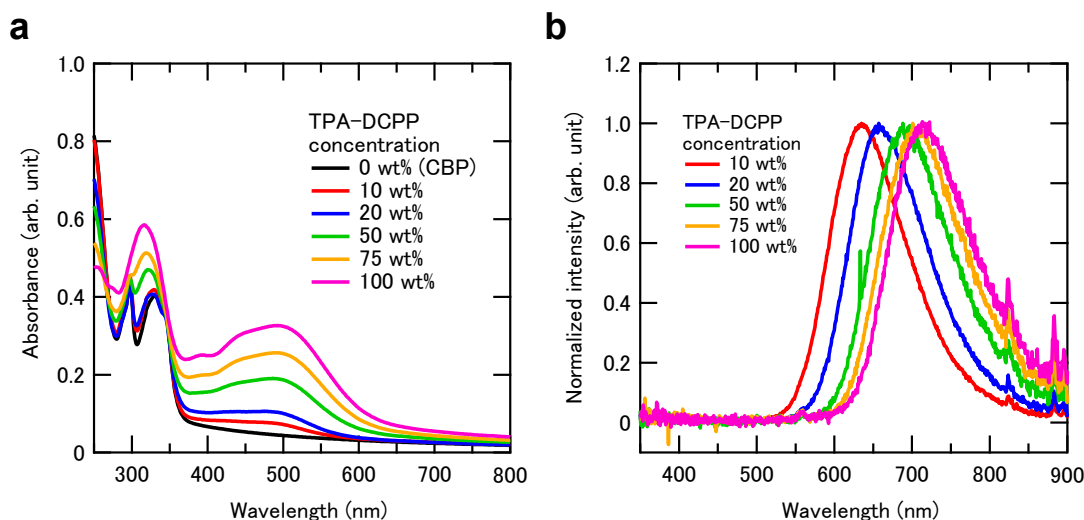


Figure 2-2. PL properties of TPA-DCPP-doped solid-state films. (a) Absorption spectra of TPA-DCPP:CBP blends with different TPA-DCPP doping concentrations. (b) Fluorescence spectra of TPA-DCPP:CBP blends with different TPA-DCPP doping concentrations.

To unravel the dynamics of the quenching process of the triplet excitons, the dependence of the TRPL decay on the photo-excitation pulse width was measured in a 50-wt%-TPA-DCPP:CBP film (**Figure 2-1c**). A long PL decay component with a millisecond-order decay lifetime, which is longer than τ_d , was observed only when the film was excited with long pulses ($>10 \mu\text{s}$). This long-lived PL does not originate from phosphorescence, because the long-lived emission lifetime is independent of the detection wavelength from 650 nm to 800 nm (**Figure 2-3**). These observations indicate that, following long-pulse excitation, a long-lived emission component that is different from “normal” triplet exciton decay, i.e., TADF, occurs in the blend film even after the excitation light is turned off when the film was excited by the long-excitation pulse width. Further, since the emission intensity in a 50-wt%-TPA-DCPP:CBP film shows the almost linear response for the excitation light power (**Figure 2-4**), the effect of the bimolecular

exciton annihilation process can be excluded. As the long PL decay component follows a power-law dependence (**Figure 2-5**), the origin of the long-lived emission can be considered as the recombination of separated carriers^{14, 15} generated by exciton dissociation.

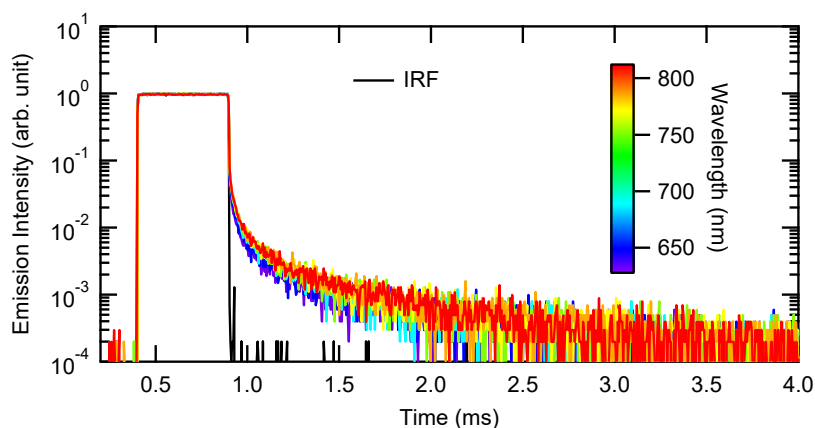


Figure 2-3. Dependence of TRPL profile on detection wavelength in a 50-wt%-TPA-DCPP:CBP blend. The black line indicates the IRF of the fluorescence lifetime spectrometer. A 470-nm light source was used as excitation light, and the power density was fixed at 25 mW cm^{-2} .

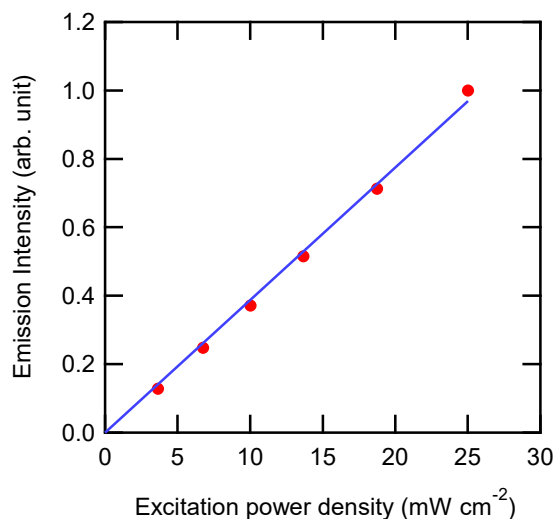


Figure 2-4. Dependence of emission intensity on excitation light power in a 50-wt%-TPA-DCPP:CBP blend.

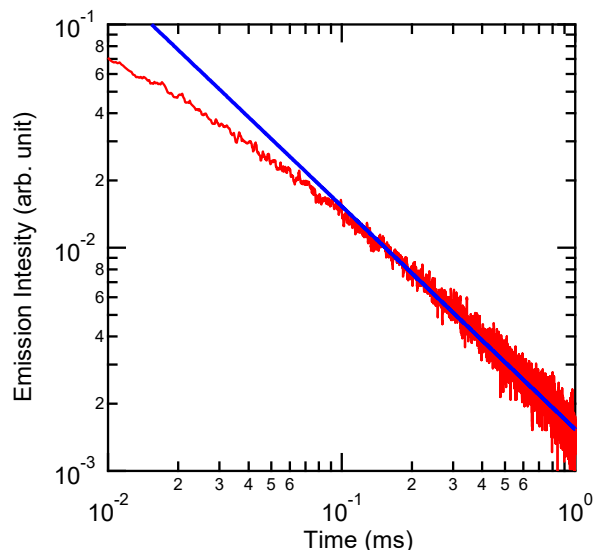


Figure 2-5. Log-log plot of the TRPL profile (excitation pulse width = 500 μ s) of a 50-wt%-TPA-DCPP:CBP blend. The red line indicates a power-law kinetic, i.e., emission intensity = t^{-m} ($m=1$).

2-2-2. External-electric-field-modulated TRPL

Since the motion of the carriers can be modulated by an electric field, we prepared a non-carrier-injection-type device to study the effect of an external electric field on the TRPL decay. A hole-blocking layer (T2T) and electron-blocking layer (CBP) were placed adjacent to the 50-wt%-TPA-DCPP:CBP layer (EML) to prevent carrier injection from each electrode into the EML (**Figure 2-6** and **Figure 2-7**). Additionally, the T2T and CBP layers contain almost no absorbance at the excitation wavelength (470 nm), meaning that only TPA-DCPP is directly excited (**Figure 2-8**). **Figure 2-6b** shows the results of the electric-field-modulated luminescence measurement. Even in the device architecture equipped with electrodes, long-lived emission similar to that in the case without electrodes was observed. When a forward-bias voltage pulse was applied to the ITO at one millisecond after turning off the excitation light, an emission spike was clearly observed. Since the emission spike is not observed under the same conditions without

prior photo-excitation (**Figure 2-9**), the emission spike can be attributed to carriers accumulated inside the EML and not injected carriers.

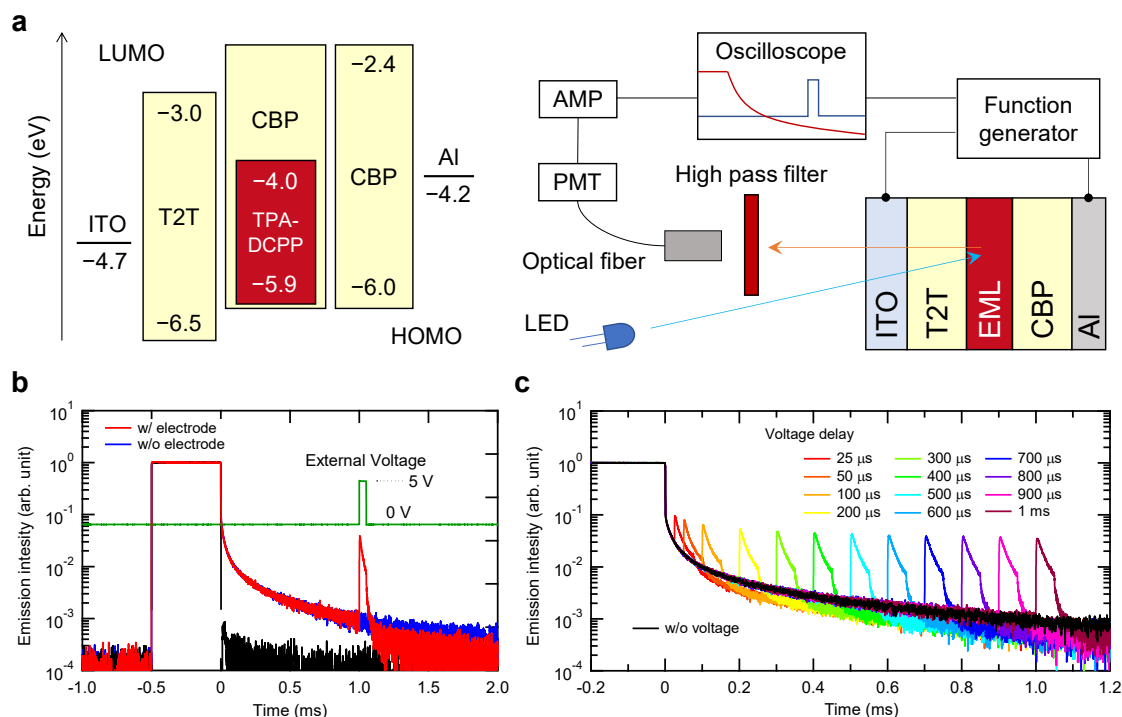


Figure 2-6. Device structure, experimental set-up, and external-electric-field-modulated luminescence. **(a)** Energy-level diagram of materials used in this work (left) and schematic of the experimental set-up for external-electric-field-modulated luminescence measurements (right). ITO and Al electrodes were used as anode and cathode, respectively. **(b)** External-electric-field-modulated TRPL profile in a device with a 50-wt%-TPA-DCPP:CBP blend (red line). The blue line is the TRPL profile of a 50-wt%-TPA-DCPP:CBP blend (without electrodes or T2T and CBP layers) for comparison. The black and green line indicates the IRF in this measurement system and the time profile of the external applied voltage, respectively. The excitation light pulse width was set to 500 μ s. **(c)** Dependence of the external-electric-field-modulated TRPL profiles on external-voltage-pulse delay in the 50 wt%-TPA-DCPP:CBP device. The applied voltage and the width were fixed to 5 V and 50 μ s, respectively. Note that it is not a multiple voltage pulses. This experiment used independent voltage pulses for each timing, and multiple measurements were performed.

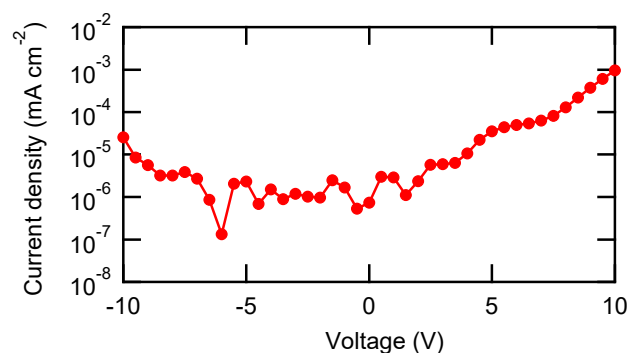


Figure 2-7. Current density-voltage characteristics of a non-injecting device. The current density is the nA cm^{-2} level even at 5 V, confirming no carrier injection.

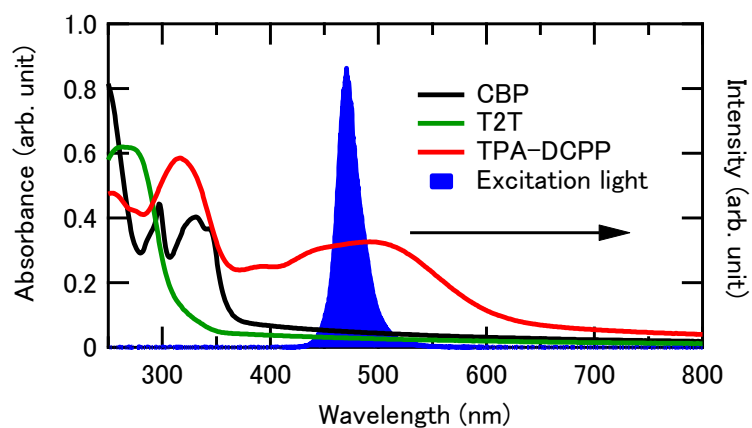


Figure 2-8. Absorption spectra of CBP, T2T, and TPA-DCPP films.

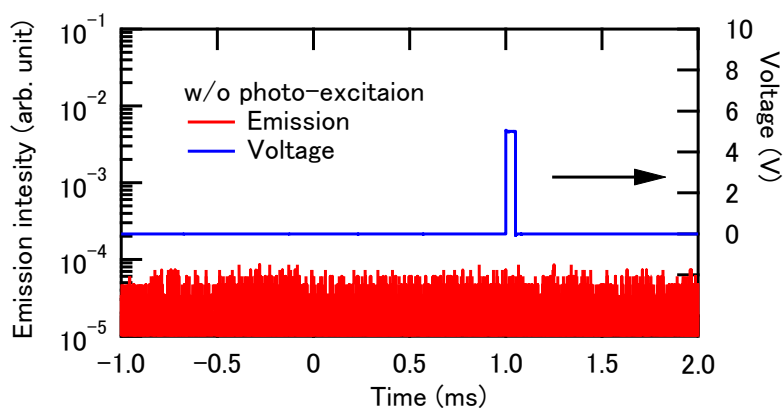


Figure 2-9. TRPL profile (red line) in a 50-wt%-TPA-DCPP:CBP non-injecting device (the same device used in the measurement shown in **Figure 2-6**) that was not photo-excited before applying the voltage.

The dependence of the TRPL profile on the timing of the external voltage pulse was also measured in the same device. As shown in **Figure 2-6c**, an emission spike appeared in the TRPL profile upon application of a voltage pulse regardless of the delay time. The TRPL tail intensity after applying the external electric field becomes appreciably weaker compared to the intensity when an electric field was not applied, again indicating that carriers generated by photo-excitation are being consumed by recombination. More interestingly, the emission spike intensity is relatively constant for delays ranging over 1 ms despite the gradual decrease in the long emission tail, and the spike could still be detected even after 1 h (**Figure 2-10**), indicating the existence of ultra-long-lived photo-generated carriers in the EML.

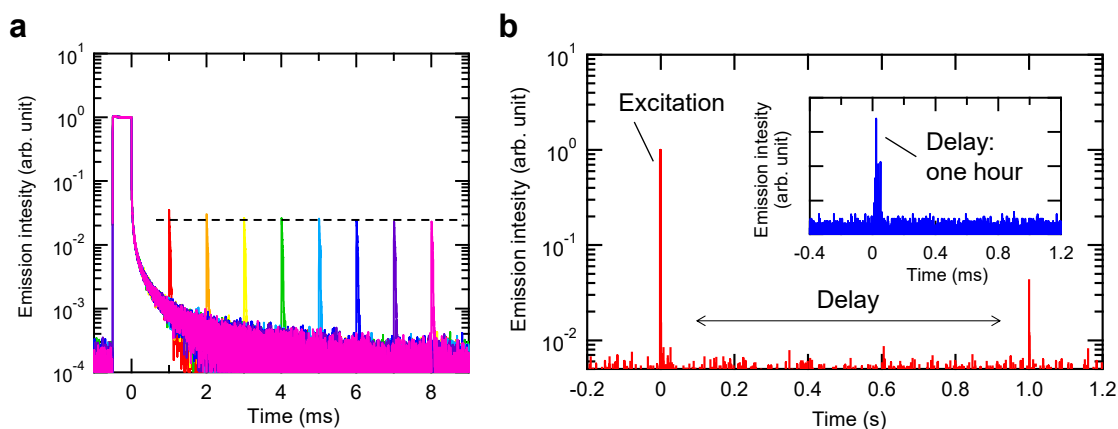


Figure 2-10. Dependence of the external-electric-field-modulated TRPL profiles on external-voltage-pulse delay (**a**: 10 ms range, **b**: second range, **b inset**: hour range) in the 50-wt%-TPADCPP:CBP non-injecting device. The excitation light pulse width was set to 500 μ s. The applied voltage and width were fixed to 5 V and 50 μ s, respectively. The TRPL signals for the one-hour-delay measurement were averaged just 10 times because of equipment limitations.

The origin of the long-lived photo-generated carriers leading to luminescence upon application of an external electric field can be ascribed to exciton dissociation by an internal electric field. This hypothesis is reinforced by the following experimental results. First, the TRPL decay and spike intensity are affected by applying a reverse bias during and after excitation (**Figure 2-11a**). The TRPL decay appreciably reduced for a reverse bias of -10 V compared to with no biasing. In the case of a low bias voltage (-10 V), since the potential slope in the EML is rather steep, the photo-generated carriers are rapidly separated and then kept apart under the influence of the field, so the carriers recombine inefficiently. Second, when multiple voltage pulses are applied to the sample, the spike emission intensity decreases with each pulse (**Figure 2-11b**), indicating the stepwise consumption of carriers. Finally, the TRPL decay diminishes with an increase in excitation power density (**Figure 2-11c**). This can be understood as a shortening of the diffusion length of the carriers because of an increase in recombination probability associated with the denser triplet generation. This result also excludes the possibility of carrier generation through two-photon ionization of TPA-DCPP¹⁵.

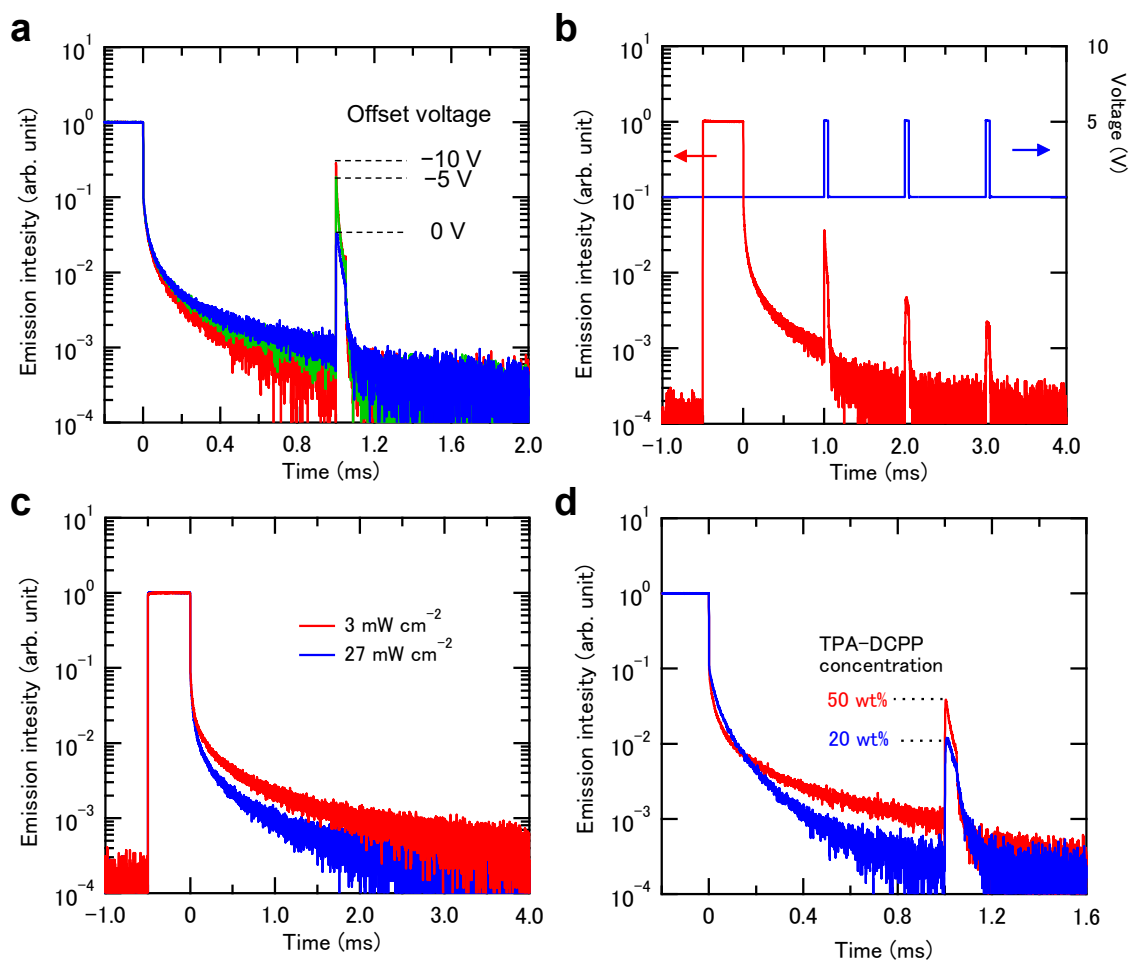


Figure 2-11. (a) Dependence of the emission spike intensity in TRPL profiles on the offset voltage for the 50-wt%-TPA-DCPP:CBP non-injecting device. The dashed lines indicate the maximum intensity for each condition. Note that the prompt decay profiles (from 0 to 1 ms) also show an offset voltage dependence. (b) External-electric-field-modulated TRPL profiles (red line) with multiple voltage pulses (blue line) for the 50-wt%-TPA-DCPP:CBP non-injecting device. The applied voltage and width were fixed at 5 V and 50 μ s, respectively. (c) Dependence of the TRPL decay profile on the excitation light power (3 or 27 mW cm^{-2}) for a 50-wt%-TPA-DCPP:CBP blend. (d) Dependence of the emission spike intensity in the TRPL profile on the doping concentration for TPA-DCPP:CBP non-injecting devices. The dashed lines indicate the maximum intensity for each concentration. Note that the prompt decay profiles (from 0 to 1 ms) also show a concentration dependence.

2-2-3. The role of SOP in exciton dissociation event

To gain more insight into the mechanism, we conducted DCM characterization¹⁶ of an OLED with a TPA-DCPP:CBP layer as the EML. As shown in **Figure 2-12a**, we found a clear threshold-voltage shift depending on the doping concentration, indicating a larger accumulation of interfacial charges with an increasing concentration of TPA-DCPP (from 20 wt% to 50 wt%). Furthermore, DCM was also performed on the device used for the TRPL measurements to verify the accumulated carriers (**Figure 2-12b**). In the first scan after light irradiation accompanied with a bias of -10 V, the transient current peak appeared at 2.5 V. The current peak, however, disappeared in the second scan. This is again consistent with accumulated carriers being consumed as recombination current.

Based on the DCM results, we can explain the driving force for carrier generation in the solid films. Since a permanent dipole moment of CBP is close to zero and TPA-DCPP has a large permanent dipole moment (13.05 D), the threshold-voltage shift observed in the DCM (**Figure 2-12a**) can be attributed to the formation of a concentration-dependent potential slope across the EML by SOP^{17, 18} of TPA-DCPP molecules. Since the concentration-dependent potential slope means a change of polarity of the EML with increasing the doping concentration, the PL spectrum of the highly doped codeposited film shows a redshifted spectrum as shown in **Figure 2-2b**. In other words, the observation of the redshifted spectrum with increasing the doping concentration is not conflicting with our proposed mechanism. In fact, the intensity of the emission spike in a 20-wt%-doped non-injecting device is much weaker than that of a 50-wt%-doped one (**Figure 2-11d**), which is due to a lower exciton dissociation probability. Since the accumulated interfacial charge density at the 50-wt%-doped EML interface is calculated to be -1.6 mC m^{-2} , the large surface potential slope can be 54.9 mV nm^{-1} at least. The

potential slope should be formed across the solid film, so some of the photo-generated excitons on TPA-DCPP can spontaneously dissociate even without an external applied electric field (**Figure 2-12c**). The origin of the long-lived emission observed in the solid film thus can be attributed to the recombination of holes and electrons that were generated by spontaneous exciton dissociation. We roughly calculate the yield of long-lived emission to total emission is ~1%, so the dissociation yield should be much higher than this. Compared with the total exciton quenching yield, the dissociation yield is actually quite small, but the fact that the process exists cannot be ignored. Here, we discuss the role of spin states in the spontaneous exciton dissociation by the SOP. The triplet excitons of polar molecules, i.e., CT-type molecules exhibiting TADF, are considered to dissociate because of (i) the long exciton lifetime, and (ii) the small energy splitting between singlet CT and triplet CT energy levels. Further, the disappearance of the delayed fluorescence component with increasing the doping concentration suggests the quenching of the triplet exciton. However, it cannot be determined which spin state, singlet and triplet, is responsible for the exciton dissociation at this stage. While we need to study it in more detail, it is evident that excitons are spontaneously dissociated by SOP.

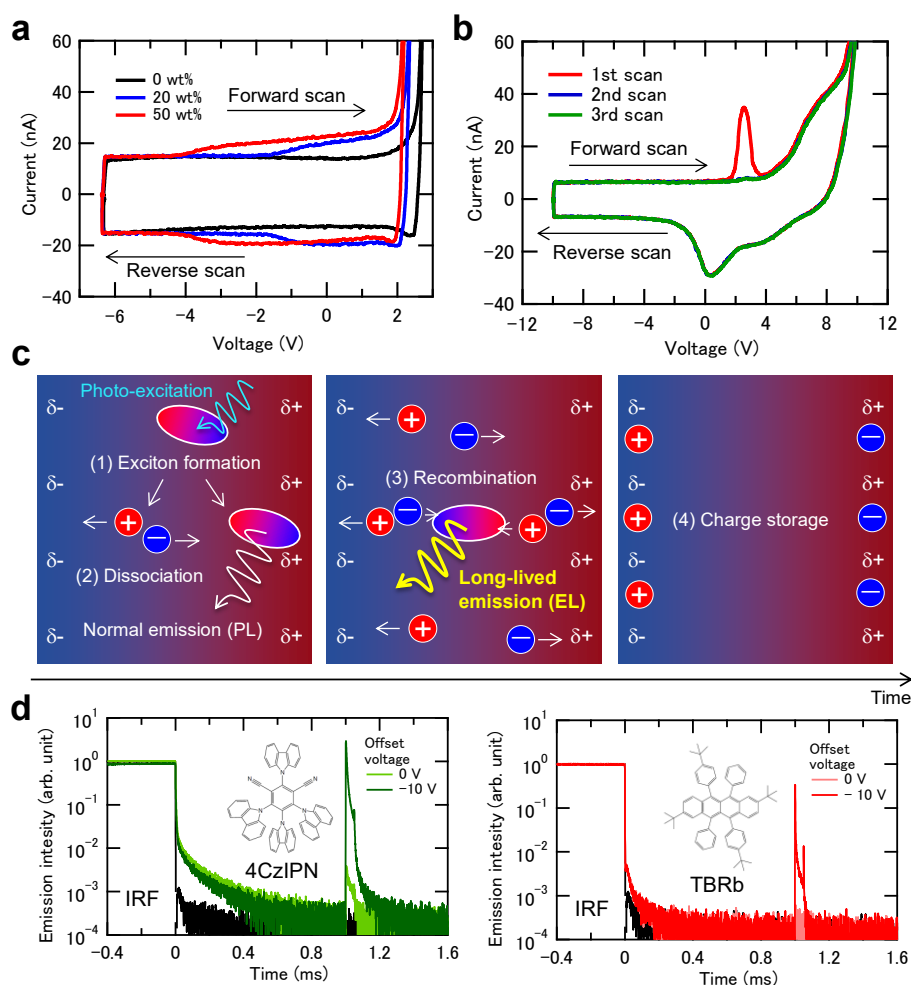


Figure 2-12. DCM and the observation of long-lived emission from other fluorophores. **(a)** DCM profiles in OLEDs with EMLs of TPA-DCPP:CBP having different TPA-DCPP doping concentrations. The device structure was ITO (100 nm)/TAPC (50 nm)/EML (30 nm)/T2T (20 nm)/BPy-TP2 (60 nm)/LiF (1.6 nm)/Al (100 nm). **(b)** Dependence of DCM profiles on the number of scans in non-injecting TPA-DCPP:CBP devices with the structure in **Figure 2-6a**. **(c)** Schematic of spontaneous exciton dissociation and recombination processes in solid films containing organic polar fluorophores. **(d)** TRPL profiles in the non-injecting device based on 50-wt%-TBRb:CBP and 50-wt%-4CzIPN:CBP blend as EML with the structure in **Figure 2-6a**. A long PL decay component having a millisecond-order decay lifetime that is much longer than the intrinsic time constant of TADF ($\tau_d = 2.3 \mu\text{s}$) was observed in the 50-wt%-4CzIPN:CBP blend. In these measurements, a UV-LED with a peak wavelength of 340 nm was used as the excitation light source. Note that the ITO electrode slightly absorbs the excitation light and emits light. The applied peak voltage and the width were fixed to 5 V and 50 μs , respectively.

Although long-lived emission was completely absent from a film doped with the non-polar fluorophore TBRb, long-lived emission was observed from a film doped with the polar fluorophore 4CzIPN⁷ (3.85 D), which also exhibits SOP¹⁹ (**Figure 2-12d**). Further, even when the voltage offset was set to 0 V, the non-injection-type devices based on 4CzIPN:CBP blends show clear EL spikes when an external voltage pulse is applied. This result indicates that the excitons of 4CzIPN are spontaneously dissociated and diffused by the SOP. Also, of course, when the voltage offset was set to -10 V on the TBRb-based device, a clear response of the EL spike due to the external voltage pulse was observed. This result shows that the excitons of TBRb dissociate by the “external” electric field. However, when the voltage offset was set to 0 V, no response was observed because of a lacking of SOP. Therefore, our proposed mechanism can explain the additional concentration-dependent quenching process in polar fluorophores. Furthermore, as the larger spatial separation²⁰ of the hole and electron in intermolecular D–A systems leads to a much weaker exciton binding energy compared to that of intramolecular D–A systems, the driving force for charge separation in exciplex-based LPL systems⁵ containing 2,8-Bis(diphenylphosphoryl)-dibenzo[b,d]thiophene, which has a moderate dipole moment (4.60 D), can also be well explained by our proposed mechanism. Additionally, the long-lived decay disappears completely in transient electroluminescence profiles (**Figure 2-13**) of OLEDs because the applied voltage promotes carrier recombination rather than charge separation. This means that there is an additional exciton quenching process under optical excitation that does not exist under electrical excitation condition. Thus, the luminescence quantum yield of solid films containing polar fluorophores or polar host matrix can differ for optical and electrical excitation, especially in the case of exciplexes²¹.

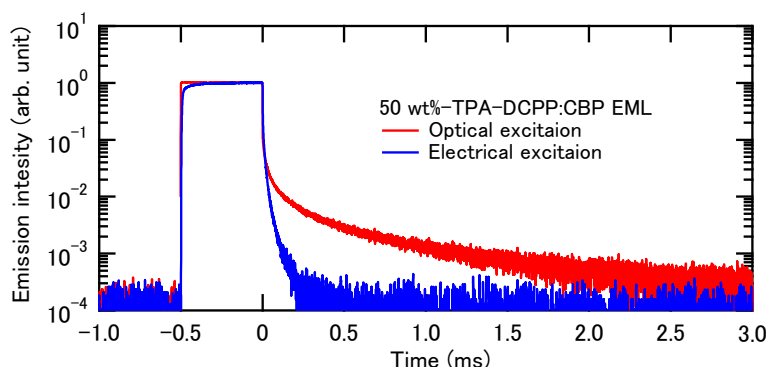


Figure 2-13. Comparison of transient emission decay profiles under optical and electrical excitation. The device structure was ITO (100 nm) / TAPC (50 nm) / EML (30 nm) / T2T (20nm) / BPy-TP2 (60 nm) / LiF (1.6 nm) / Al (100 nm). For electrical excitation, a constant current density (1.0 mA cm^{-2}) was injected into the device for 500 μs .

2-3. Summary

We investigated the exciton dissociation of a CT-type fluorophore in a solid film. A long-lived emission observed in the PL measurement of CBP:TPA-DCPP codeposited film was assigned to the slow recombination event of the charge carrier dissociated from the exciton. The charge carriers were modulated by an external electric field, and an emission enhancement due to the charge carrier recombination was detected. We also found that the spontaneous exciton dissociation undergoes in a CT-type fluorophore exhibiting large SOP by DCM characterization. Thus, the exciton dissociation leads to decline of the luminescence efficiency as a non-negligible concentration quenching.

2-4. Sample preparation and experimental methods

2-4-1. Materials

The molecules 4'-bis(carbazol-9-yl) biphenyl (CBP), 7,10-bis(4-(diphenylamino)phenyl)-2,3-dicyanopyrazinophenanthrene (TPA-DCPP), 2,4,6-tris(biphenyl-3-yl)-1,3,5- triazine (T2T), and 2,7-bis(2,2'-bipyridine-5-yl)triphenylene (BPy-TP2) were purchased from NARD institute, Ltd. The molecules 1,1-bis[(di-4-tolylamino)phenyl]cyclohexane (TAPC) and 2,8-di-tert-butyl-5,11-bis(4-tert-butylphenyl)-6,12-diphenyltetracene (TBRb) were purchased from Luminescence Technology Corp. The molecule 2,4,5,6-tetra(9H-carbazol-9-yl)isophthalonitrile (4CzIPN) was synthesized according to the literature⁷.

2-4-2. Sample fabrication

All organic layers were formed by thermal evaporation under high-vacuum conditions ($< 10^{-4}$ Pa). Organic films with a thickness of 50 nm were grown on precleaned quartz substrates. The non-injecting devices were fabricated on clean tin-doped indium oxide (ITO) glass substrates and had an effective device area of 4 mm². The device structure for external-electric-field-modulated luminescence measurements was ITO (100 nm) / T2T (30 nm) / EML (100 nm) / CBP (30 nm) / aluminum (Al) (100 nm), with ITO as the anode, T2T as the hole-blocking layer, CBP and TPA-DCPP co-deposited as the emissive layer, neat CBP as the electron-blocking layer, and Al as the cathode. After device fabrication, the devices were immediately encapsulated with glass lids and epoxy glue in a dry nitrogen-filled glove box.

2-4-3. Measurement of photoluminescence properties

PLQY of the samples was measured using an absolute photoluminescence quantum yield measurement system (C11347-01, Hamamatsu Photonics). Absorption spectra and steady-state photoluminescence spectra were recorded on ultraviolet-visible (Lambda 950-PKA, PerkinElmer) and photoluminescence (FluoroMax-4, Horiba Jobin Yvon) spectrophotometers, respectively.

2-4-4. External-electric-field-modulated luminescence characterization

TRPL decay was measured using a fluorescence lifetime spectrometer (C11367, Hamamatsu Photonics) with a time-correlated single photon counting (TCSPC) method for measuring the time constant of TADF molecules. We also used a photo-sensor module (H10721-01, Hamamatsu Photonics), an amplifier unit (C11184, Hamamatsu Photonics), and an oscilloscope (WaveRunner 640Zi, Teledyne Lecroy) with a function generator (WaveStation2012, Teledyne Lecroy) as an external electric field source for observing the long-lived TRPL and external-electric-field-modulated TRPL profile measurements. A pulsed LED driving circuit was prepared as an excitation source to control the excitation pulse width, and a long-pass filter with an optical density of 6 was used for the extraction of the sample signal. All TRPL signals measured with the oscilloscope were averaged 10,000 times and normalized at the intensity just before turning off the photo-excitation.

2-4-5. Displacement current measurement

DCM was conducted using a current input preamplifier (LI-76, NF Corporation) and multifunction filter (3611, NF Corporation) with the oscilloscope and the function

generator as noted earlier. All DCM curves were measured with a sweep rate of 10 V s^{-1} at room temperature.

References

1. C. W. Tang and S. A. VanSlyke, Organic electroluminescent diodes. *Appl. Phys. Lett.* **51**, 913-915 (1987).
2. X. Xiong, F. Song, J. Wang, Y. Zhang, Y. Xue, L. Sun, N. Jiang, P. Gao, L. Tian and X. Peng, Thermally Activated Delayed Fluorescence of Fluorescein Derivative for Time-Resolved and Confocal Fluorescence Imaging. *J. Am. Chem. Soc.* **136**, 9590-9597 (2014).
3. J. Zhou, Q. Liu, W. Feng, Y. Sun and F. Li, Upconversion Luminescent Materials: Advances and Applications. *Chem. Rev.* **115**, 395-465 (2015).
4. M. G. Debijs and P. P. C. Verbunt, Thirty Years of Luminescent Solar Concentrator Research: Solar Energy for the Built Environment. *Adv. Energy Mater.* **2**, 12-35 (2012).
5. R. Kabe and C. Adachi, Organic long persistent luminescence. *Nature* **550**, 384-387 (2017).
6. C. A. Parker and C. G. Hatchard, Triplet-singlet emission in fluid solutions. Phosphorescence of eosin. *Trans. Faraday Soc.* **57**, 1894-1904 (1961).
7. H. Uoyama, K. Goushi, K. Shizu, H. Nomura and C. Adachi, Highly efficient organic light-emitting diodes from delayed fluorescence. *Nature* **492**, 234-238 (2012).
8. X.-K. Chen, D. Kim and J.-L. Brédas, Thermally Activated Delayed Fluorescence (TADF) Path toward Efficient Electroluminescence in Purely Organic Materials: Molecular Level Insight. *Acc. Chem. Res.* **51**, 2215-2224 (2018).
9. K. Tokumaru, Thermally activated delayed fluorescence: exploring the past to get insights into reverse and forward intersystem crossing. *J. Photonics Energy* **8**, 032109 (2018).
10. J. V. Caspar and T. J. Meyer, Application of the energy gap law to nonradiative, excited-state decay. *J. Phys. Chem.* **87**, 952-957 (1983).

11. H. Kuhn, Classical Aspects of Energy Transfer in Molecular Systems. *J. Chem. Phys.* **53**, 101-108 (1970).
12. A. Rao, P. C. Y. Chow, S. Gélinas, C. W. Schlenker, C.-Z. Li, H.-L. Yip, A. K. Y. Jen, D. S. Ginger and R. H. Friend, The role of spin in the kinetic control of recombination in organic photovoltaics. *Nature* **500**, 435-439 (2013).
13. S. Wang, X. Yan, Z. Cheng, H. Zhang, Y. Liu and Y. Wang, Highly Efficient Near-Infrared Delayed Fluorescence Organic Light Emitting Diodes Using a Phenanthrene-Based Charge-Transfer Compound. *Angew. Chem. Int. Ed.* **54**, 13068-13072 (2015).
14. J. T. Randall and M. H. F. Wilkins, Phosphorescence and electron traps II. The interpretation of long-period phosphorescence. *Proceedings of the Royal Society of London. Series A. Mathematical and Physical Sciences* **184**, 390-407 (1945).
15. H. Ohkita, W. Sakai, A. Tsuchida and M. Yamamoto, Charge Recombination Luminescence via the Photoionization of a Dopant Chromophore in Polymer Solids. *Macromolecules* **30**, 5376-5383 (1997).
16. S. Egusa, N. Gemma, A. Miura, K. Mizushima and M. Azuma, Carrier injection characteristics of the metal/organic junctions of organic thin-film devices. *J. Appl. Phys.* **71**, 2042-2044 (1992).
17. Y. Noguchi, N. Sato, Y. Tanaka, Y. Nakayama and H. Ishii, Threshold voltage shift and formation of charge traps induced by light irradiation during the fabrication of organic light-emitting diodes. *Appl. Phys. Lett.* **92**, 203306 (2008).
18. Y. Noguchi, Y. Miyazaki, Y. Tanaka, N. Sato, Y. Nakayama, T. D. Schmidt, W. Brütting and H. Ishii, Charge accumulation at organic semiconductor interfaces due to a permanent dipole moment and its orientational order in bilayer devices. *J. Appl. Phys.* **111**, 114508 (2012).
19. K. Osada, K. Goushi, H. Kaji, C. Adachi, H. Ishii and Y. Noguchi, Observation of spontaneous orientation polarization in evaporated films of organic light-emitting diode materials. *Org. Electron.* **58**, 313-317 (2018).
20. M. Pope and C. E. Swenberg, *Electronic processes in organic crystals and polymers*. (Oxford University Press on Demand, 1999), vol. 39.
21. K. Goushi and C. Adachi, Efficient organic light-emitting diodes through up-conversion from triplet to singlet excited states of exciplexes. *Appl. Phys. Lett.* **101**, 023306 (2012).

Chapter 3

Significant role of spin-triplet state for exciton dissociation in organic solids

Takahiko Yamanaka, Hajime Nakanotani & Chihaya Adachi

Science Advances **8**, eabj9188 (2022)

Abstract

Clarification of the role of the spin state that initiates exciton dissociation is critical to attaining a fundamental understanding of the mechanism of OPVs. Although an excited spin-triplet state with an energy lower than that of excited spin-singlet state is disadvantageous in exciton dissociation, a small electron exchange integral results in small singlet-triplet energy splitting in some material systems. This energy splitting leads to a nearly isoenergetic alignment of both excited states, raising a question about the role of excited spin states in exciton dissociation. Herein, we show that the spin-triplet rather than the spin-singlet plays a critical role in the exciton dissociation that leads to the formation of free carriers. This result indicates that the spin-triplet inherently acts as an intermediate, leading to exciton dissociation. Thus, our demonstration provides a fundamental understanding of the role of excited spin states of organic molecular systems in photoinduced charge-carrier generation.

3-1. Introduction

The role of spin states in the excited states of organic semiconductor materials has been extensively studied to elucidate the unique exciton dynamics inherent to the tightly bonded hole-electron pair in organic molecular systems. In particular, in organic optoelectronic devices such as OLEDs and OPVs, manipulating the excited spin states is critical for improving device performance¹⁻⁴. For example, the formation of low-energy triplet excitons via recombination of a photogenerated hole-electron pair is generally considered a major energy-loss pathway in D-A blend-type bulk heterojunction OPVs (BHJ-OPVs) (**Figure 3-1a**), leading to a low carrier extraction yield³⁻⁷. Thus, the rapid dissociation of excitons and the successive suppression of bimolecular recombination of the separated charge carriers have been widely considered to be requisites for OPVs with high photocarrier generation efficiency. Some state-of-the-art BHJ-OPVs have demonstrated nearly unity IQE for photocarrier generation⁸⁻¹⁰. However, in primarily CT-type excited spin states, it remains controversial which excited spin states play a critical role in exciton dissociation; various aspects of the role of excited spin states have therefore been investigated to attain a comprehensive understanding¹¹⁻¹³.

In general, an excited spin-triplet state with an energy lower than that of an excited spin-singlet state is disadvantageous for exciton dissociation events because it requires an input of external energy greater than the exciton binding energy of the excited spin-triplet state¹⁴. By contrast, the excited-state lifetime of an excited spin-triplet state is much longer than that of an excited spin-singlet state because of the weak spin-orbit coupling in molecules. Because exciton dissociation by an external electric field occurs within the exciton lifetime of molecules, their exciton lifetime should influence the exciton dissociation process¹⁵. Therefore, if the energy level of an excited spin-triplet is nearly

isoenergetically aligned with that of an excited spin-singlet, the question arises as to which excited spin state is advantageous for the charge separation events following the formation of the exciton (**Figure 3-1a**). This question has not yet been clarified for organic solid-state films, even though answering this question is critical for completely suppressing exciton losses in OPVs.

The ideal energy alignment of excited spin states in organic molecules and solid composites can be realized by a small electron exchange integral in their excited states. A proper combination of D-A units in molecular systems can well control the ΔE_{ST} , resulting in a ΔE_{ST} of tens of milli-electron volts. In these molecular systems, since the S_1 and T_1 states generally have a lowest CT excited-state character (1CT_1 and 3CT_1) and the energy is sufficiently lower than that of the locally excited spin-triplet state of a D or an A unit (3LE_1), intramolecular CT states are formed for both spin states when the molecule is excited optically or electrically. Then, the CT exciton can dissociate and diffuse to the adjacent molecules as a free carrier if the CT exciton overcomes the Coulomb binding energy, depicting the footprints of charge separation behavior. Therefore, such systems should provide an ideal platform to explore the role of excited spin states for understanding exciton dissociation processes.

A series of excitonic processes from exciton generation to charge separation (exciton dissociation) and recombination events similar to those in OPVs can be observed in organic thin films even without the aid of an external electrical field if the solid film is made of a molecular system that exhibits SOP¹⁶ (**Figure 3-1b**). The SOP induced by a spontaneous ordering of a permanent dipole moment of the molecules forms an internal potential slope of the electrical field¹⁷, working as a driving force in the charge separation as discussed in **Chapter 2**. In this case, the recombination of photogenerated holes and

electrons can be detected as long-lived luminescence, which can be categorized as previously reported LPL¹⁸. Although the fundamental driving force for LPL is attributed to charge separation based mainly on the Coulomb interaction between D and A molecules, the aforementioned long-lived emission (LLE) relies not only on the intermolecular Coulomb interaction but also substantially on the electric field that arises from SOP. In **Chapter 2**, the LLE reveals the presence of a nonnegligible PL quenching process in a solid-state film containing a polar fluorophore composed of a D-A combination. However, a deeper understanding of the role of the spin state in the exciton dissociation process had been unreachable. Hence, in the present study, conventional TRPL measurements are conducted to elucidate the role of excited spin states on spontaneous exciton dissociation in polar organic films that exhibit SOP and a small ΔE_{ST} . Our work clarifies that excited spin-triplet states act as an efficient “intermediate excited-state bath,” leading to the successive exciton dissociation process in solid thin films.

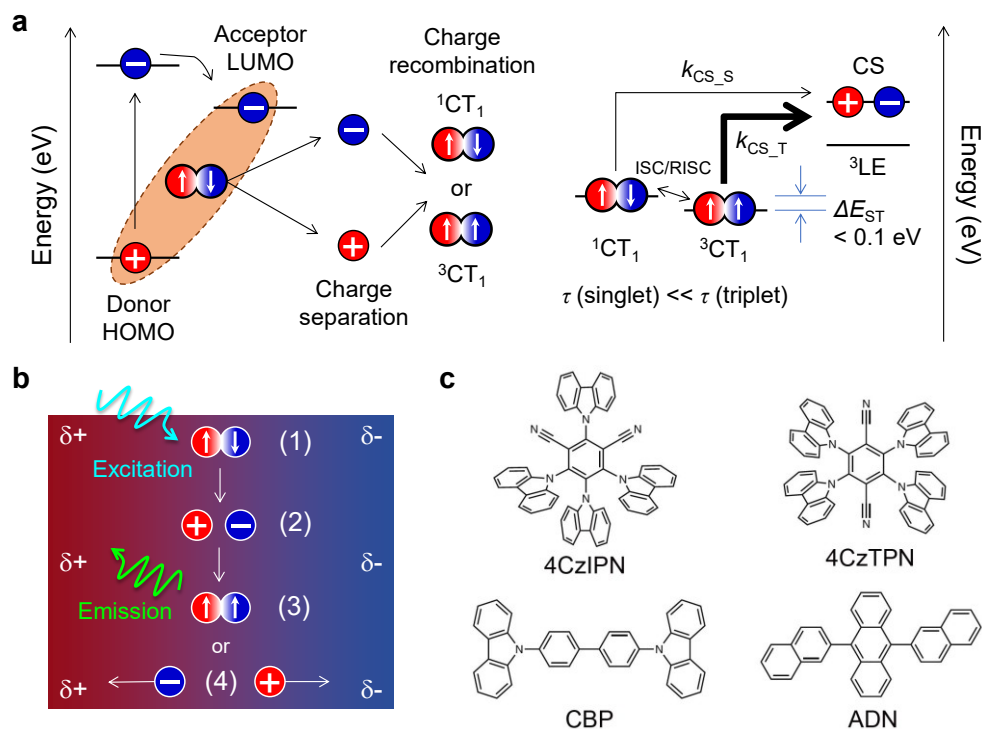


Figure 3-1. Key photophysical process of charge-transfer-type exciton. **(a)** Left: Photophysical process in an organic D-A system, i.e., photocarrier generation via dissociation of the charge-transfer exciton (CTE) and the formation of $^1\text{CT}_1$ and $^3\text{CT}_1$ via bimolecular recombination during carrier diffusion. Right: Excited-state energy-level diagram to investigate the role of the excited spin state in the exciton dissociation process. Here, CS and τ represent the carrier separation state and the exciton lifetime, respectively. **(b)** Schematic of spontaneous exciton dissociation in a polar organic film. Process (1): CTE generation by photoexcitation. Process (2): Spontaneous dissociation of the CTE by the SOP of the film. Process (3): Bimolecular recombination between the dissociated carriers. Process (4): Charge-carrier diffusion and accumulation at the interface. **(c)** Molecular structures of the compounds used in this study.

3-2. Results and discussion

Figure 3-1c and **Figure 3-2** show the chemical structures and the energy levels for two fluorophores and two wide-energy-gap molecules used as emitters and host matrices, respectively. Because 4CzIPN and 4CzTPN have a small ΔE_{ST} of 0.01 and 0.06 eV, respectively, these molecules are well known to function as efficient TADF emitters in

OLEDs^{2, 19}. Note that 4CzIPN has a permanent dipole moment ($\mu_D = 3.8$ Debye), whereas 4CzTPN is a nonpolar molecule because of its symmetric molecular structure. For the host matrix, CBP was chosen as a triplet-activated host because the T_1 state of CBP (2.55 eV) is higher than those of 4CzIPN (2.48 eV) and 4CzTPN (2.28 eV). By contrast, because the T_1 state for ADN (1.69 eV)²⁰ is much lower than those for 4CzIPN and 4CzTPN but the S_1 state can confine the S_1 states for 4CzIPN and 4CzTPN, the ADN matrix functions as a triplet-scavenging host (**Figure 3-2**).

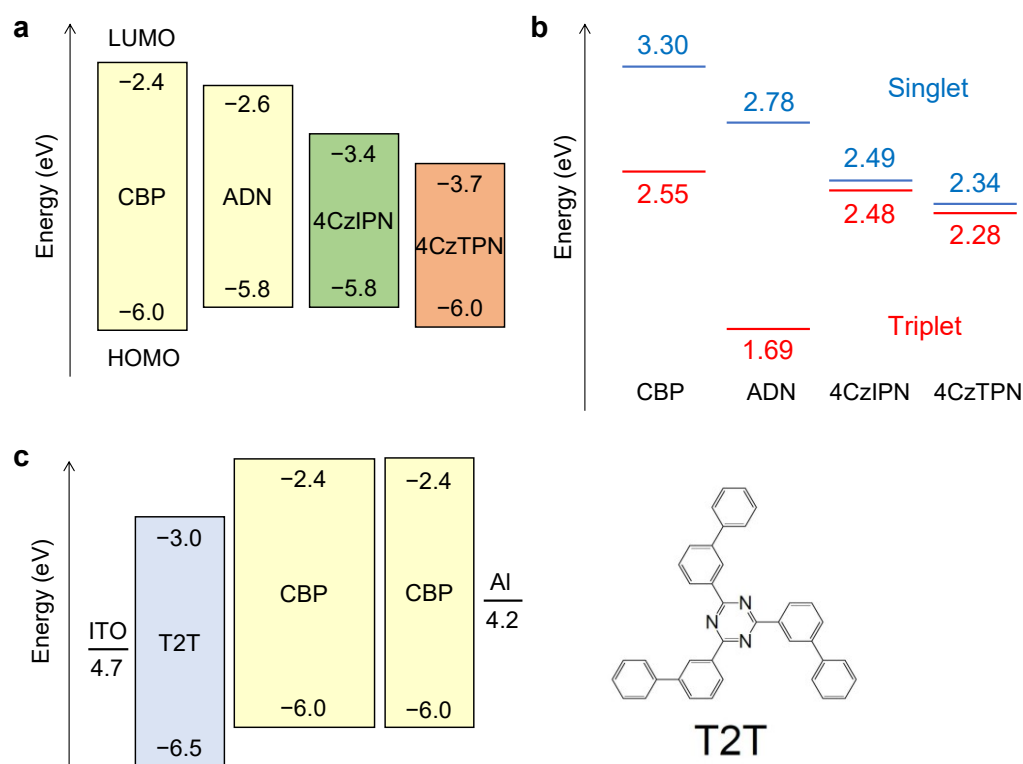


Figure 3-2. Energy-level diagram of fluorophores and host molecules. **(a)**, **(b)** Energy levels (HOMO, LUMO, singlet, and triplet) for organic fluorophores with a small ΔE_{ST} (4CzIPN and 4CzTPN) and host molecules (CBP and ADN) used in this study. **(c)** Energy-level diagram of the NCI-type device and the molecular structure of T2T.

Figure 3-3a shows the TRPL profiles for 4CzIPN or 4CzTPN doped into a CBP

host matrix with a doping concentration of 50 wt %. Here, the excitation light with a wavelength of 430 nm was used to directly excite the absorption band of the fluorophores (**Figure 3-4**). In the case of the 4CzIPN:CBP film, after the photoexcitation light was turned off, two components in the emission decay were observed in the measurement time range of ~2 ms: an inherent radiative decay due to 4CzIPN (i.e., delayed fluorescence of singlet excitons generated via a reverse intersystem crossing from the T_1 state) and an LLE decay arising from slow recombination of charge carriers dissociated from the 4CzIPN excitons (see schematic in **Figure 3-1b**). Note that the prompt decay component based on the singlet excitons in 4CzIPN is buried in the first component because of the nanosecond decay. By contrast, no LLE was observed in the profile of the 4CzTPN:CBP film. Here, we conducted atomic force microscopy measurements to confirm the microstructures of each film (**Figure 3-5**). The almost flat surface with an average roughness between 0.28 and 0.36 nm was observed in all films, indicating no substantial difference in the microstructures.

First, the absence of LLE in the 4CzTPN:CBP film is attributed to the lack of an SOP (i.e., σ_{int}) in the film. To calculate the σ_{int} , displacement current measurements (DCMs)²¹ were conducted for a diode with a configuration of indium tin oxide (ITO) (100 nm)/ α -NPD (50 nm)/4CzIPN:CBP or 4CzTPN:CBP (50 nm)/Al (100 nm). The onset voltage was lower than 0 V for the 4CzIPN:CBP diode, as shown in **Figure 3-3b**, which is attributed to charge accumulation ($\sigma_{\text{int}} = -1.79 \text{ mC m}^{-2}$) at the α -NPD/4CzIPN interface¹⁷, indicating the occurrence of SOP inside the 4CzIPN:CBP layer. Because no net carrier accumulation at the α -NPD/4CzTPN interface was observed from the current density–voltage characteristics (**Figure 3-3b**), these results indicate that the occurrence of SOP in the film is a critical mechanism for the spontaneous dissociation of

the excitons.

Notably, the excitons of both fluorophores can also dissociate upon application of an external voltage to the films, which is similar to the case of OPVs. **Figure 3-3c** shows the TRPL profiles recorded when a negative voltage pulse (200 μ s width) was applied during photoexcitation in noncarrier-injecting (NCI)-type devices with a structure of ITO (100 nm)/T2T (30 nm)/4CzIPN:CBP or 4CzTPN:CBP (100 nm)/CBP (30 nm)/ Al (100 nm) (**Figure 3-2c**). For both fluorophores, the steady-state PL intensity during photoexcitation was attenuated by the external voltage pulse, clearly indicating the occurrence of exciton dissociation (inset of **Figure 3-3c**). After the excitation light was turned off, the LLE was observed even in the 4CzTPN:CBP NCI device with an applied external negative voltage during photoexcitation. The LLE appearance was attributed to the photogeneration of excitons and subsequent exciton dissociation into holes and electrons because of the external bias. An electric field-modulated EL enhancement was also observed for the 4CzTPN:CBP NCI device under a negative voltage offset, whereas no EL spike was observed at 0 V offset (**Figure 3-6**). Therefore, these observations indicate that the charge carriers generated by the dissociation of excitons can essentially maintain a stable state at least on the millisecond time scale in both triplet-activated films. Here, in the 4CzIPN:CBP NCI device, the emission undershoot and overshoot were observed at the pulse fall (0 to -10 V) and the pulse rise (-10 to 0 V), respectively. The undershoot corresponds to a non-equilibrium state immediately after applying the negative voltage pulse. The overshoot is the momentary recombination of charge carrier which accumulate at EML/CBP and EML/T2T interfaces.

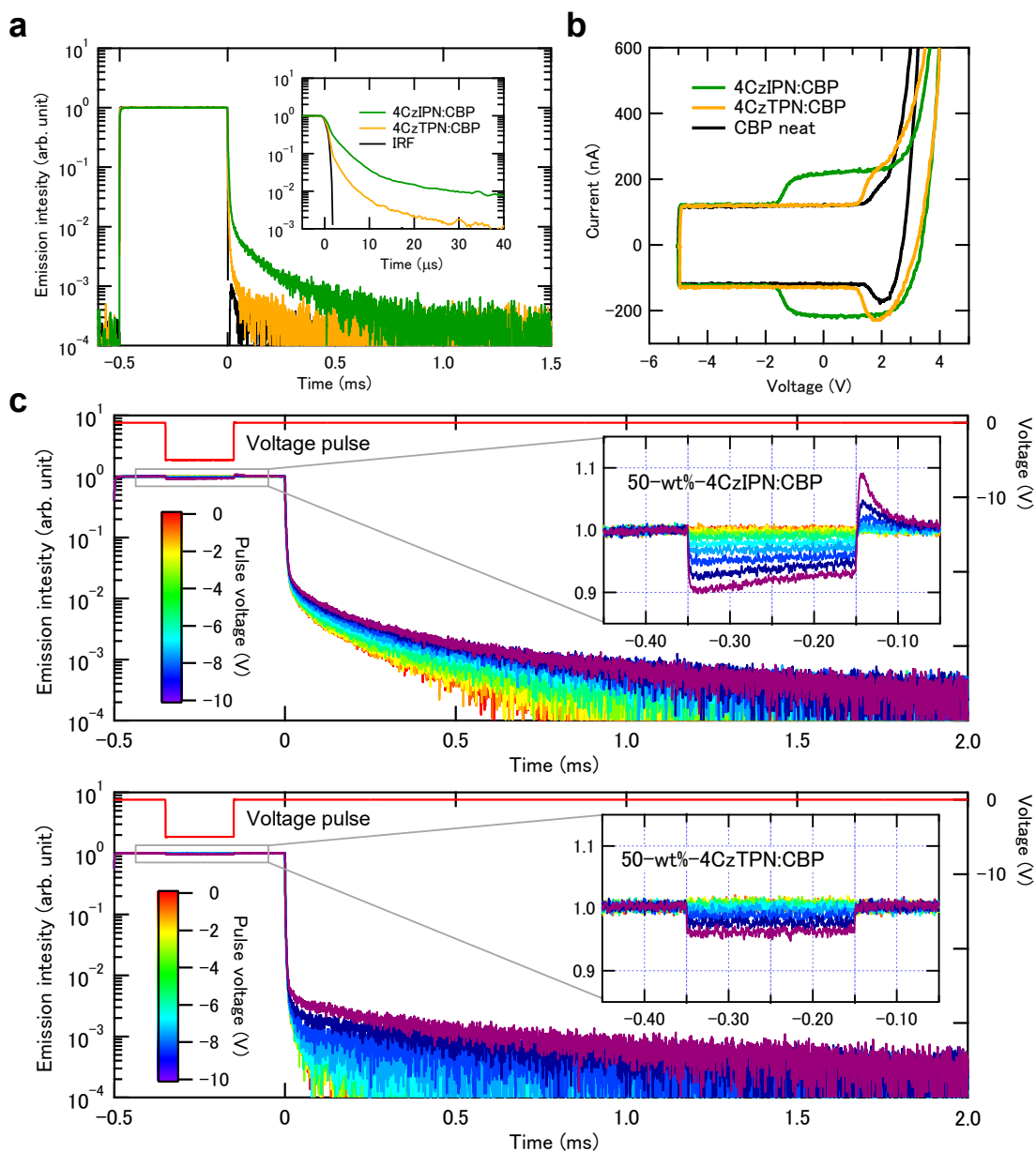


Figure 3-3. Photoluminescence characteristics of 4CzIPN and 4CzTPN in a triplet-activated CBP host matrix. **(a)** TRPL profiles of 4CzIPN:CBP and 4CzTPN:CBP blend films. A 430-nm LED was used as excitation light, and the light pulse width and the power were fixed at 500 μ s and 20 mW cm $^{-2}$, respectively. The lifetime of the LLE component is much longer than the intrinsic TADF lifetime for 4CzIPN. **(b)** DCM profiles of the 4CzIPN- and 4CzTPN-based diodes. The doping concentration of each fluorophore was fixed at 50 wt %. **(c)** Electrically modulated TRPL profile in NCI-type devices based on CBP:4CzIPN (top) and CBP:4CzTPN (bottom). A negative voltage pulse with different voltages with a pulse width of 200 μ s was applied to the sample during photoexcitation. The inset shows an enlarged view of the TRPL profile during photoexcitation.

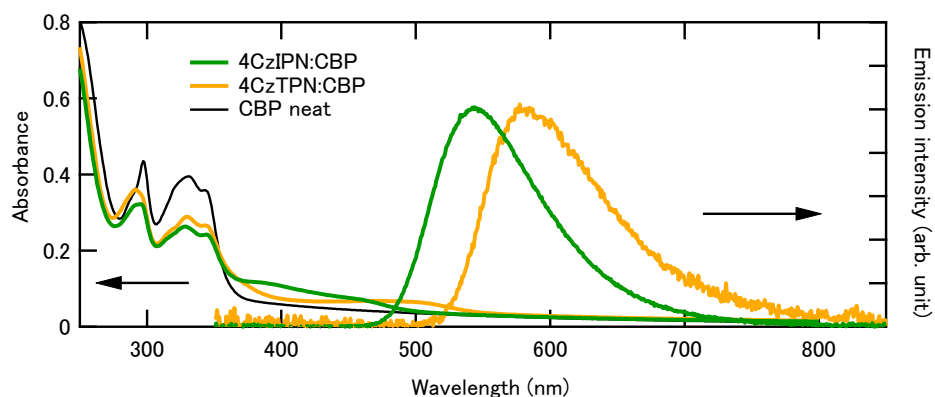


Figure 3-4. Absorption and fluorescence spectra of 4CzIPN:CBP, 4CzTPN:CBP, and CBP films. The doping concentration of fluorophores was fixed at 50 wt% for each co-deposited film.

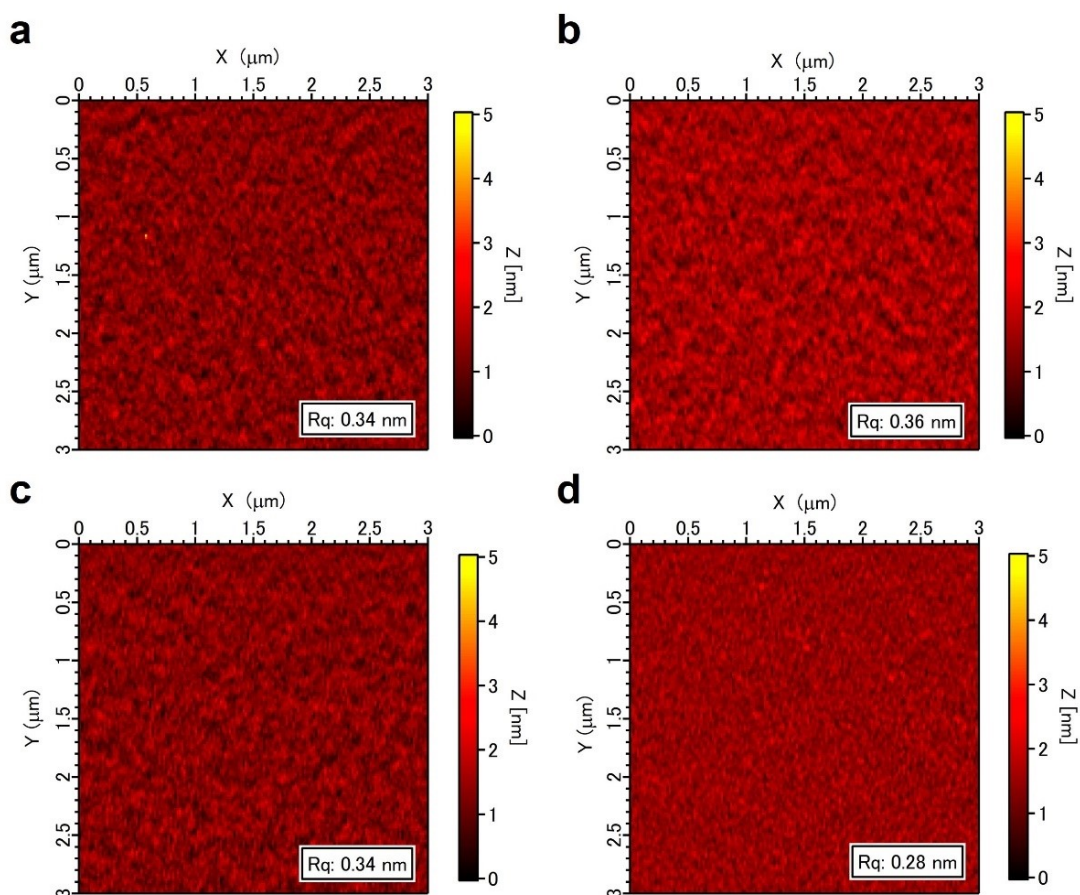


Figure 3-5. AFM images of solid-state films. (a) 50-wt%-4CzIPN:CBP. (b) 50-wt%-4CzTPN:CBP. (c) 50-wt%-4CzIPN:ADN. (d) neat 4CzIPN. The root-mean-square roughness (R_q) is less than 0.5 nm in all samples.

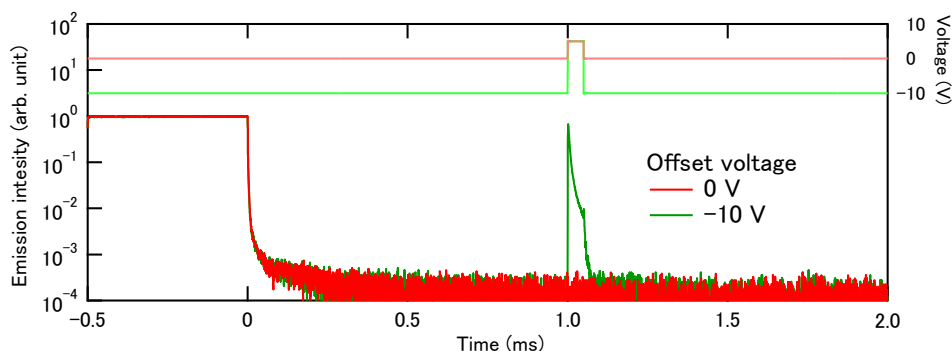


Figure 3-6. Dependence of the external-electric-field-modulated TRPL profiles on the offset voltage during the measurement in the 50-wt%-4CzTPN:CBP NCI device. The applied voltage and width were fixed at 5 V and 50 μ s, respectively.

Next, we discuss the role of the excited spin states on the exciton dissociation process. We first investigate the role of the $^3\text{CT}_1$ of 4CzIPN on the dissociation process by incorporating ADN as a triplet-scavenging host molecule. Notably, the σ_{int} of a 4CzIPN:ADN layer (-1.56 mC m^{-2}) is similar to that of a 4CzIPN:CBP layer (-1.79 mC m^{-2}), indicating the same level of SOP for both films (**Figure 3-7a**). The TADF component of 50-wt%-4CzIPN doped in the ADN host is substantially quenched (**Figure 3-8**), resulting in a PLQY of 15% that corresponds to the prompt (fluorescence) PLQY in the 4CzIPN:CBP film (28%). This result indicates that the triplet excitons of 4CzIPN are substantially quenched by the $^3\text{LE}_1$ of ADN via Dexter-type triplet energy transfer²².

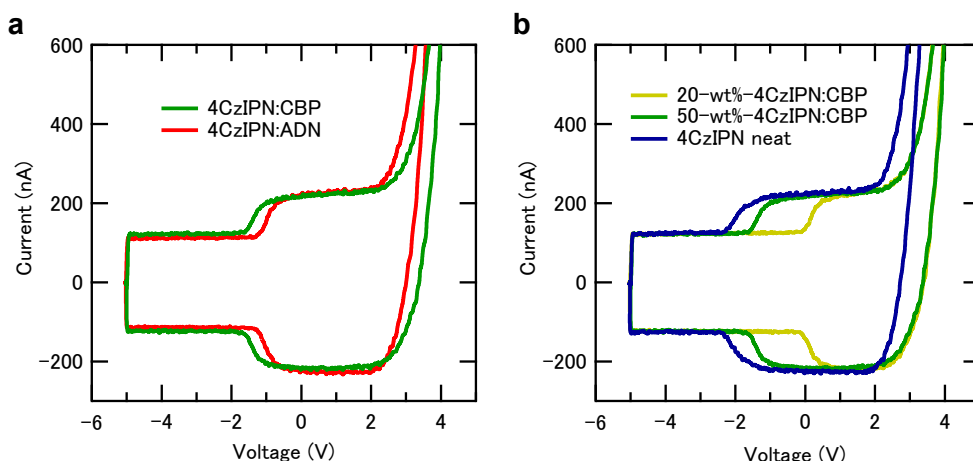


Figure 3-7. DCM profile of 4CzIPN-based diodes. **(a)** Dependence of the DCM profile in the 4CzIPN-based diode on the host matrix. The doping concentration of the 4CzIPN was fixed at 50 wt%. **(b)** Dependence of the DCM profile for the 4CzIPN:CBP-based diode with the 4CzIPN concentration of 20 wt% and 50 wt% and the neat 4CzIPN film.

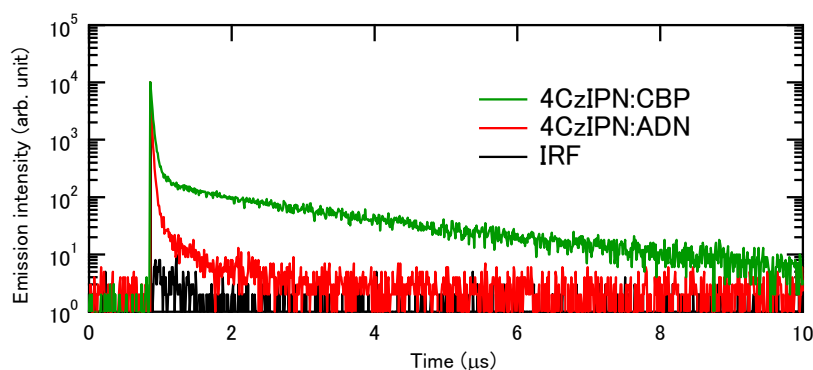


Figure 3-8. TRPL profiles of 4CzIPN:CBP and 4CzIPN:ADN blend films. The doping concentration of the 4CzIPN was fixed at 50 wt%. The black line indicates the IRF of the fluorescence lifetime spectrometer used for the measurements.

The LLE component was substantially diminished in the TRPL profile for the 4CzIPN:ADN film (**Figure 3-9a**), indicating that the unique photophysical characteristics of ADN control the disappearance of the photogenerated holes and electrons in the 4CzIPN:ADN film. We can attribute this phenomenon to either (i) the low exciton dissociation yield in the triplet-deactivated film or (ii) the nonradiative decay from the

$^3\text{LE}_1$ of ADN. The arguments for these hypotheses are discussed as follows:

1) The SOP for a 4CzIPN:CBP film becomes larger nonlinearly with increasing concentration of polar 4CzIPN molecules (**Figure 3-7b**) because of the peculiar intermolecular dipole–dipole interaction between neighboring 4CzIPN molecules^{23, 24}, whereas the LLE decay in TRPL becomes shorter (**Figure 3-10**). The attenuation of the LLE component with increasing 4CzIPN concentration implies that fewer charge carriers are dissociated from the 4CzIPN excitons. However, the LLE intensity should be influenced not only by the charge-carrier density but also by the change in carrier recombination probability, which depends on the trap density or carrier transport ability of the film. Hence, to study the charge separation dynamics in greater detail, we conducted PLQY measurements of 4CzIPN:CBP films (**Figure 3-9b**). The PLQY for the TADF component (i.e., the contribution of $^3\text{CT}_1$) decreases with increasing doping concentration, whereas the PLQY for the prompt component remains almost the same, suggesting that the number of active triplet excitons is correlated with the dissociation probability. We then evaluated the electrical field–modulated TRPL in the 50-wt%-4CzIPN:CBP and the neat 4CzIPN NCI devices to directly confirm the spin-selective exciton dissociation. Even though the steady-state PL intensity for the 50-wt%-4CzIPN:CBP NCI device was lowered when an external voltage pulse was applied, as illustrated in the inset of **Figure 3-3c**, the neat 4CzIPN NCI device was unaffected by applying an external electric field (**Figure 3-11**). Furthermore, the delayed component (intrinsic delayed fluorescence lifetime via $^3\text{CT}_1$) in the 50-wt%-4CzIPN:CBP NCI device with a negative voltage was appreciably attenuated compared with that of the device without an electric field, whereas the prompt decay component was unchanged (**Figure 3-9c**). Also, virtually no electrical field modulation of either the prompt or the

delayed component was observed in the TRPL profiles of the 4CzIPN neat NCI device (**Figure 3-9d**). Notably, in the case of the neat films, although the SOP is larger than the doped films as indicated by **Figure 3-7b**, some of the 4CzIPN molecules should have been insusceptible to SOP and external electric fields due to the cancellation of the dipoles or no specific interaction with CBP molecules. These results clearly suggest that the charge separation event after the formation of the excitonic states occurs selectively via the excited spin-triplet state and that the dissociation probability of the singlet excitons, contributing to the rapid radiative relaxation, is negligibly low (**Figure 3-9e**). The relaxation time of the PL quenching after applying the external electric field is over several microseconds in the 4CzIPN:CBP NCI device, indicating that the charge carriers are formed slowly (**Figure 3-12**).

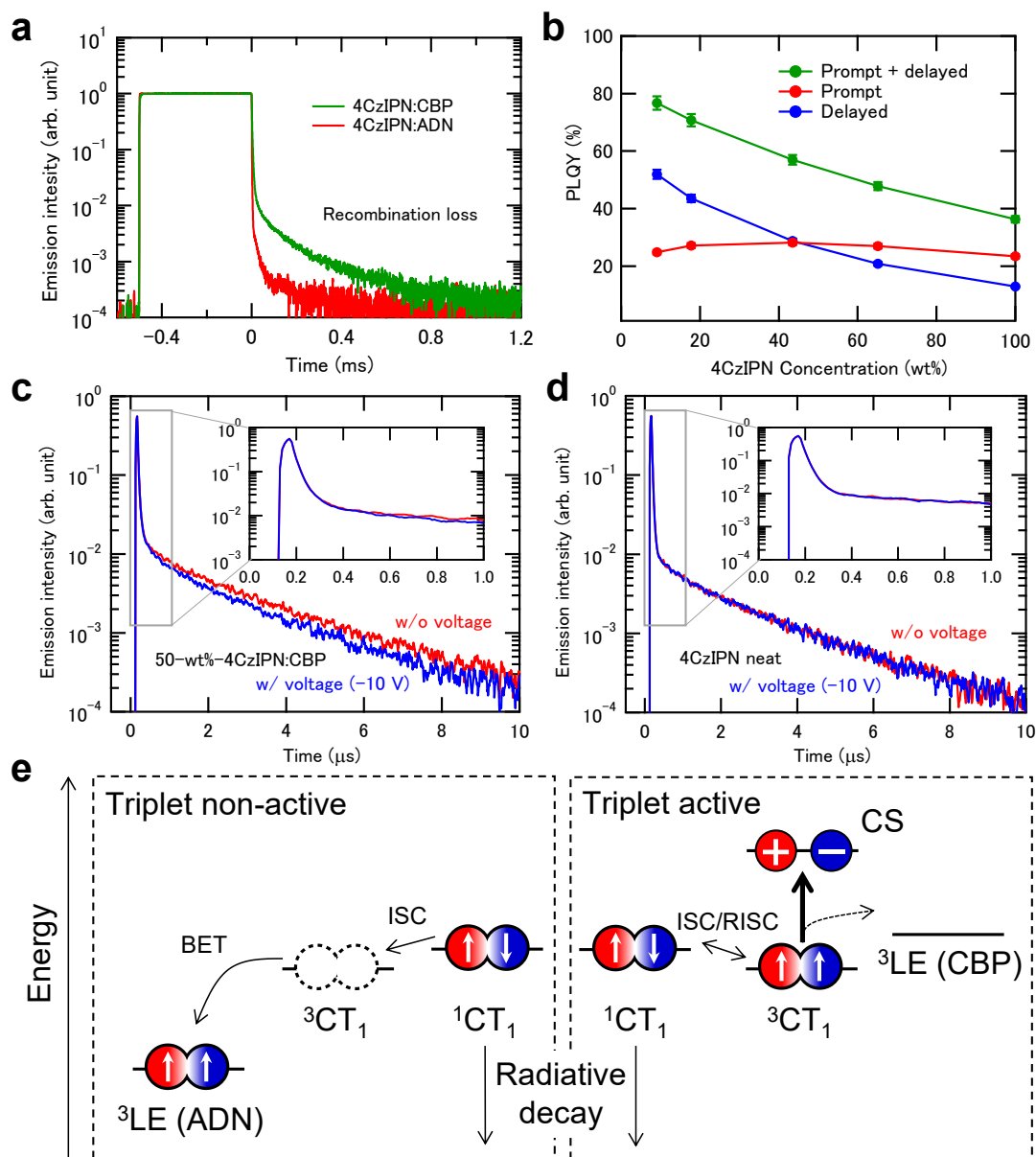


Figure 3-9. PL characteristics of 4CzIPN in a triplet-activated and deactivated host matrix. (a) TRPL profile in 4CzIPN:CBP and 4CzIPN:ADN blend films. The doping concentration of 4CzIPN for each host matrix was fixed at 50 wt %. (b) Concentration dependence of PLQY for prompt and delayed components in 4CzIPN:CBP blends. The error bars were estimated by considering experimental variability. (c, d) Emission decay profiles in NCI devices consisting of 50-wt%-4CzIPN:CBP or 4CzIPN under an electric field. The DC voltage was fixed at -10 V. Delayed fluorescence lifetimes of the 50-wt%-4CzIPN:CBP and the neat 4CzIPN film without voltage are 2.34 and 1.86 μs , respectively. (e) Schematic of the role of the excited spin state on the exciton dissociation process.

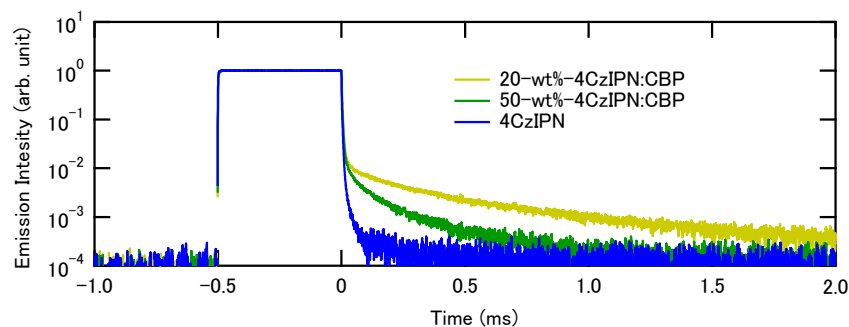


Figure 3-10. Dependence of the TRPL decay profile in 20 wt% and 50 wt%-4CzIPN:CBP films and the neat 4CzIPN film.

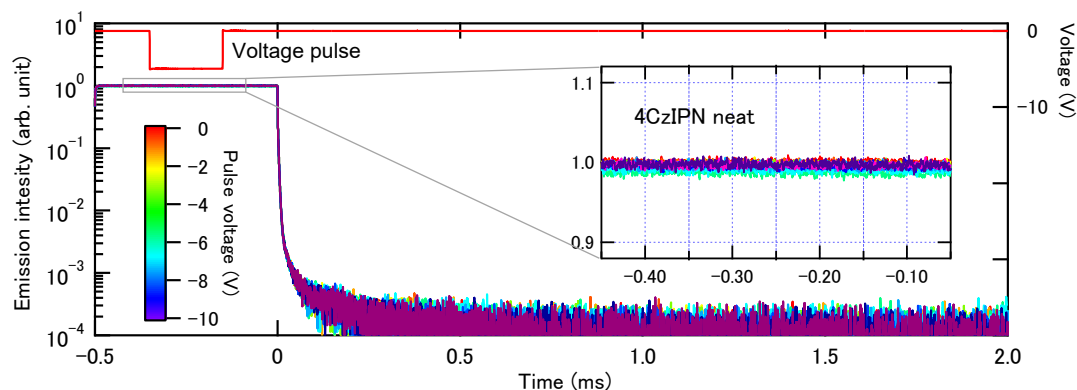


Figure 3-11. Electrically modulated TRPL profile in a neat 4CzIPN-based NCI-type device. Negative voltage pulses with different voltages and a pulse width of 200 μ s were applied to the sample during photoexcitation. The inset represents an enlarged view of the TRPL profile during photoexcitation.

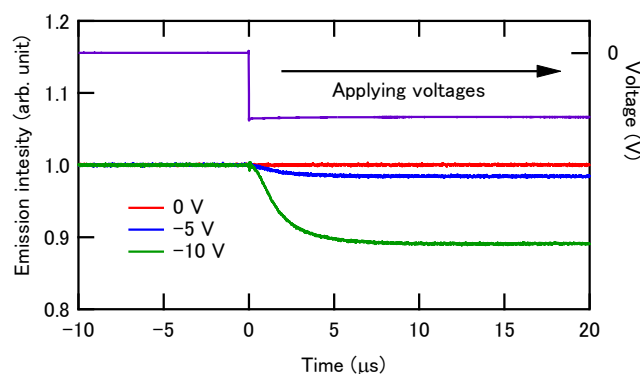


Figure 3-12. Electrically modulated TRPL profile in a 50-wt%-4CzIPN:CBP NCI device (High-resolution range). Negative voltage pulses with different voltages were applied to the sample during photoexcitation.

Because the $^3\text{CT}_1$ lifetime (τ_d) of 2.3 μs is appreciably longer than the $^1\text{CT}_1$ lifetime (τ_p) of 30 ns in the case of 50-wt%-4CzIPN:CBP, we interpret this phenomenon as the spontaneous exciton dissociation from the long-lived $^3\text{CT}_1$ of 4CzIPN, which would be favorable compared with dissociation from the energetically closed $^1\text{CT}_1$. Notably, the radiative decay from the $^1\text{CT}_1$ to the k_r of $9.3 \times 10^6 \text{ (s}^{-1}\text{)}$ and the k_{ISC} of $2.4 \times 10^7 \text{ (s}^{-1}\text{)}$ should both be faster than the exciton dissociation in this molecular system. However, we considered that the low dissociation probability in the 4CzIPN neat is attributable to the competition between the exciton dissociation and the nonradiative relaxation in the triplet excited state. Several groups have reported that concentration quenching of 4CzIPN is due to intermolecular interaction that originates from an electron exchange between neighboring molecules following a nonradiative decay from the T_1 to the ground state^{25, 26}. According to the literature 25, the molecular distances of 50-wt%-4CzIPN:CBP and neat 4CzIPN can be calculated to be 1.4 and 1.0 nm, respectively. Then, we estimated the rate constant of Dexter energy transfer (k_{DET}) which correlates with concentration quenching of triplets is described by the following equation:

$$k_{\text{DET}} = \left(\frac{4\pi^2}{h} \right) K^2 \exp \left(-\frac{2r}{L} \right) \int f_{\text{H}}(\nu) F_{\text{G}}(\nu) d\nu$$

where r is molecular distance, and L is the effective average Bohr radius. Here, the L is assumed to 1.0 nm at most by taking into account the molecular size and CT exciton character of 4CzIPN. In this case, k_{DET} for the 4CzIPN neat film is calculated to be 2.2 times higher than that of a 50-wt%-4CzIPN doped film, which is sufficient to accelerate the concentration quenching. In fact, the PL decay of the TADF component in the neat film is clearly attenuated as shown in **Figure 3-13**. Hence, we considered that the concentration-dependent non-radiative triplet deactivation is one of the critical factors for exciton dissociation. Although the dependence of PLQY on the 4CzIPN doping

concentration (**Figure 3-9b**) shares a similar trend with the result in the literature 25, note that the absolute value of PLQY in the literature 25 is much lower than that of our results especially in the high-doping concentration region. One possibility for the origin of the difference in PLQY is speculated to be a difference in material purity because the PL characteristics of organic material are extremely sensitive to its purity. Although it is impossible to directly compare the material purity, we note that all experiments in this study were carried out using the highly purified 4CzIPN powder with the guaranteed traceability for the purity (**Figure 3-14**). In addition, to obtain supplementary evidence for the dissociation from triplet excited states, we studied a 50-wt%- Alq₃:CBP NCI device that completely deactivates triplet excitons. Because the steady-state PL intensity in this device was unchanged when an external electric field was applied, as in the case of the 4CzIPN neat NCI device (**Figure 3-15**), the low dissociation probability for singlet excitons is again confirmed.

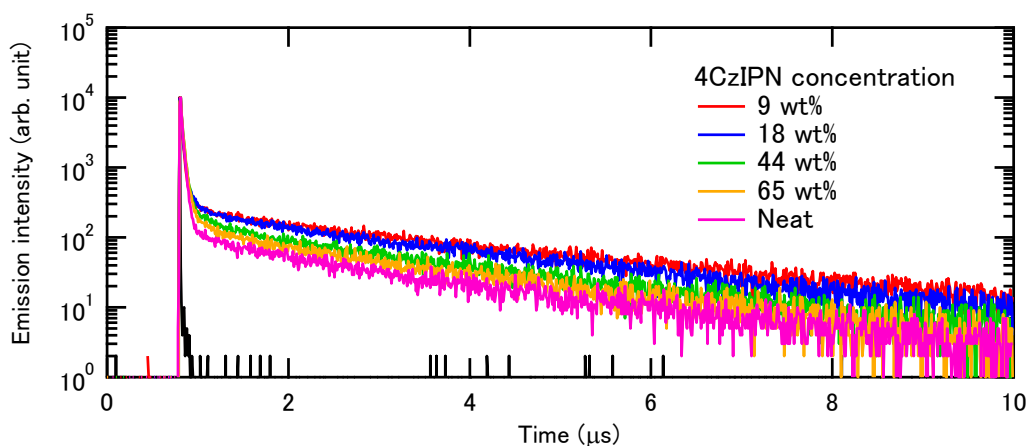


Figure 3-13. TRPL profile of 4CzIPN:CBP co-deposited films. The black line indicates the IRF of the fluorescence lifetime spectrometer used for the measurements.

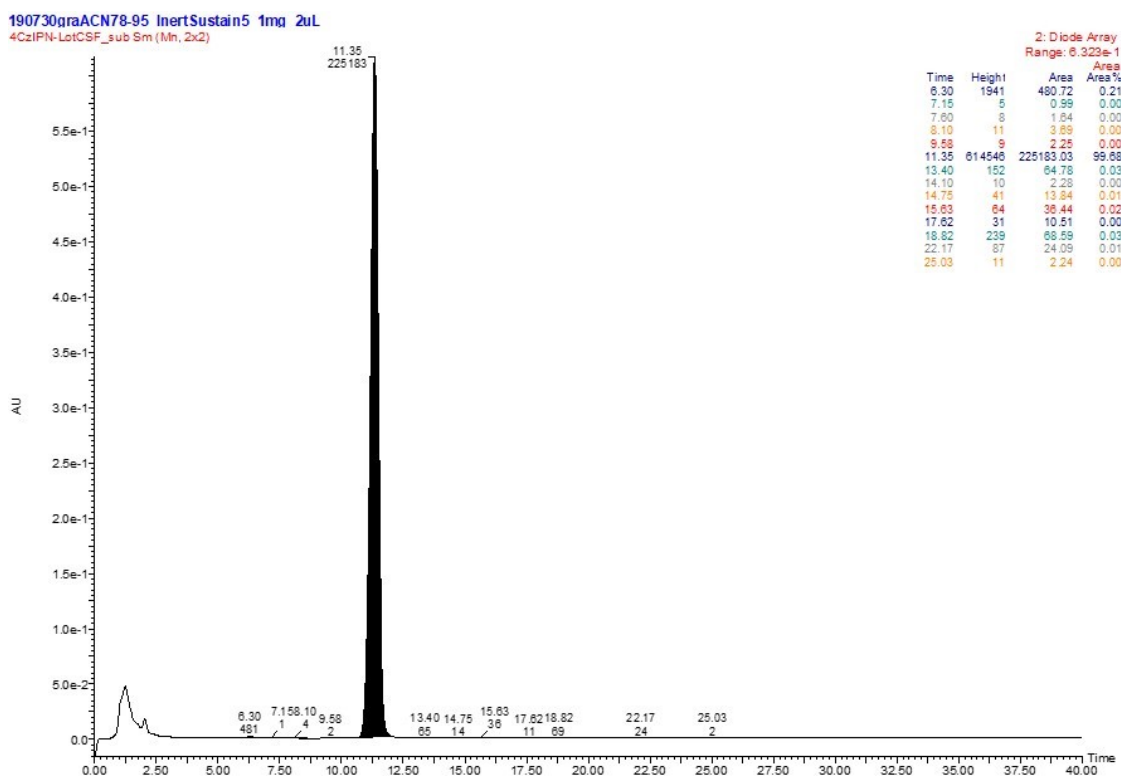


Figure 3-14. High-performance liquid chromatography (HPLC) for 4CzIPN using in this study. HPLC purity of 4CzIPN is over 99.5%.

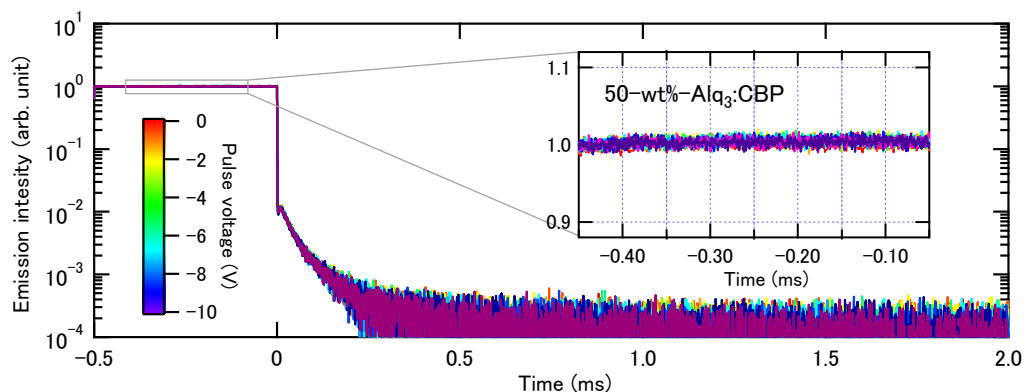


Figure 3-15. Electrically modulated TRPL profile in a 50-wt%-Alq₃:CBP-based NCI-type device. Negative voltage pulses with different voltages and a pulse width of 200 μ s were applied to the sample during photoexcitation. The inset represents an enlarged view of the TRPL profile during photoexcitation. Note that the delayed components after turn-off the excitation light might be ascribed to the hot excitons that are generated before decay to the S₁ state (*Ref.* 27).

We also observed the electric field–modulated EL enhancement in the 4CzIPN NCI devices (**Figure 3-16**). The EL spike intensity for the 50-wt%-4CzIPN:CBP NCI device was greater than that for the neat 4CzIPN NCI device, again indicating a low charge-separation efficiency in the 4CzIPN neat NCI device. This result is supported by the absorbed photon-electron conversion efficiency, namely, a full-wavelength IQE, measurements for the 4CzIPN diodes (**Figure 3-17a**). The IQE at the wavelength of 430 nm was elevated from 3 to 26% in the 50-wt%-4CzIPN:CBP diode with an increase in the negative bias, whereas an increase in the low IQE from 2 to 8% was observed for the neat 4CzIPN diode (**Figure 3-17b**). Note that the charge separation originated from 4CzIPN is ensured, since the wavelength longer than 420 nm is not absorbed by the hole transport layer of α -NPD (**Figure 3-17c**). Moreover, the intensity of the normalized IQE spectra in the 50-wt%-4CzIPN:CBP diode was increased with an increase in the negative bias although that of the neat 4CzIPN diode showed almost no change (**Figure 3-17d**). This spectral change means that the acceleration of the triplet exciton dissociation depends on the external electric field. Here, the time constant for the delayed component for the neat 4CzIPN diode is virtually independent of the applied voltage (**Figure 3-9d**) and exciton dissociation from the triplet state is negligible. Instead, the smaller IQE for the neat 4CzIPN diode might be attributable to carrier generation from the hot CT state, in which the charge generation is independent of the electric field by the aid of the extremely rapid process with excess energy²⁷.

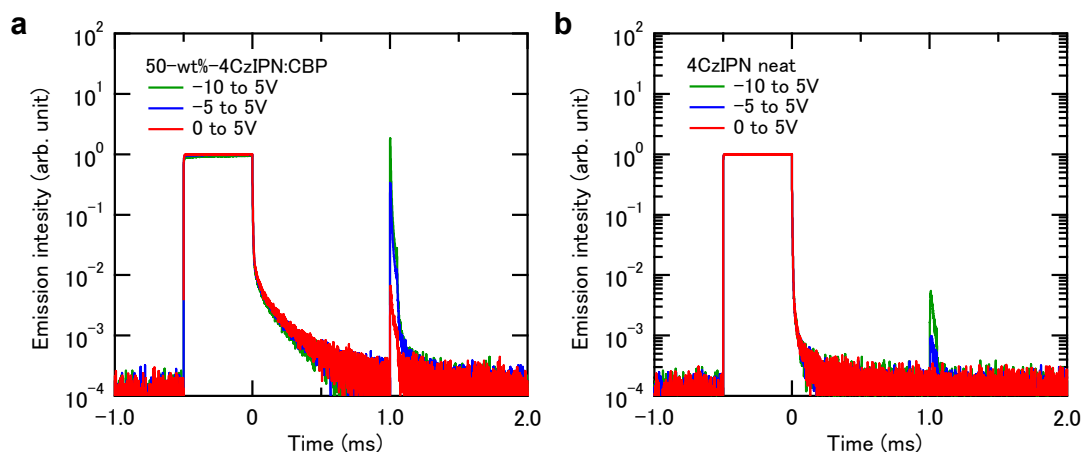


Figure 3-16. Charge-separation efficiency in 4CzIPN-based NCI devices. **(a, b)** External-electric-field-modulated TRPL profiles for 50-wt%-4CzIPN:CBP- and neat 4CzIPN-based NCI devices. The applied voltage width was fixed at 50 μ s. Apparently, 50-wt%-4CzIPN:CBP device showed larger EL with the application of pulse voltages compared with those of the neat 4CzIPN device. The small appearance of the EL might be ascribed to the hot excitons that are generated before decay to the S_1 state (*Ref.* 27).

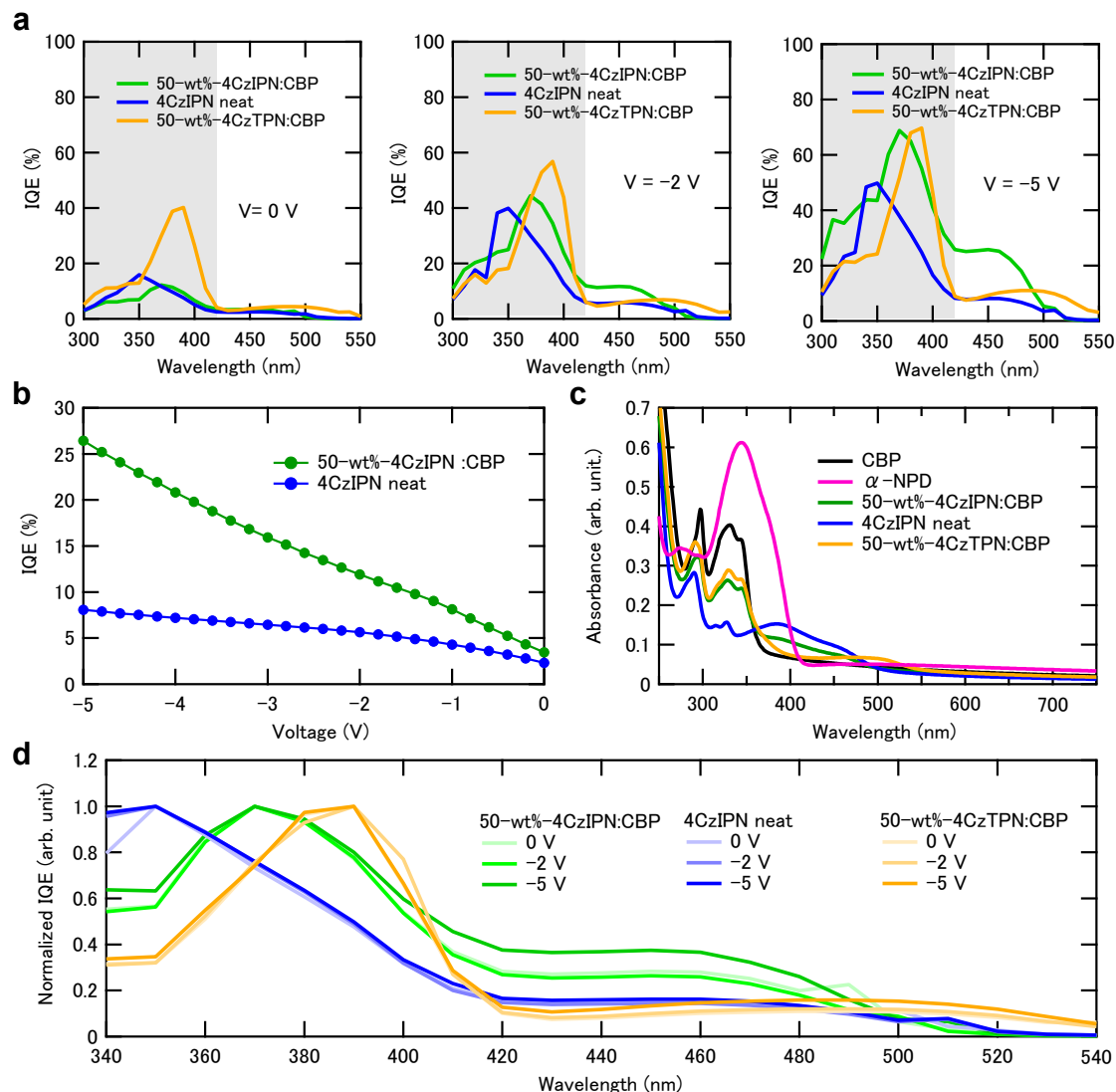


Figure 3-17. IQE of the diode including 50-wt%-4CzIPN:CBP, neat 4CzIPN, and 50-wt%-4CzTPN:CBP. **(a)** Full wavelength IQE as a function of voltage. Note that the IQE of 50-wt%-4CzTPN:CBP diode at 0V is speculated to be assigned to the exciton dissociation owing to the internal electric field induced by the electrodes with different work functions. **(b)** Dependence of IQE on the 4CzIPN doping concentration in a 4CzIPN-based diode at 430 nm excitation. **(c)** Absorption spectra of material comprising the diodes for IQE measurements. **(d)** Normalized IQE spectra on each voltage.

Returning our attention to **Figure 3-3c**, we observe that the decrease in the PL intensity when the negative voltage pulse was applied is substantially smaller for the 4CzTPN:CBP NCI device than for the 4CzIPN:CBP NCI device despite the similar electrical field. A comparison of the prompt:delay ratio for the doped films reveals that the ratio is 1:1 for the 4CzIPN:CBP film and 4:1 for the 4CzTPN:CBP film (**Table 3-1**). Assuming that exciton dissociation from the $^3\text{CT}_1$ state is more likely than that from the $^1\text{CT}_1$ state, as previously mentioned, the 4CzIPN:CBP NCI device is expected to be more easily quenched because of the large population of the $^3\text{CT}_1$ state. The IQE of the 50-wt%-4CzIPN:CBP diode was elevated largely by applying the negative bias, compared to that of the 50-wt%-4CzTPN:CBP diode (**Figure 3-17a**). These observations support our hypothesis that the exciton dissociation from the $^3\text{CT}_1$ state is critical (**Figure 3-9e**). Here, note that a small IQE value around the visible region has been observed even in the 50-wt%-4CzTPN:CBP diode at 0 V, and it is slightly larger than that of the 4CzIPN:CBP diode. It would be due to the exciton dissociation by the internal electric field induced by the difference of work function on each electrode, and the effective transport of charge carriers in the diode because the HOMO levels of 4CzTPN and CBP are almost the same.

Table 3-1. Photophysical properties of 50-wt%-4CzIPN and 4CzTPN in CBP.

Compound	Prompt PLQY (%)	Delayed PLQY (%)	τ_p (ns)	τ_d (μs)	k_r (10^7 s^{-1})	k_{ISC} (10^7 s^{-1})	k_{RISC} (10^5 s^{-1})
4CzIPN:CBP	28.2	28.8	30.3	2.34	0.93	2.37	6.07
4CzTPN:CBP	12.2	3.1	11.6	1.75	1.04	7.55	1.68

2) In addition to the initial carrier density in the 4CzIPN:ADN film being reduced, the small amount of charge carriers generated from the 4CzIPN excitons would be consumed as heat by the production of $^3\text{LE}_1$ of ADN through the Dexter event. Thus, the

LLE intensity became much weaker than that in the 4CzIPN:CBP case. Moreover, the 4CzIPN:ADN NCI device showed no EL response under an applied positive voltage pulse after the excitation light was turned off (**Figure 3-18**), whereas a clear response was observed in the 4CzIPN:CBP NCI device. This behavior is well explained using the BET channel to describe the energy loss in OPVs³⁻⁷. In the case of a 4CzIPN:CBP or 4CzTPN:CBP film, the $^3\text{CT}_1$ can survive with a long lifetime because of the shut-off of the Dexter energy transfer channel to the host. In addition, a decrease in the LLE intensity was observed in response to the application of an external negative voltage pulse, indicating the dissociation of the excitons of 4CzIPN and the suppression of charge-carrier recombination (**Figure 3-19**). Thus, no formation of the host $^3\text{CT}_1$ state is responsible for the no energy-loss channel in the triplet's preserved host environment.

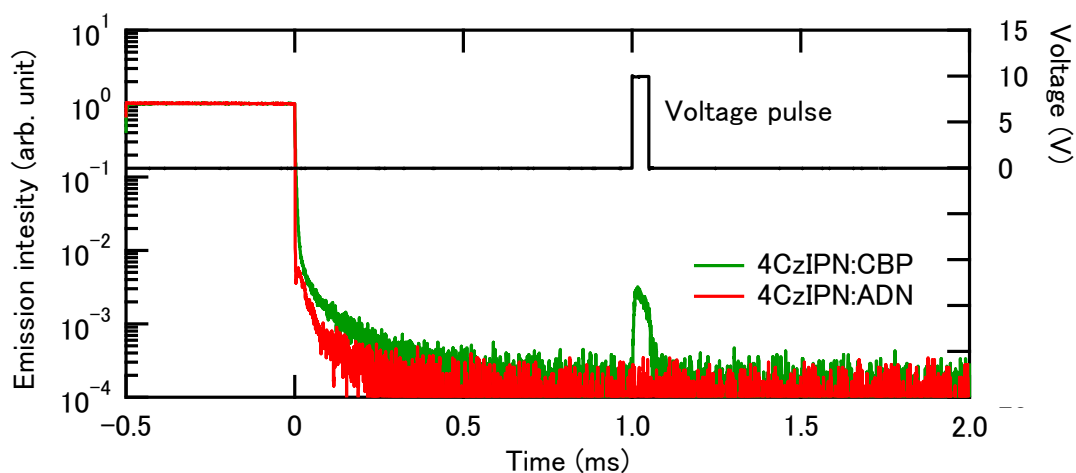


Figure 3-18. External-electric-field-modulated TRPL profile in 4CzIPN-based NCI devices with triplet-activated and -deactivated host. The device structure is ITO (100 nm) / SiO₂ (100 nm) / 50-wt%-4CzIPN:CBP or 50-wt%-4CzIPN:ADN (100 nm) / CBP (100 nm) / Al (100 nm). The applied peak voltage and the width were fixed at 10 V and 50 μs , respectively.

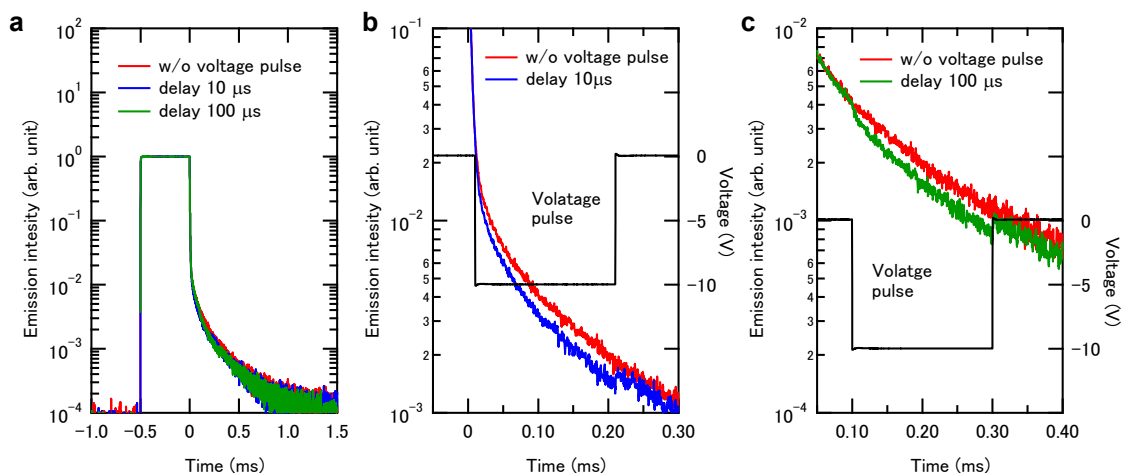


Figure 3-19. External-electric-field-modulated TRPL profiles in a 50-wt%-4CzIPN:CBP NCI device. The applied peak voltage and the width were fixed at -10 V and 200 μ s, respectively.

3-3. Summary

We investigated the role of the $^3\text{CT}_1$ states in organic molecular systems with a small ΔE_{ST} for exciton dissociation events. Our observations highlight that the charge separation following the exciton dissociation from the $^3\text{CT}_1$ states rather than the $^1\text{CT}_1$ states is inherently critical because the fast decay channels (e.g., the fluorescence decay channel in $^1\text{CT}_1$ states) are shut off and the $^3\text{CT}_1$ states are spin-forbidden. We expect that our fundamental findings will contribute to the future molecular design of efficient photoelectron conversion via the engineering of the excited spin states. For example, CT excitons exhibiting $k_{\text{r}} < k_{\text{ISC}}$ are advantageous for generating long-lived charge carriers and successive exciton dissociation for a high photoelectron conversion efficiency. The molecular structure of 4CzIPN (or 4CzTPN) used in the present study is, unfortunately, unfavorable for charge separation between neighboring molecules because of its four bulky carbazole units, which shield the electron-acceptor unit, and because the $^3\text{CT}_1$ state has a short lifetime as a consequence of the nature of the rapid reverse intersystem

crossing²⁸. Therefore, for practical applications, the simple D-A-type organic molecular systems that exhibit highly efficient TADF with a long ³CT₁ lifetime to provide an efficient carrier separation path, such as p-2Cz2BMe (³CT₁ lifetime: millisecond order)²⁹, would become the candidates. Also, we would like to understand the remaining issue for the charge separation processes in D-A intra- and intermolecular CT systems. Other researchers have argued that many intermolecular CT systems show charge separation from their singlet and higher excited states^{4, 15, 27}. Systematic studies involving tuning the strength of CT interaction would clarify the charge separation mechanism conclusively.

3-4. Sample preparation and experimental methods

3-4-1. Materials

4'-bis(carbazol-9-yl) biphenyl (CBP) and 2,4,6-tris(biphenyl-3-yl)-1,3,5- triazine (T2T) were purchased from NARD Institute. 4,4'-bis(N-(1-naphthyl)-N-phenylamino)-biphenyl (α -NPD) and tris-(8-hydroxyquinoline) aluminum (Alq₃) were purchased from Nippon Steel Chemical Co. ADN was purchased from Luminescence Technology Corp. 4CzIPN and 1,2,4,5-tetrakis(carbazol-9-yl)-3,6-dicyanobenzene (4CzTPN) were synthesized via previously reported methods².

3-4-2. Sample fabrication

All organic layers were formed by thermal evaporation under high-vacuum conditions ($<10^{-4}$ Pa). Organic films with a thickness of 50 nm were grown on precleaned quartz substrates. All of the devices were fabricated on clean ITO glass substrates and had an effective device area of 4 mm². The device structure for the DCM, IQE, and fluorescence lifetime measurements under an electric field was ITO (100 nm)/ α -NPD (50

nm)/ EML (50 nm)/Al (100 nm), with ITO as the anode, α -NPD as the hole transport layer, and Al as the cathode. The device structure for the external electric field–modulated PL measurements (NCI-type device) was ITO (100 nm)/T2T (30 nm)/EML (100 nm)/CBP (30 nm)/Al (100 nm), with ITO as the anode, T2T as the hole-blocking layer, CBP as the electron-blocking layer, and Al as the cathode. Each emissive layer consisted of a host matrix (CBP or ADN) and a TADF fluorophore (4CzIPN or 4CzTPN), respectively. After device fabrication, the devices were immediately encapsulated with glass lids and epoxy glue in a dry N₂-filled glove box.

3-4-3. Measurement of fundamental PL properties

The PLQY and the time constant for TADF molecules were measured using an absolute PLQY measurement system (C11347-01, Hamamatsu Photonics) and a fluorescence lifetime spectrometer (C11367, Hamamatsu Photonics) with a time-correlated single-photon counting (TCSPC) method, respectively.

3-4-4. TRPL measurement and PL intensity measurement under electric fields

TRPL decay was measured using a photosensor module (H10721-01, Hamamatsu Photonics), an amplifier unit (C11184, Hamamatsu Photonics), and an oscilloscope (WaveRunner 640Zi, Teledyne Lecroy) with a function generator (WaveStation2012, Teledyne Lecroy) as an external electric field source for observing the LLE and external electric field–modulated TRPL profile. A pulsed LED driving circuit was prepared as an excitation source, and a long-pass filter with an optical density of 5 was used for extraction of the sample signal. The power density of the excitation LED was fixed at 20

mW cm⁻². All TRPL signals were averaged for 10,000 measurements, smoothed using the moving-average method, and normalized at the intensity immediately before the photoexcitation was turned off.

3-4-5. Fluorescence lifetime measurements under an electric field

The fluorescence lifetime of the samples under an electric field was measured using a photosensor module (H10721-01, Hamamatsu Photonics), an amplifying unit (VT120A, Ortec), a time-to-digital converter (U1050A-002, Agilent), a discriminator (model 584, Ortec), and an excitation light source (LDH-D-C-420, PicoQuant) via the TCSPC method. A DC power supply was used as an external electric field source.

3-4-6. DCM characterization

DCM was conducted using a current-input preamplifier (LI-76, NF Corporation) and a multifunction filter (3611, NF Corp.) with an oscilloscope and a function generator. All DCM curves were measured with a sweep rate of 100 V s⁻¹ at room temperature.

3-4-7. IQE measurements

The IQE was calculated as the ratio of the absorbed photons to the observed current. The irradiation power (a tungsten lamp with a monochromator) was measured using a calibrated photodiode (S1337-1010BQ, Hamamatsu Photonics) covered by a light shield with a 4 mm² hole, which was the same area as the active area of the device. The number of absorbed photons was estimated from the absorbance of codeposited films with consideration of the reflection interference and optical length in the device. The photocurrent was measured using a pA Meter DC Voltage Source (4140B, Agilent).

References

1. M. A. Baldo, D. F. O'Brien, Y. You, A. Shoustikov, S. Sibley, M. E. Thompson and S. R. Forrest, Highly efficient phosphorescent emission from organic electroluminescent devices. *Nature* **395**, 151-154 (1998).
2. H. Uoyama, K. Goushi, K. Shizu, H. Nomura and C. Adachi, Highly efficient organic light-emitting diodes from delayed fluorescence. *Nature* **492**, 234-238 (2012).
3. T. M. Clarke and J. R. Durrant, Charge Photogeneration in Organic Solar Cells. *Chem. Rev.* **110**, 6736-6767 (2010).
4. A. Rao, P. C. Y. Chow, S. Gélinas, C. W. Schlenker, C.-Z. Li, H.-L. Yip, A. K. Y. Jen, D. S. Ginger and R. H. Friend, The role of spin in the kinetic control of recombination in organic photovoltaics. *Nature* **500**, 435-439 (2013).
5. Y. Hou, X. Zhang, K. Chen, D. Liu, Z. Wang, Q. Liu, J. Zhao and A. Barbon, Charge separation, charge recombination, long-lived charge transfer state formation and intersystem crossing in organic electron donor/acceptor dyads. *J. Mater. Chem. C* **7**, 12048-12074 (2019).
6. S. Gélinas, O. Paré-Labrosse, C.-N. Brosseau, S. Albert-Seifried, C. R. McNeill, K. R. Kirov, I. A. Howard, R. Leonelli, R. H. Friend and C. Silva, The Binding Energy of Charge-Transfer Excitons Localized at Polymeric Semiconductor Heterojunctions. *J. Phys. Chem. C* **115**, 7114-7119 (2011).
7. H. Kraus, M. C. Heiber, S. Vath, J. Kern, C. Deibel, A. Sperlich and V. Dyakonov, Analysis of Triplet Exciton Loss Pathways in PTB7:PC71BM Bulk Heterojunction Solar Cells. *Sci. Rep.* **6**, 29158 (2016).
8. S. H. Park, A. Roy, S. Beaupré, S. Cho, N. Coates, J. S. Moon, D. Moses, M. Leclerc, K. Lee and A. J. Heeger, Bulk heterojunction solar cells with internal quantum efficiency approaching 100%. *Nat. Photonics* **3**, 297-302 (2009).
9. H. Yin, S. Chen, S. H. Cheung, H. W. Li, Y. Xie, S. W. Tsang, X. Zhu and S. K. So, Porphyrin-based thick-film bulk-heterojunction solar cells for indoor light harvesting. *J. Mater. Chem. C* **6**, 9111-9118 (2018).
10. D. Baran, N. Gasparini, A. Wadsworth, C. H. Tan, N. Wehbe, X. Song, Z. Hamid, W. Zhang, M. Neophytou, T. Kirchartz, C. J. Brabec, J. R. Durrant and I. McCulloch, Robust nonfullerene solar cells approaching unity external quantum efficiency enabled by suppression of geminate recombination. *Nat. Commun.* **9**, 2059 (2018).

11. P. C. Chow, S. Gelinas, A. Rao and R. H. Friend, Quantitative bimolecular recombination in organic photovoltaics through triplet exciton formation. *J. Am. Chem. Soc.* **136**, 3424-3429 (2014).
12. J. Benduhn, F. Piersimoni, G. Londi, A. Kirch, J. Widmer, C. Koerner, D. Beljonne, D. Neher, D. Spoltore and K. Vandewal, Impact of Triplet Excited States on the Open-Circuit Voltage of Organic Solar Cells. *Adv. Energy Mater.* **8**, 1800451 (2018).
13. T. Higashino, T. Yamada, M. Yamamoto, A. Furube, N. V. Tkachenko, T. Miura, Y. Kobori, R. Jono, K. Yamashita and H. Imahori, Remarkable Dependence of the Final Charge Separation Efficiency on the Donor-Acceptor Interaction in Photoinduced Electron Transfer. *Angew. Chem. Int. Ed.* **55**, 629-633 (2016).
14. M. R. Narayan and J. Singh, Roles of binding energy and diffusion length of singlet and triplet excitons in organic heterojunction solar cells. *physica status solidi (c)* **9**, 2386-2389 (2012).
15. A. Classen, C. L. Chochos, L. Lürer, V. G. Gregoriou, J. Wortmann, A. Osvet, K. Forberich, I. McCulloch, T. Heumüller and C. J. Brabec, The role of exciton lifetime for charge generation in organic solar cells at negligible energy-level offsets. *Nat. Energy* **5**, 711-719 (2020).
16. T. Yamanaka, H. Nakanotani and C. Adachi, Slow recombination of spontaneously dissociated organic fluorophore excitons. *Nat. Commun.* **10**, 5748 (2019).
17. Y. Noguchi, W. Brütting and H. Ishii, Spontaneous orientation polarization in organic light-emitting diodes. *Jpn. J. Appl. Phys.* **58**, SF0801 (2019).
18. R. Kabe and C. Adachi, Organic long persistent luminescence. *Nature* **550**, 384-387 (2017).
19. Z. Zhou, C. Qiao, K. Wang, L. Wang, J. Liang, Q. Peng, Z. Wei, H. Dong, C. Zhang, Z. Shuai, Y. Yan and Y. S. Zhao, Experimentally Observed Reverse Intersystem Crossing-Boosted Lasing. *Angew. Chem. Int. Ed.* **59**, 21677-21682 (2020).
20. Y. Zhang and S. R. Forrest, Existence of continuous-wave threshold for organic semiconductor lasers. *Phys. Rev. B* **84**, 241301 (2011).
21. S. Egusa, N. Gemma, A. Miura, K. Mizushima and M. Azuma, Carrier injection characteristics of the metal/organic junctions of organic thin-film devices. *J. Appl. Phys.* **71**, 2042-2044 (1992).
22. D. L. Dexter, A Theory of Sensitized Luminescence in Solids. *J. Chem. Phys.* **21**, 836-850 (1953).

23. L. Jäger, T. D. Schmidt and W. Brütting, Manipulation and control of the interfacial polarization in organic light-emitting diodes by dipolar doping. *AIP Adv.* **6**, 095220 (2016).
24. M. Tanaka, H. Noda, H. Nakanotani and C. Adachi, Molecular orientation of disk-shaped small molecules exhibiting thermally activated delayed fluorescence in host–guest films. *Appl. Phys. Lett.* **116**, 023302 (2020).
25. H. S. Kim, S.-R. Park and M. C. Suh, Concentration Quenching Behavior of Thermally Activated Delayed Fluorescence in a Solid Film. *J. Phys. Chem. C* **121**, 13986-13997 (2017).
26. J. Lee, N. Aizawa, M. Numata, C. Adachi and T. Yasuda, Versatile Molecular Functionalization for Inhibiting Concentration Quenching of Thermally Activated Delayed Fluorescence. *Adv. Mater.* **29**, 1604856 (2017).
27. A. E. Jailaubekov, A. P. Willard, J. R. Tritsch, W. L. Chan, N. Sai, R. Gearba, L. G. Kaake, K. J. Williams, K. Leung, P. J. Rossky and X. Y. Zhu, Hot charge-transfer excitons set the time limit for charge separation at donor/acceptor interfaces in organic photovoltaics. *Nat. Mater.* **12**, 66-73 (2013).
28. H. Noda, X. K. Chen, H. Nakanotani, T. Hosokai, M. Miyajima, N. Notsuka, Y. Kashima, J. L. Bredas and C. Adachi, Critical role of intermediate electronic states for spin-flip processes in charge-transfer-type organic molecules with multiple donors and acceptors. *Nat. Mater.* **18**, 1084-1090 (2019).
29. H. Noda, H. Nakanotani and C. Adachi, Highly Efficient Thermally Activated Delayed Fluorescence with Slow Reverse Intersystem Crossing. *Chemistry Letters* **48**, 126-129 (2019).

Chapter 4

Electron lifetime of over one month in disordered organic solid-state films

Takahiko Yamanaka, Hajime Nakanotani, Katsuhiko Nakamoto & Chihaya
Adachi
(Submitted)

Abstract

Understanding intrinsic carrier lifetime in disordered organic solid-state semiconductors is essential for improving device performance in not only molecule-based optoelectronic devices such as OPV but also photocatalysts used for producing solar fuel cells. Carriers in disordered films are generally thought to have short lifetimes on a scale ranging from nanoseconds to milliseconds¹. These short carrier lifetimes cause loss of charges in OPVs and low quantum yields in photocatalysts and impede the future application of organic semiconductors to, for example, charge-storage-based memory devices. This study reports an ultra-long intrinsic carrier lifetime of more than one month in a disordered film of an organic semiconductor stored at room temperature without external power. This extraordinary lifetime, which is several orders of magnitude longer than that generally believed possible in conventional organic semiconductors, arises from carrier stabilization by SOP, excited spin-triplet recycling, and blocking of recombination processes in disordered films.

4-1. Introduction

For organic semiconductors, an exciton dissociation event in a solid-state is recognized as one of the critical processes. In OPVs, exciton dissociation and carrier collection in organic solid-state semiconductor films greatly influence the power conversion efficiency²⁻⁴. Carriers generated and separated via exciton dissociation at the interface between D and A molecules are transported in the D and A layers and then collected by electrodes. Thus, short carrier lifetimes limit the spatial and temporal lengths of carrier diffusion and transportation, thereby limiting carrier collection in OPVs. Aside from increasing efficiency in OPVs, long carrier lifetimes in organic solid-state semiconductors can facilitate efficient photocatalytic reactions such as hydrogen production⁵. In OLEDs, on the other hand, exciton dissociation can reduce a fluorophore's PLQY in organic solids^{6, 7} and negatively impact OLED performance. Furthermore, carriers generated by exciton dissociation lead to undesirable exciton-polaron interactions that reduce EL efficiency in OLEDs^{8, 9}. Therefore, a short carrier lifetime is preferable for efficient light production followed by immediate recombination of carriers.

Although the carrier generation following exciton dissociation events in a solid film seems to be an unwarranted process for OLEDs, it has been disclosed that the exciton dissociation can induce unique emission phenomena. For instance, OLPL^{10, 11} produces a long-lasting emission of over an hour when carriers generated by exciton dissociation at D/A interfaces slowly recombine, suggesting an unusually long carrier lifetime. Consequently, several open questions remain regarding exciton dissociation in organic solid-state systems: the role of the excited spin state in dissociation, the maximum length of carrier lifetime and the actual spatial extent of carrier diffusion. Recently, we showed that molecules exhibiting TADF have advantages for achieving efficient charge

separation¹². Since the energy levels of the S_1 and T_1 states of TADF molecules are nearly identical ($\Delta E_{ST} < 0.2$ eV), the T_1 state can act as an intermediate for exciton dissociation. The longer excited-state lifetimes of T_1 states compared to S_1 states and the possibility for exciton dissociation from the T_1 state provide more chances for dissociation of excitons into charges, thereby suppressing energy loss in OPVs. Since the triplet exciton generated by carrier recombination can re-dissociate to the charge carrier, the carriers generated from triplet-active organic solid-state films can exist relatively stably.

Previously, relatively long carrier lifetimes in organic solid-state films have been reported by several groups. For example, centimeter-scale electron diffusion—which corresponds to a long carrier lifetime of nearly three seconds even at room temperature—has been demonstrated in a fullerene-based photo-active organic heterostructure by eliminating carrier recombination centers¹³. Very recently, the generation of charges with lifetimes on the order of seconds in polymer-based organic semiconductor heterojunction nanoparticles has been also reported⁵, and W. Tian et al. reported that charge carriers generated in an *N,N'*-bis(naphthalene-1-yl)-*N,N'*-bis(phenyl)-benzidine (NPB) film by laser irradiation survived over five hours^{14, 15}. In these reported organic molecular systems, the spatial overlap between holes and electrons has been well suppressed, leading to the long lifetime of accumulated carriers. Alternatively, the introduction of deep electron trap sites enables long-duration carrier storage in D-A blend type OLPL systems, leading to photostimulated luminescence lasting over seven days¹⁶. However, since the luminescence intensity decays very rapidly, the carrier lifetime can be estimated to be considerably shorter than seven days. Thus, clarifying the limits of intrinsic charge carrier lifetime along with the spatial extent of carrier diffusion in organic solid-state films is crucial for improving our fundamental understanding of organic semiconductor physics

and could lead to future applications such as advanced imaging devices.

Here, we report an unexpectedly ultra-long carrier lifetime at room temperature of over one month for electrons, which is drastically longer than conventionally thought to be realistic. We also unveil that the carriers barely diffuse in the plane of the film, enabling us to use the ultra-long-lived carriers to reproduce images as EL. We achieved this by fabricating an electron storage device consisting of the organic molecule TPA-DCPP¹⁷ and an electron blocking layer (EBL) of T2T. In this molecular system, the TADF properties of TPA-DCPP allow triplets generated via hole-electron recombination to be dissociated again into charges, leading to a long carrier lifetime¹². Furthermore, spontaneous dissociation of TPA-DCPP excitons is assisted by the molecule's large permanent dipole moment (13.05 D)⁶. After exciton dissociation, generated holes were extracted from an anode by applying a short-duration bias voltage, and electrons were stored inside the device without the need for a constant external electrical field. We evaluated the electron lifetime by electrically injecting holes into the device at arbitrary timings to release the stored electrons as EL. This method can visualize the charge carrier stored in the device sensitively than that of electrical measurement.

4-2. Result and discussion

4-2-1. Characterization of charge carrier lifetime

Figure 4-1a shows the device structure and the energy levels of molecules in this study. The co-deposited film of TPA-DCPP as a guest and 3,3-di(9H-carbazol-9-yl)biphenyl (mCBP) as a host matrix was used as an emissive layer (EML). The 80-nm-thick T2T layer acts as an electron blocking layer, preventing leakage of electrons from the EML to the aluminum (Al) cathode. In this device, an EL response typical to that of

an OLED was not observed even when applying a forward DC voltage of 10 V because the large electron injection barrier at the T2T / Al interface prevents electrons from being injected from the Al cathode into the device (**Figure 4-2**). Therefore, in the non-electron-injecting (NEI) device, the lifetimes of electrons stored in the EML could be investigated by detecting the EL generated via the recombination of stored electrons with holes injected from the anode.

Figure 4-1b,c shows pulsed-EL measurement at different hold times after light irradiation, which generated the initial charges. For light irradiation, 470-nm monochromatic light was used because it is well-matched with the absorption band of TPA-DCPP. In this experiment, the power density and pulse width of the excitation light were fixed at 40 mW cm^{-2} and 50 microseconds, respectively. An offset voltage (-2 V) was applied during the light irradiation to facilitate both charge separation and hole extraction. After irradiation, the device was kept in open-circuit conditions. A turn-on voltage pulse (10 V) was then applied for 10 microseconds following a given hold time.

Pulsed EL was only observed after irradiation with light, implying that the produced EL provides a visual indication of the recombination of charge carriers stored in the EML. As depicted in **Figure 4-1d**, the EL intensity was constant for hold times from 0.1 to 10,000 seconds (~ 2.7 hours) and gradually attenuated for longer times. Notably, the EL intensity after ten days was still 80% of that for hold times of several seconds. Fitting the graph with the exponential decay equation $f(t) = e^{-t/\tau}$, where t is time, and τ is the lifetime, the electron lifetime was calculated to be 903 hours, i.e., electrons can survive over one month in the solid-state film. This result indicates that the electrons stored in the device are remarkably stable even at room temperature.

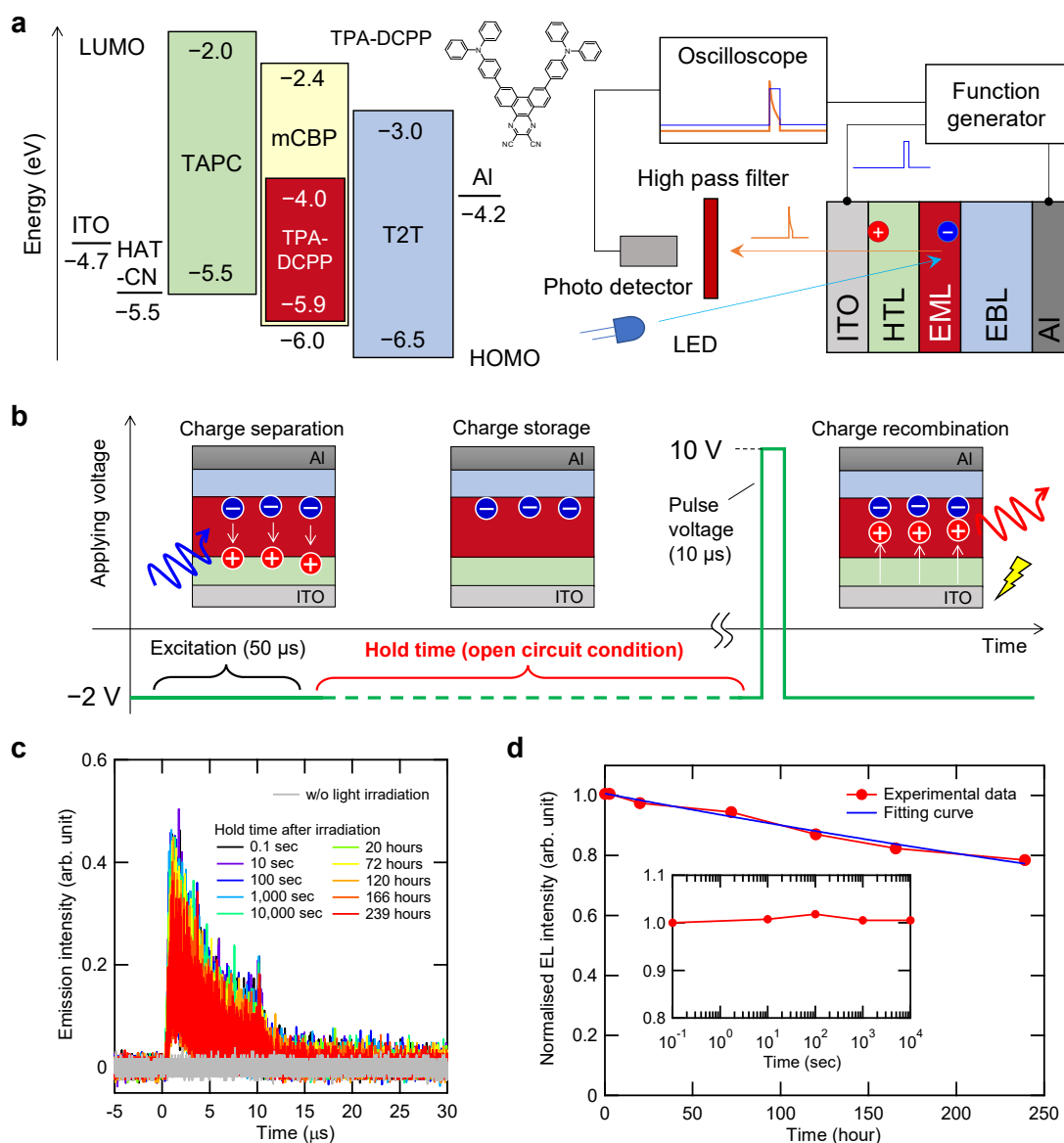


Figure 4-1. Device structure and EL decay for charge storage characterization. **(a)** Device structure, energy level diagram of molecules used in this study, and schematic illustration of the experimental setup for characterizing electron storage. **(b)** Timing chart of pulsed-EL measurement. The offset voltage during irradiation, turn-on voltage, and pulse width was fixed at -2 V, 10V, and 10 microseconds, respectively. During electron storage, the device was kept in open circuit conditions. **(c)** Pulsed-EL responses for arbitrary hold times after light irradiation. **(d)** Dependence of the EL intensity on the hold time after light irradiation. The EL intensity was defined as an integration of the EL response in **Figure 4-1c** from 0 to 16 microseconds. The dashed line corresponds to an exponential fitting ($f(t)=e^{-t/\tau}$) for the EL intensity against hold time, yielding a τ of 903 h. The inset is an enlarged view of the initial decay.

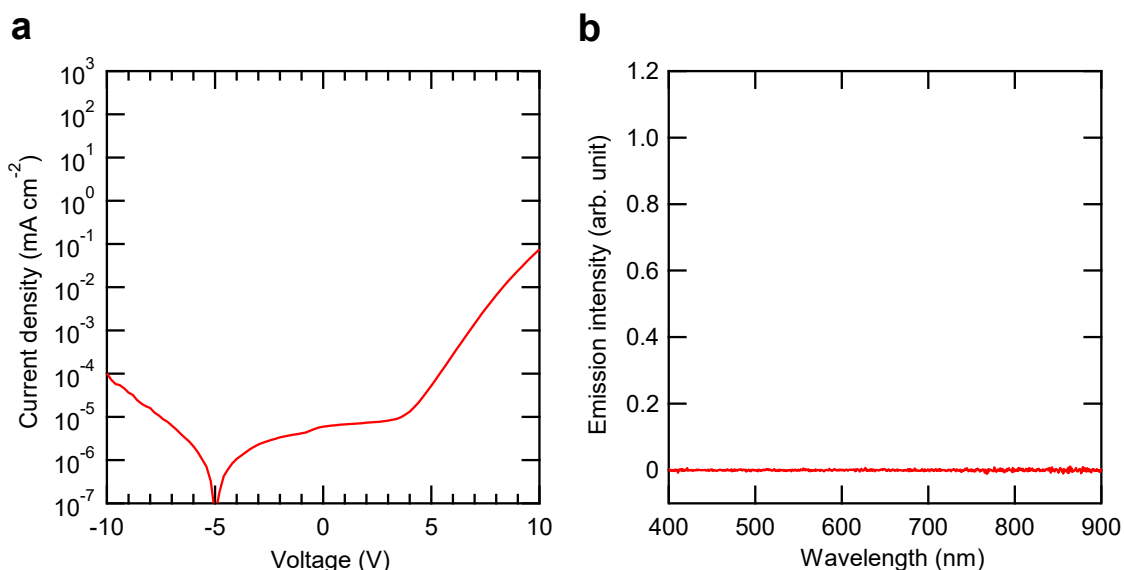


Figure 4-2. (a) Current density-voltage curve and (b) EL spectrum at 10 V for the non-electron-injecting type device.

Excessive charge generation was found to deteriorate the storage capability. **Figure 4-3** illustrates the charge storage characteristics after irradiation long enough (three seconds) to reach a steady state of carrier generation. In this case, the EL intensity rapidly decreased for hold times under 10 hours, implying that the larger number of carriers generated by long-duration irradiation accelerates recombination. Here, electrons were not entirely consumed in the case of a low turn-on voltage less than 10 V. As presented in **Figure 4-4**, EL was still detected even after applying a 3 V pulse multiple times, and an intense EL pulse was observed by applying a turn-on voltage of 10 V after a 3 V pulse. Additionally, the electron storage behavior was the same regardless of whether the device was under open-circuit conditions or an applied offset voltage of -2 V during the hold time (**Figure 4-5**). This indicates that the electrical potential slope in open-circuit conditions can be expected to be identical to that when applying -2 V, suggesting that the internal molecular polarization well stabilizes the accumulated electrons.

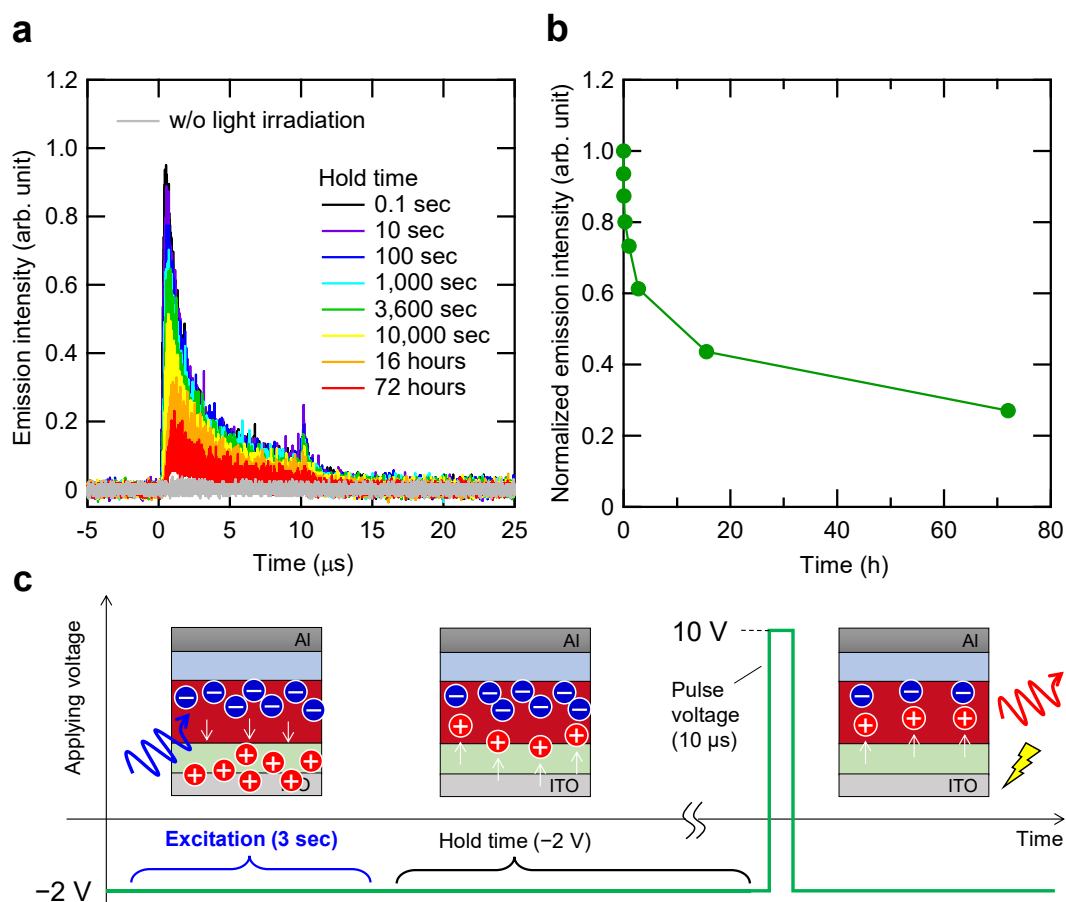


Figure 4-3. Charge storage characteristics when light irradiation was conducted for 3 seconds. **(a)** Pulsed EL of an NEI device for arbitrary hold times after light irradiation. **(b)** Time-dependent EL intensity based on the integration of the EL pulses in **Fig. 4-3a** from 0 to 16 microseconds. The inset displays the same data on log scales. **(c)** Timing chart of the pulsed-EL measurement. The offset voltage, turn-on voltage, and electrical pulse width were -2 V, 10 V, and 10 microseconds, respectively.

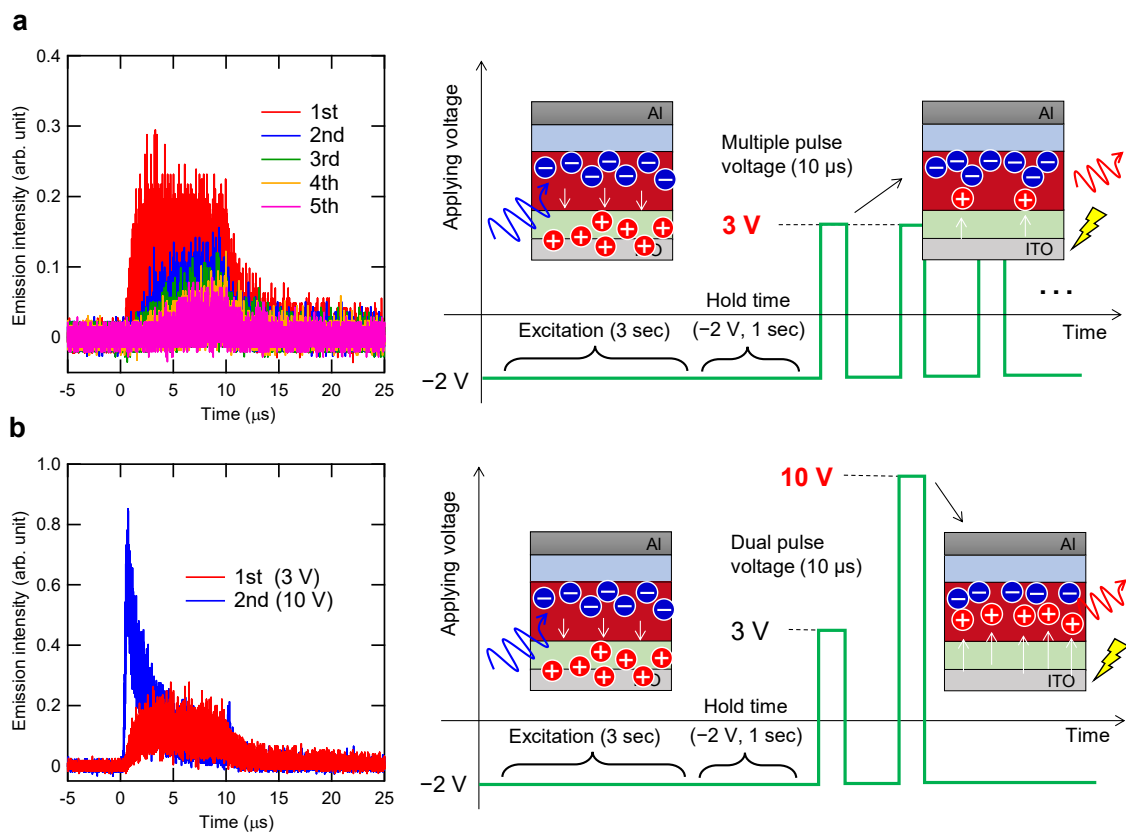


Figure 4-4. EL intensity when applying multiple pulse voltages. The offset voltage was fixed at -2 V. **(a)** Applying 3 V five times. **(b)** Applying 10 V after a 3 V pulse.

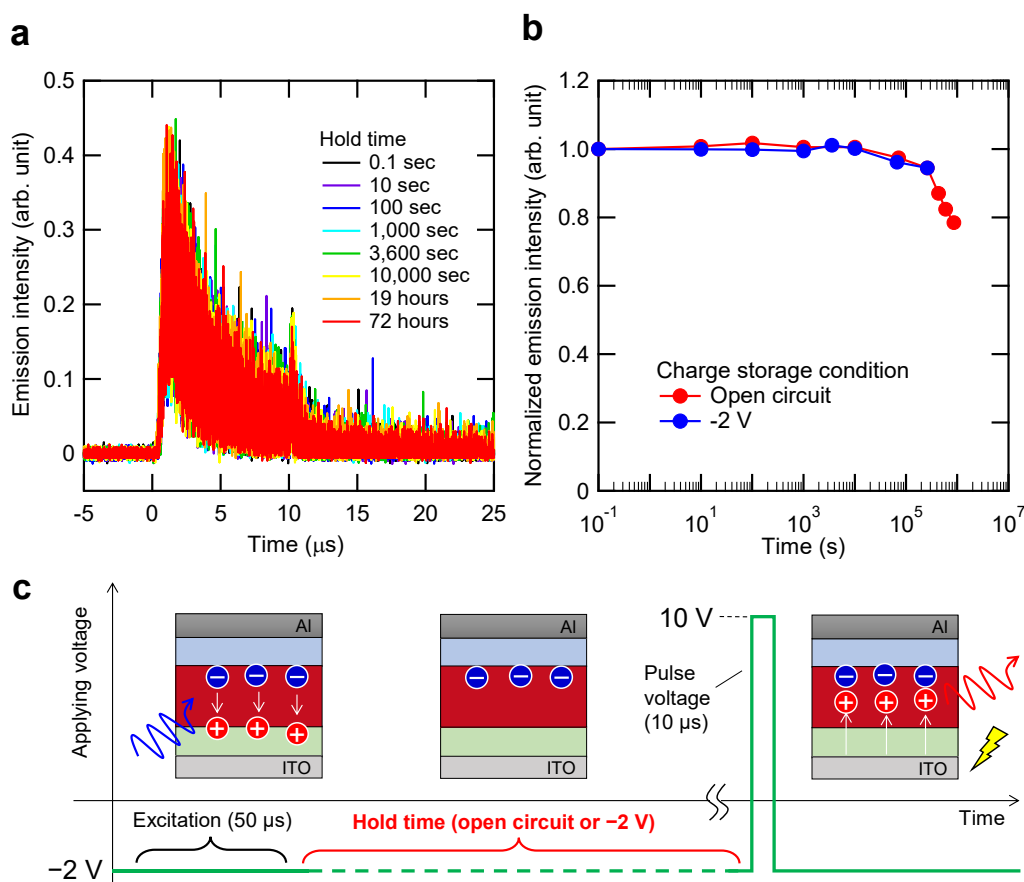


Figure 4-5. Charge storage characteristics when applying -2 V during the hold time. **(a)** Pulsed EL of an NEI device for arbitrary hold times after light irradiation. **(b)** Decay of EL intensity, which is defined as the integration of the EL pulse from 0 to 16 microseconds. **(c)** Timing chart of the pulsed-EL measurement. Light irradiation was conducted for 50 microseconds. An offset voltage of -2 V was applied during both the light irradiation and hold time. The turn-on voltage and electric pulse width were fixed at 10 V and 10 microseconds, respectively.

To explore the origin of the ultra-long-lived electrons based on charge dynamics such as injection and accumulation, displacement current measurement (DCM)^{18, 19} was conducted on a device with a standard OLED structure containing the same EML as the NEI device. The OLED structure was ITO/HAT-CN (10 nm)/TAPC (50 nm)/mCBP:50-wt%-TPA-DCPP (30 nm)/T2T (20 nm)/BPy-TP2 (60 nm)/Liq (2 nm)/Al. In this device, electrons can be injected from the Al cathode into the organic layers. In the steady-state

DCM profiles under dark conditions without irradiation as shown in **Figure 4-6a**, the displacement current observed when sweeping from -6 V to -2 V originated from the capacitance between both electrodes (ITO anode and Al cathode). The rising of the signal current at -2 V indicates the charge injection voltage (V_{inj}) at which the compensation for the spontaneous orientation polarization of the polar EML begins. The device subsequently exhibits significant current injection above the threshold voltage (V_{th}) of 2 V. Here, the injected current just after V_{inj} is assigned to holes because the capacitance corresponding to this region is independent of the thickness of the TAPC hole transport layer while it is dependent on that of the BPy-TP2 electron transport layer (**Figure 4-7**).

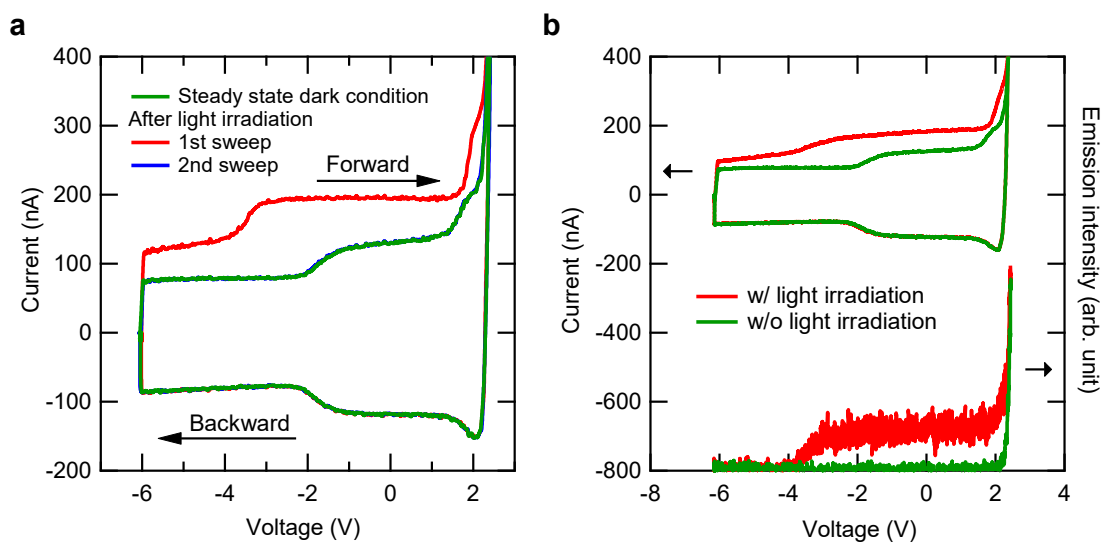


Figure 4-6. DCM characterization in an OLED based on TPA-DCPP. **(a)** 470 nm light irradiation was conducted for three seconds at -6 V before the first sweep (red line). The DCM curve in the second sweep (blue line) completely overlapped that of dark condition (green line), which was taken after five acquisitions in dark to assure a steady state. **(b)** Synchronized DCM and EL measurement. In the signals with light irradiation (red lines), excitation light with a pulse width of 500 microseconds was irradiated on the device under a -6 V bias before every single acquisition. The emission intensity was obtained by averaging 1,000 measurements.

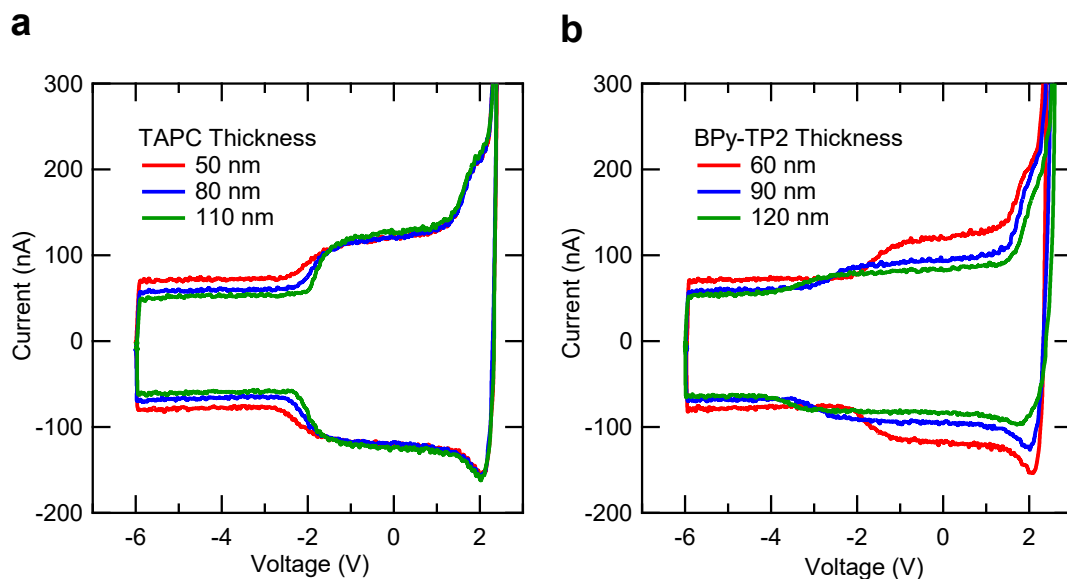


Figure 4-7. DCM profiles in the OLEDs with different thicknesses of charge transport layers. (a) Varying HTL (TAPC) thickness, (b) varying ETL (BPy-TP2) thickness.

Irradiating 470 nm light for three seconds on the device under a -6 V bias before scanning resulted in DCM profiles extremely different from those without prior irradiation. The displacement current around -6 V exceeds the amount of charge originating from the capacitance of the two electrodes without irradiation, indicating that excess charge carriers are injected into the device from the starting voltage of -6 V. This behavior can be attributed to the charge carriers generated by the dissociation of photo-generated TPA-DCPP excitons. During irradiation, the holes are extracted from the device under a negative bias voltage, whereas the electrons are trapped in the EML due to the presence of the large electron extraction barrier at the TPA-DCPP/T2T interface. DCM profiles of a bilayer device without the electron blocking layer exhibit no difference with light irradiation (**Figure 4-8**), which is consistent with T2T causing electron accumulation. These results provide further evidence that TPA-DCPP excitons spontaneously dissociate into free charge carriers—a process assisted by the SOP of the EML—and electrons

accumulate in the device.

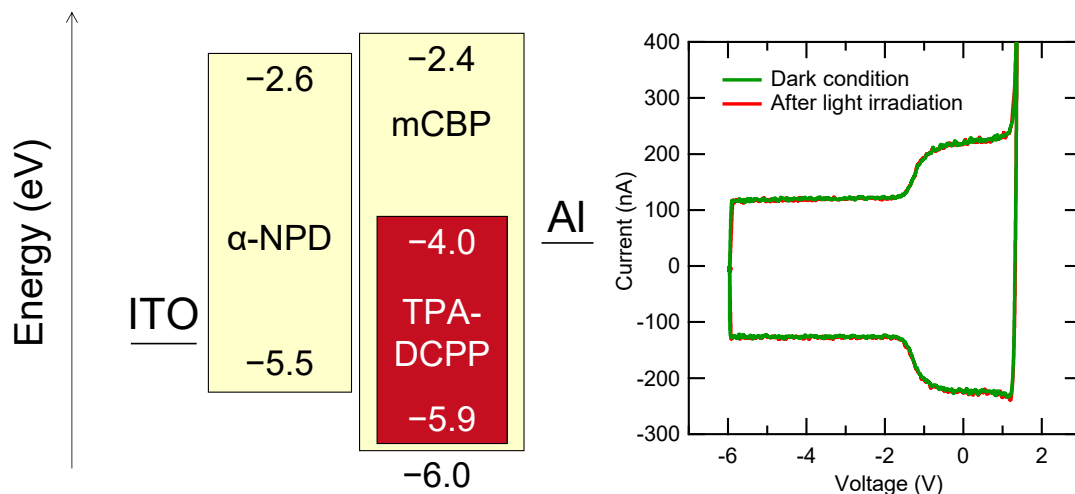


Figure 4-8. Energy levels of and DCM profiles in a bilayer device. The device structure is ITO/ α -NPD (50 nm)/mCBP:50 wt%-TPA-DCPP (50 nm)/Al.

The DCM signal was only larger for the forward sweep of the first scan. During the second sweep, the signal overlapped the steady-state DCM signal (i.e., dark conditions), which is expected if the accumulated electrons recombined with holes during the first scan. Recombination should produce EL originating from TPA-DCPP, even below V_{th} , so synchronized DCM and EL measurements were performed. As depicted in **Figure 4-6b**, EL response was indeed observed at voltages over -4 V in the acquisition scan after light irradiation. Conversely, no EL was observed at even 2 V in the scan without light irradiation. As expected, EL was observed only during the forward sweep, which is consistent with accumulated electrons being consumed by recombination with injected holes (**Figure 4-9**). Holes start to be injected into the EML at -4 V, with the currents of 125 nA and 200 nA in **Figure 4-6b** assigned to hole accumulation at the TAPC/EML and EML/T2T interfaces in dark condition, respectively, based on **Figure 4-7**. Here, the

accumulated electrons induced by light irradiation are calculated to be -9.5 nC (**Figure 4-10**). Therefore, the interface charge is estimated to be -2.4 mC m^{-2} , which corresponds to $\sim 3\%$ of TPA-DCPP molecules in the EML forming radical anion states if the charge carriers are assumed to be accumulated within one nanometer of the EML/T2T interface.

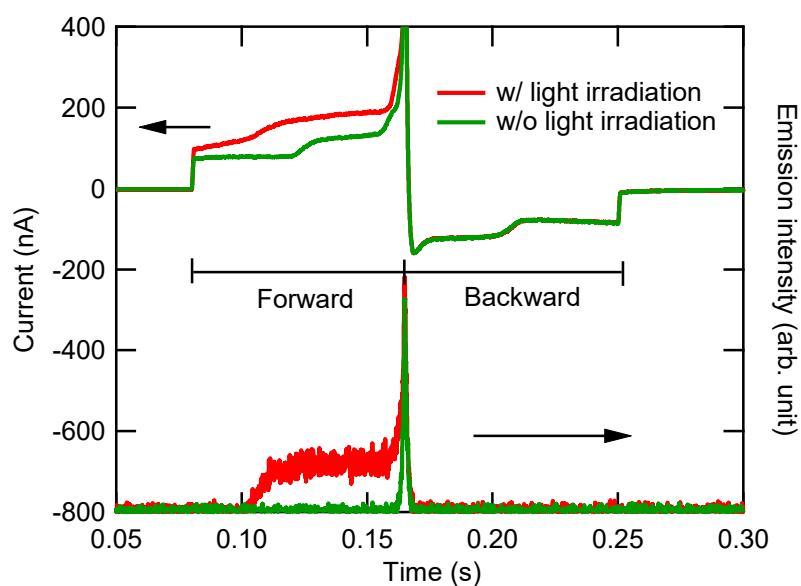


Figure 4-9. EL measurement synchronized with DCM. The horizontal axis is time. EL based on accumulated charges was only observed in the forward sweep just after light irradiation. Here, the EL peak observed at 0.16 seconds in both profiles is due to CW emission over threshold voltage (V_{th}) of 2 V.

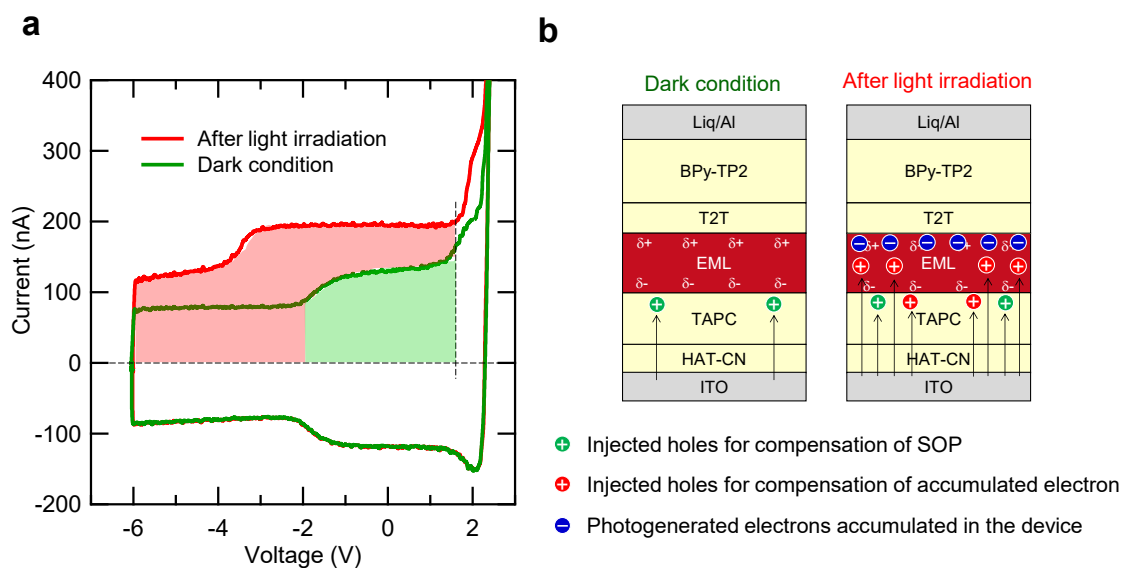


Figure 4-10. (a) DCM curves for the accumulated charge calculation. The areas filled with red and green colors originated from the accumulated charge and intrinsic molecular polarization, respectively. (b) Schematic illustrations of the charge carrier behavior on DCM. The accumulated electrons are estimated by subtracting the total injected holes induced by light irradiation from injected holes in the dark condition for compensation of SOP.

Based on the previous experimental results and discussion, we interpret the charge storage mechanism as illustrated in **Figure 4-11**. Initially, an internal potential slope induced by the SOP is formed before light irradiation. During irradiation under a negative bias, a number of charge carriers are optically generated by the exciton dissociation, and the holes are extracted through the ITO electrode. When the irradiation is stopped, the electronic equilibrium re-organizes, and some accumulated electrons are gradually consumed as they recombine with back-flowing holes. The remaining electrons are then stored stably near the EML/EBL interface with the help of the SOP. Notably, the spontaneous molecular orientation plays a fundamental role in determining the charge storage characteristics.

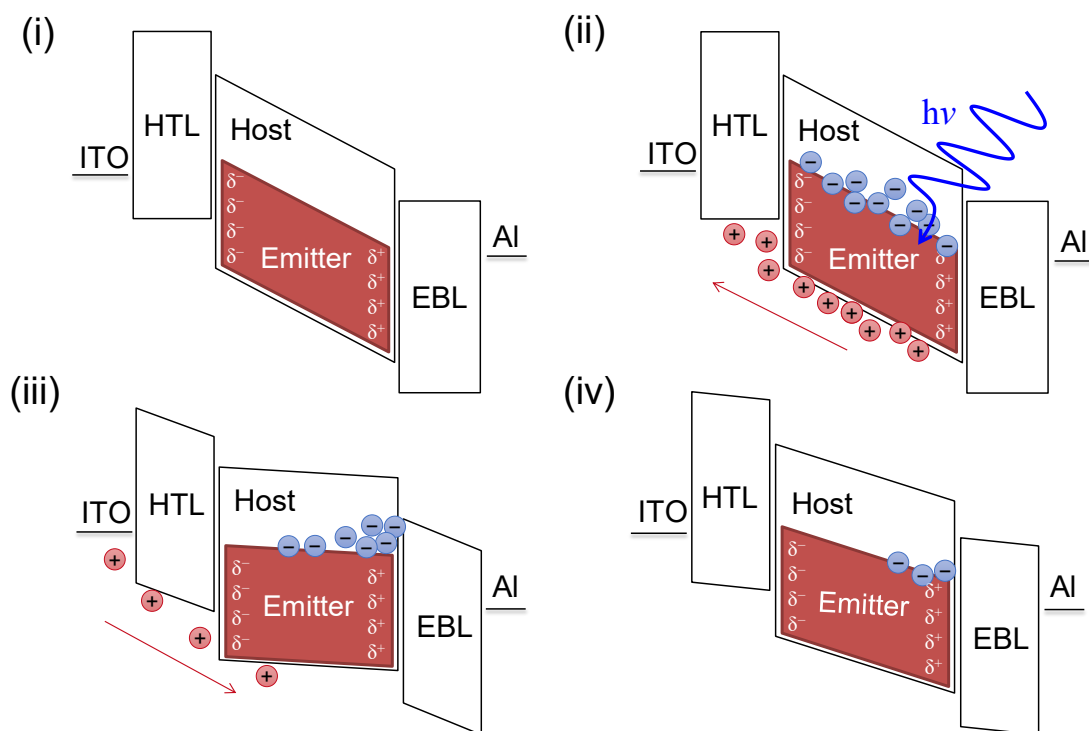


Figure 4-11. Schematic illustrations of the charge storage mechanism. (i) Steady state (before light irradiation). (ii) Charge separation under light irradiation with an offset voltage applied. (iii) Gradual consumption of charge carriers caused by the backflow of holes after turning off the offset voltage. (iv) Stable charge storage.

4-2-2. Evaluation of spatial storage ability

Having demonstrated the long lifetime of the electrons, we next characterized the device's spatial retention of electrons using a monochrome camera (the experimental setup is illustrated in **Figure 4-12**). The existence of long-lived electrons and the ability to read them as EL enabled us to visualize the electron diffusion behavior in the solid state. Light from an LED was passed through a line-and-space pattern (**Figure 4-13a**) and projected onto a device with an effective area of 10 mm diameter. For this experiment, light was irradiated for 20 milliseconds with a power density of 40 mW cm^{-2} to obtain a sufficient noise-to-signal ratio in the EL image. By applying turn-on voltage to the device one second after excitation light off, EL was only observed from areas that were irradiated

with light (**Figure 4-13a**) with little spreading or blurring. **Figure 4-13b** shows the distribution of the EL intensity across one of the line-and-space patterns. The EL pattern aligned well with the irradiated areas even after a hold time of 1,000 seconds, indicating that the accumulated electrons remained near the EML/T2T interface under the influence of the EML's SOP. Although the edge of the pattern slightly spread as time passed (**Figure 4-14**), the spatial information was still largely intact after 1,000 seconds.

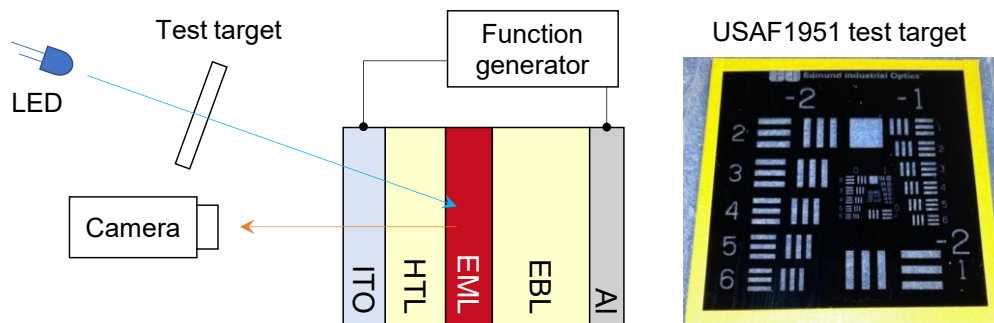


Figure 4-12. Schematic illustration of experimental set-up for EL imaging. The EL image was slightly stretched in the horizontal direction because the light irradiation was conducted at an angle that was not perfectly perpendicular to the device. The photograph is the projected pattern used in this measurement. An LED light passing through the test pattern was focused on the device with unity magnification.

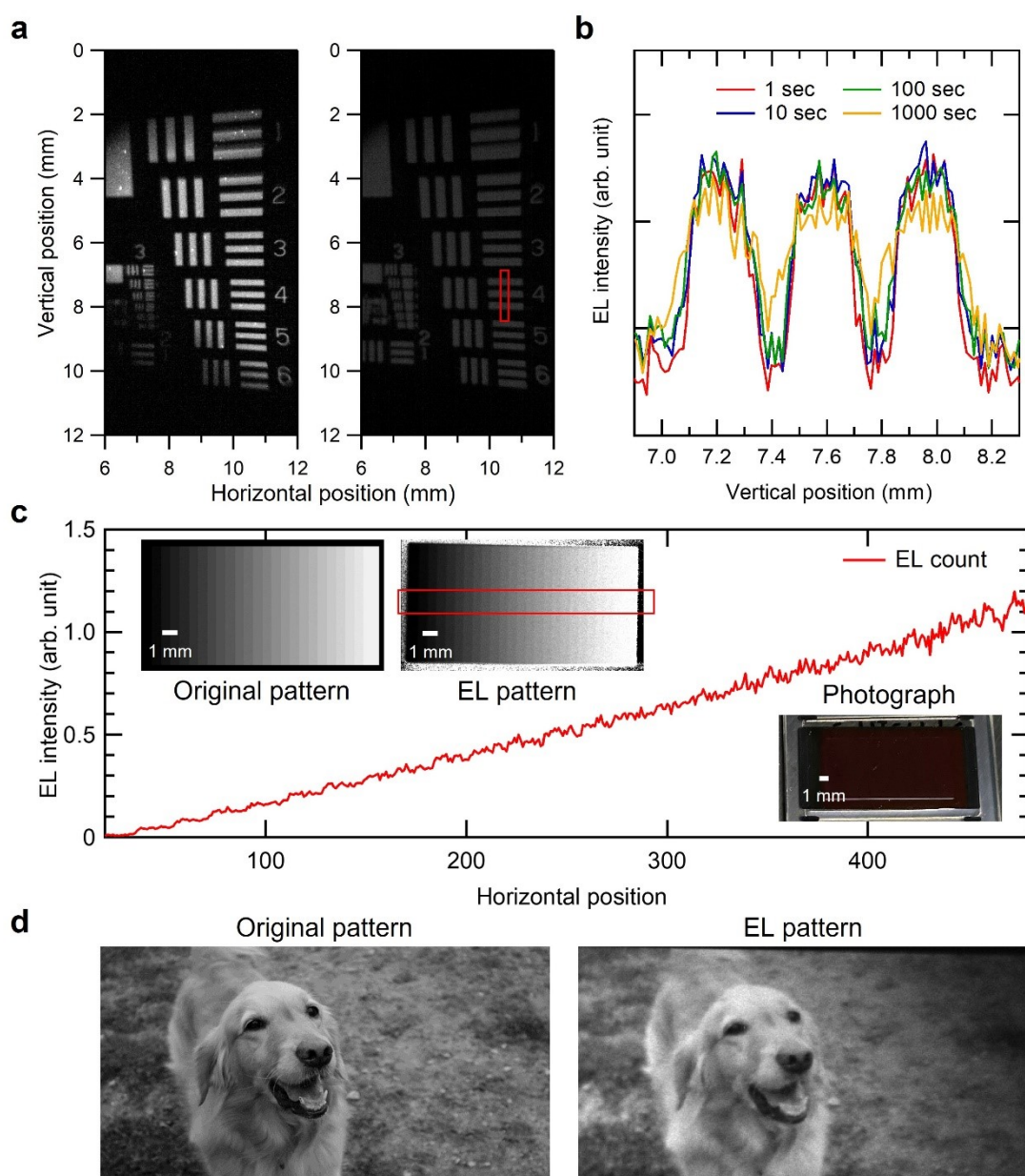


Figure 4-13. Electroluminescence imaging for evaluation of spatial electron storage ability. **(a)** The left image is the device during light irradiation and the right image is the device when applying a turn-on voltage after a hold time of one second. An offset voltage during the light irradiation and turn-on voltage are -2 V and 10 V, respectively. **(b)** Characterization of the EL pattern along the area corresponding to the red box in Fig. 3a for different hold times. The EL intensity is the average of five lines. **(c)** Original grayscale pattern reproduced EL pattern corrected for spatial inhomogeneity of light intensity image, and photograph of the device used to test grayscale behavior. The graph shows the EL intensity along with the red box in the EL pattern. **(d)** Original pattern and EL pattern reproduced by the device to demonstrate storage of a grayscale photograph.

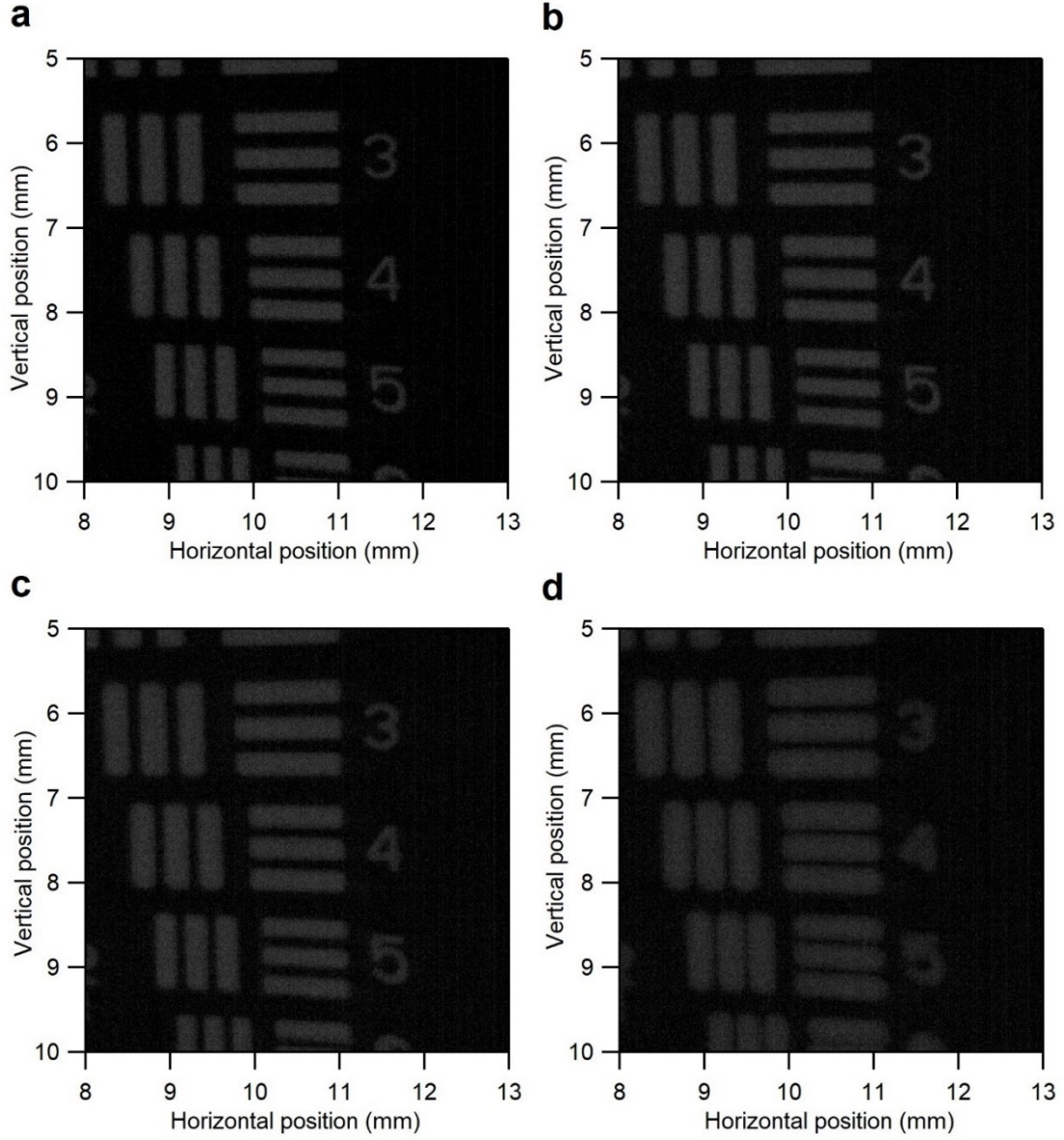


Figure 4-14. EL images after arbitrary hold times of (a) 1 second, (b) 10 seconds, (c) 100 seconds, and (d) 1,000 seconds.

In this device, the motion of charge carriers, i.e., electron current (j_n), can be expressed as the sum of drift and diffusion currents by

$$j_n = qn\mu_n E(x) + kT\mu_n \frac{dn}{dx}$$

where k is the Boltzmann constant, T is the temperature, μ_n is the electron mobility, n is the electron density, x is the position on a line in the plane of the device, q is the

elementary charge, and $E(x)$ is the electric field at x . In-plane polarization of TPA-DCPP is expected to be significantly smaller than the polarization in the direction of the permanent dipole moment, which is normal to the film, so the drift current that depends on the electric field can be neglected. In addition, diffusion current should be low because of the low electron mobility of TPA-DCPP²⁰, contributing to the good spatial retention of the stored charges.

To evaluate the linearity of the dependence of charge generation on excitation power, we conducted grayscale imaging using an electron-multiplying CCD camera (EM-CCD) and pattern projection using a digital micromirror device (DMD). The patterned light was generated by reflecting the excitation light off a 2D micromirror array in which each mirror can direct the light either onto or away from the NIE device. The irradiation intensity was controlled by adjusting the duty ratio, i.e., the period for which the mirror faced to the device. When using a grayscale chart graded into 25 levels as the irradiation pattern as presented in **Figure 4-13c**, gradation proportional to the irradiation intensity was clearly observed in the EL image corrected for the spatial inhomogeneity of light intensity. In this measurement, to correct for the spatial inhomogeneity of the excitation LED during EL imaging, we obtained a reference image (S_{ref}) and a dark image (S_{dark}). For the S_{ref} acquisition, the duty ratios of all pixels of the DMD were fixed at unity, i.e., the whole effective area was irradiated for ten milliseconds (**Figure 4-15a**). The S_{dark} acquisition corresponds to the image without applying a turn-on voltage to the device (**Figure 4-15b**). The corrected image (S_{cor}) was calculated as follows:

$$S_{\text{cor}} = \frac{(S_{\text{raw}} - S_{\text{dark}})}{(S_{\text{ref}} - S_{\text{dark}})}$$

where S_{raw} is a raw EL image (**Figure 4-15c**). The S_{dark} subtraction was performed to eliminate the signal originating from ambient light and an offset of the EM-CCD. The

S_{dark} acquisition shows no image (**Figure 4-15b**), indicating that no emission image can be observed under optical excitation with no voltage application (e.g., delayed fluorescence of the TADF emitter).

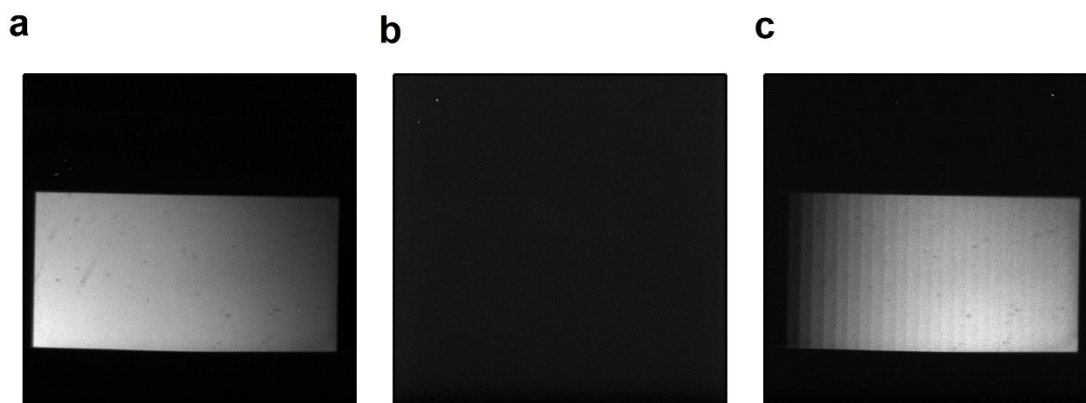


Figure 4-15. Gray scale EL imaging for correction of spatial inhomogeneity. (a) Reference image (S_{ref}). (b) Dark image (S_{dark}). (c) Raw EL image of the grayscale chart projection (S_{raw}).

We also evaluated the dependence of the EL intensity on the excitation pulse width and power density at a fixed position using a point sensor to evaluate the EL linearity by eliminating the spatial information (**Figure 4-16**). A linear relationship between EL intensity and the excitation pulse width was observed just as with the DMD projection (irradiation power density $\sim 3 \mu\text{W cm}^{-2}$), whereas poor linearity with power density was obtained. The EL intensity saturated for irradiation with a power density over 50 mW cm^{-2} and a pulse width of 500 microseconds since there is an upper limit for charge storage capacity (-2.4 mC m^{-2}) determined by the SOP of the organic polar film. Finally, we demonstrated the successful storage and retrieval of a complex pattern in high-resolution grayscale by imaging a photograph with an arbitrary distribution of intensities as illustrated in **Figure 4-13d**.

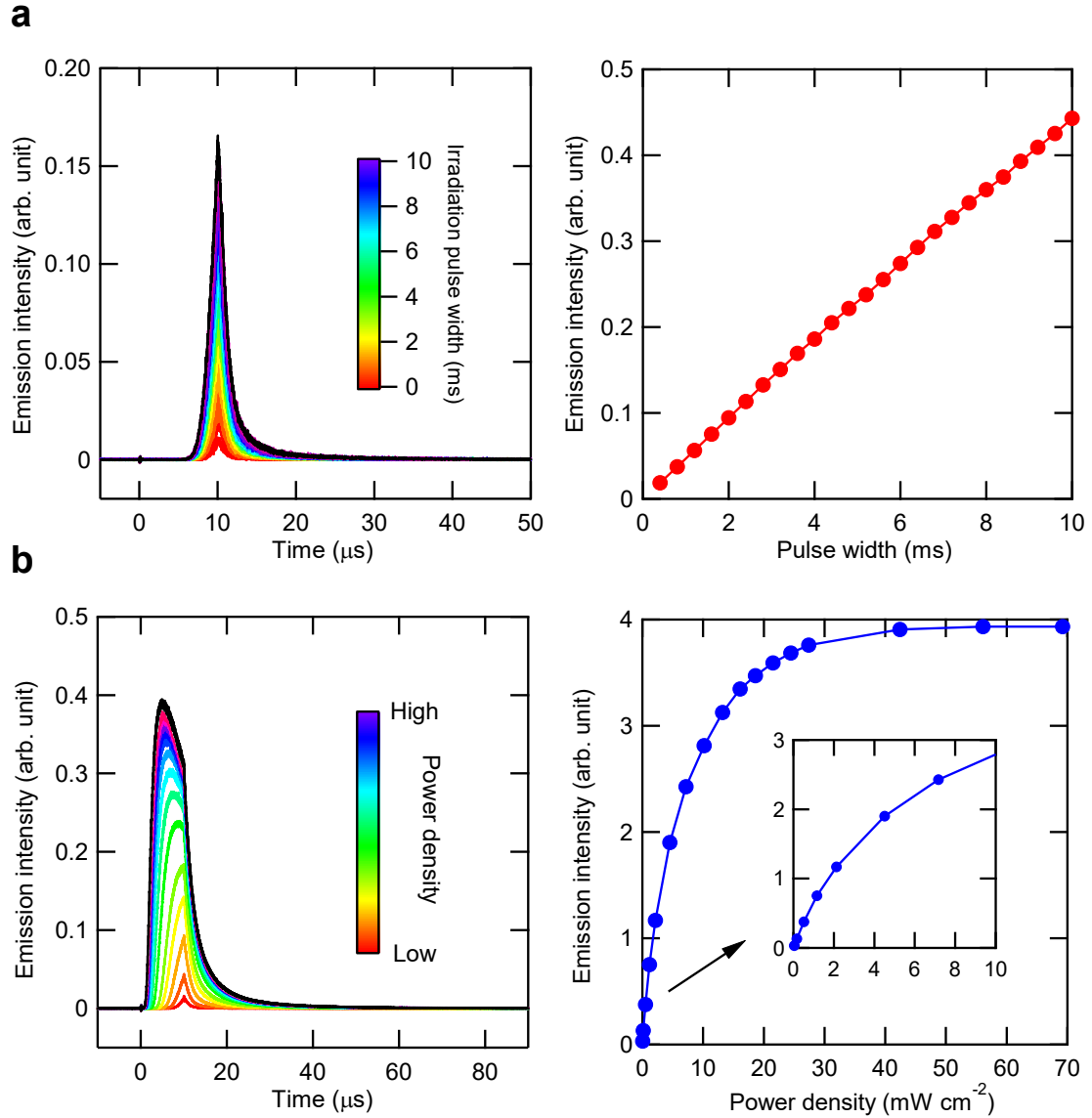


Figure 4-16. EL linearity characterization. **(a)** EL intensity as a function of the irradiation pulse width. The irradiation power density was fixed at $\sim 3 \mu\text{W cm}^{-2}$, which is the same level as the DMD projection. The EL intensity was defined as the integration of the EL pulse from 0 to 40 microseconds. **(b)** EL intensity as a function of power density. The irradiation pulse width was fixed at 400 microseconds, which is the shortest pulse width in the DMD projection. The EL intensity was defined as the integration of the EL pulse from 0 to 80 microseconds. The inset is an enlarged view.

4-2-3. High-speed pulse-driven OLED using charge accumulation

The photo-generated electrons identified in **Section 4-2-1** also have implications for OLED performance. Therefore, we measured the time variation of the EL spectrum in the normal OLED after light irradiation to elucidate how photogenerated electrons affect the EL characteristics. The structure of the normal OLED was the same as that for DCM characterization. As shown in **Figure 4-17a, b**, the EL intensity with driving a constant voltage of 3 V gradually attenuated over several tens of seconds after light irradiation, whereas no change was observed in the device without light irradiation. If the reduction of EL intensity occurred in the constant current driving, it could be attributed to exciton-polaron annihilation. However, the driving current just after light irradiation prominently increased (**Figure 4-17c**) and the EL intensity is proportional to the current density that was measured simultaneously (**Figure 4-17d**). This phenomenon is induced by hole injection for the compensation of the electrons accumulated by light irradiation. Also as discussed in **Section 4-2-1**, the exciton dissociation accelerates instantaneous charge injection (**Figure 4-17e**).

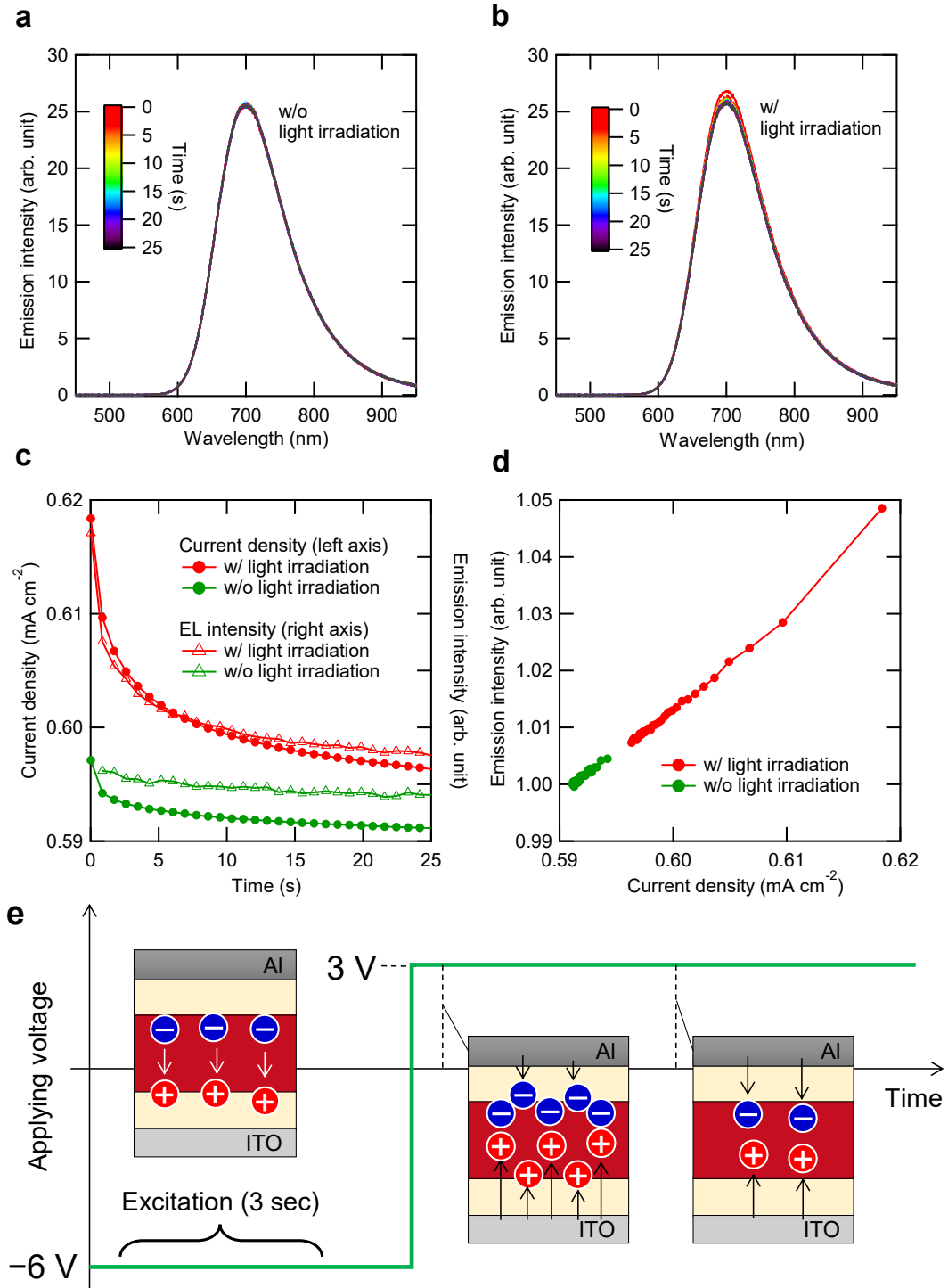


Figure 4-17. Evolution of EL intensity under applying a constant driving voltage of 3 V, after applying an offset voltage of -6 V (a) without light irradiation. (b) with light irradiation. (c) Evolution of current density and EL intensity over time. (d) Current density as a function of EL intensity. (e) Charge carrier dynamics in the EL measurement.

To deepen our understanding of the EL response originating from the recombination between injected holes and accumulated electrons, pulse-driven OLED characteristics were investigated. As presented in **Figure 4-18a**, a steep emission spike was observed when a turn-on voltage of 3 V was applied after light irradiation under an offset voltage of -6 V, while a relatively gradual increase in EL was observed without light irradiation. Photoluminescence from the device under light irradiation decreases when a negative voltage is applied, which is consistent with more radiative excitons of TPA-DCPP dissociating into charge carriers with the bias. Notably, creating a larger number of accumulated charges by lowering the offset voltage during light irradiation or by extending the irradiation time (**Figure 4-18b, c**) led to a larger spike in the EL. In addition, an EL pulse was observed for a turn-on voltage of 0 V (**Figure 4-18d**) owing to the hole injection at applied voltages below V_{th} , as clarified by the DCM characterizations.

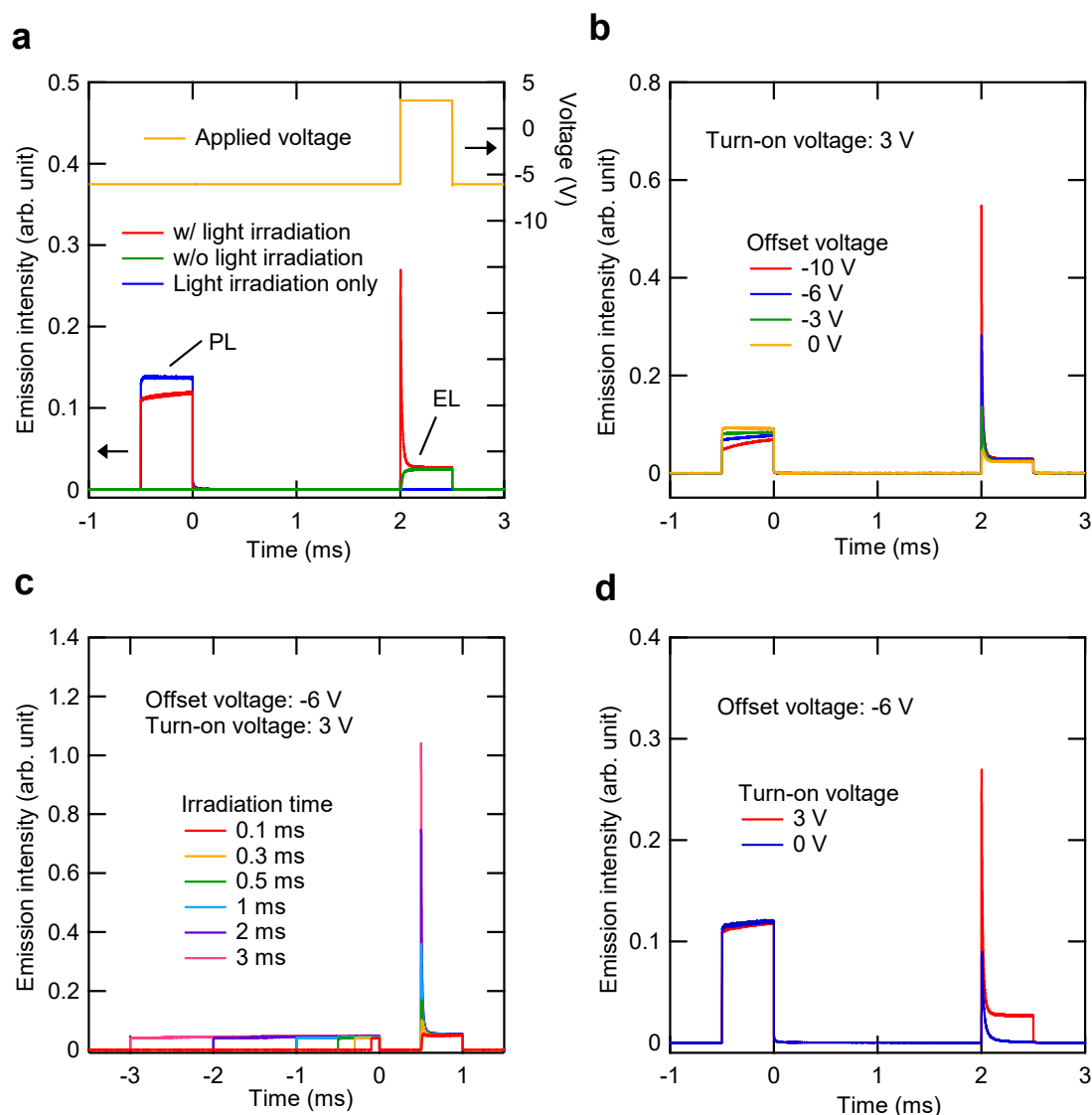


Figure 4-18. Electroluminescence characterization in the pulse-driven OLED. All signals were obtained by averaging 10,000 acquisitions. **(a)** The EL pulse was detected when a turn-on voltage of 3 V was applied to the OLED after 500 microseconds of light irradiation. An offset voltage of -6 V was applied during the light irradiation and hold time continuously until applying the turn-on voltage. The emission appearing in the time region from -0.5 to 0 milliseconds is the PL of the TPA-DCPP emitter excited by the light irradiation. **b–d**, Dependence of the EL pulse intensity on **(b)** offset voltage, **(c)** pulse width of excitation light, **(d)** turn-on voltage.

Figure 4-19 shows the resulting EL when a short voltage pulse of 500 microsecond is applied. The rise time (time required for the response to rise from 10% to 90% of its peak value) and the peak power of the EL pulse were 360 nanoseconds and 2.4 mW cm^{-2} , respectively. The rise time was ~ 107 times faster and the peak power was ~ 27 times greater than those of the resulting EL without light irradiation. Since the hole mobilities of HTLs are typically a few orders of magnitude greater than the electron mobilities of ETLs^{21, 22}, the fast response time of the device can be explained by the high hole mobility of the TAPC layer ($1.0 \times 10^{-2} \text{ cm}^2 \text{ V}^{-1} \text{ s}^{-1}$)²³. Space charge induced by the accumulated electrons reduces the hole injection barrier, resulting in the high-speed and high-power EL pulse. Here, we calculated the EQE for the one-microsecond EL pulse. The net charge was calculated to be -1.7 nC by taking the difference current signal with and without light irradiation (**Figure 4-20a**). Total radiant energy was also calculated to be $5.3 \times 10^{-2} \text{ nJ}$ by integrating the radiant flux with peak power of 0.1 mW (**Figure 4-20b**). Therefore, the EQE defined as a ratio of “the number of photons” to “the number of electrons” was calculated to be 1.75% in this EL pulse. Note that the EQE value under DC driving conditions was 4.0% at radiant flux of 0.1 mW (**Figure 4-20c**), which is higher than that of the pulse EL. However, this value is reasonable because the prompt emission from TPA-DCPP mainly contributes to the short EL pulse and delayed emission after one microsecond is not included in the integration of the radiant flux (**Figure 4-20d**).

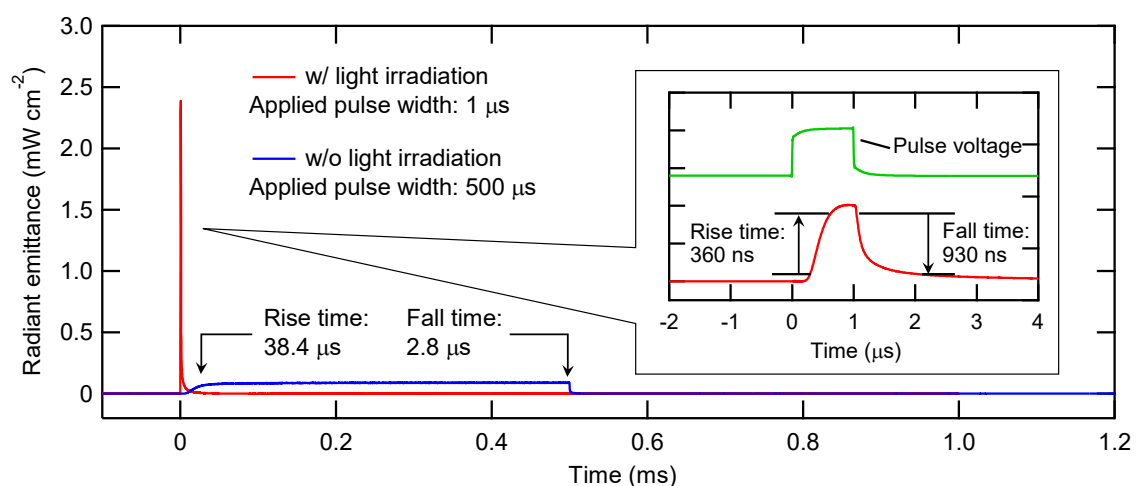


Figure 4-19. Radiant emittance of EL pulse when applying a one-microsecond pulse voltage to the normal OLED. The offset voltage, turn-on voltage, and irradiation time were -6 V, 3 V, and 500 microseconds, respectively. In the measurement without light irradiation, electric pulse width was fixed 500 microseconds to obtain a maximum value of radiant emittance (Due to the low time response of the device).

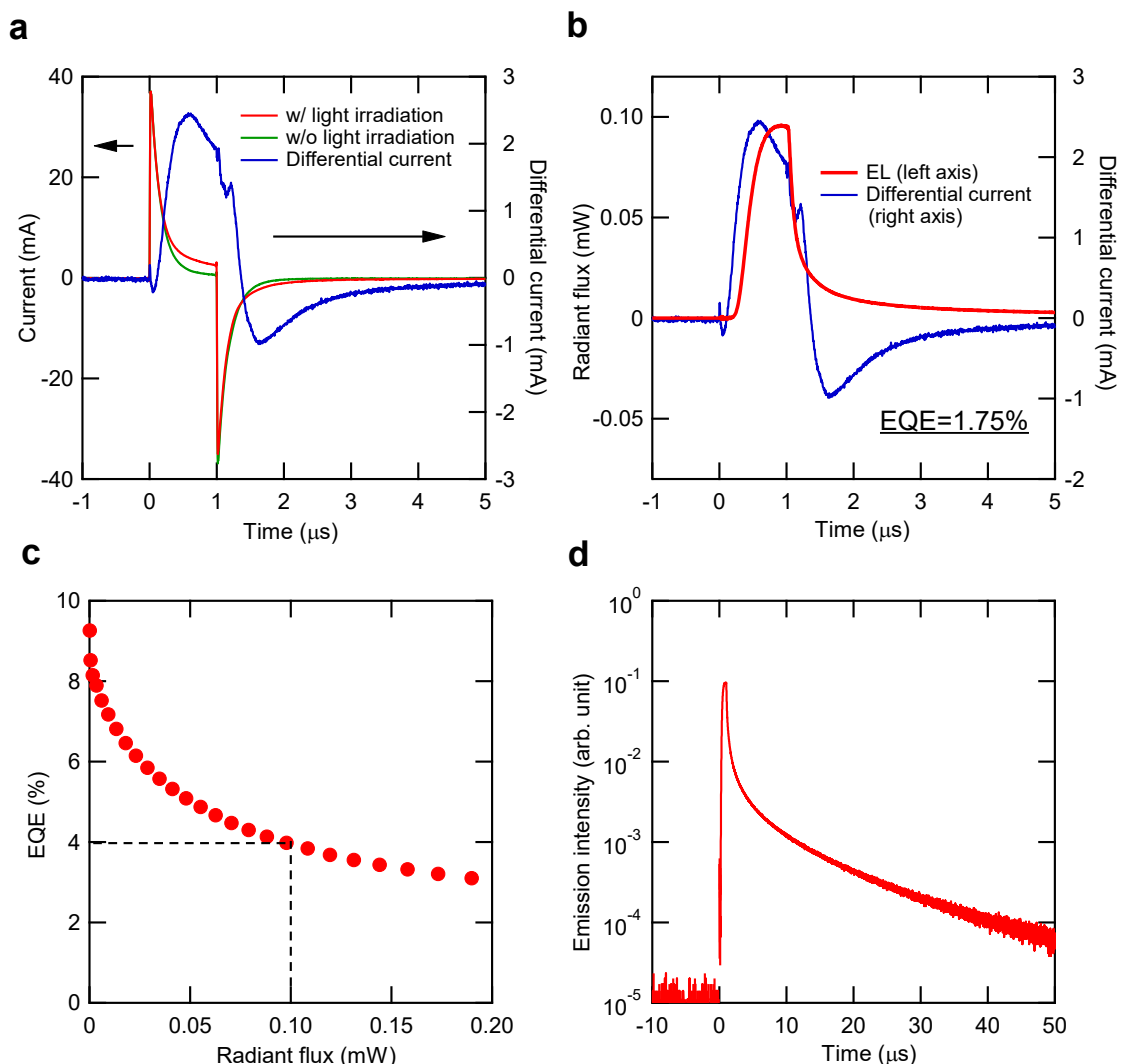


Figure 4-20. Calculation of EQE of the EL pulse originating from the accumulated charge carriers. **(a)** The current signal with (red) and without light irradiation (green). The blue line corresponds to the differential current. The net charge is calculated to be -1.7 nC by integrating the differential current from 0.1 to $1.0 \mu\text{s}$. **(b)** The radiant flux of the EL pulse. Total radiant energy is calculated to be $5.3 \times 10^{-2} \text{ nJ}$ by integrating the radiant flux from 0.1 to $1.0 \mu\text{s}$. **(c)** The EQE-radiant flux characteristic under continuous wave (CW) driving. **(d)** EL pulse plotted on a log scale. The emission tail observed after $10 \mu\text{s}$ is mainly attributed to delayed fluorescence of the TADF emitter, though a small portion of emission based on charge recombination after turning off the pulse voltage is speculated to be included.

4-3. Summary

This study shows that photo-generated charge carriers can survive over one month in an organic solid with SOP even at room temperature. This means that electrons, i.e., radical anions, can be extraordinarily stable even in disordered organic films if recombination processes are suppressed. We also found that the charge carriers retain spatial information with little blurring by visualizing accumulated electrons as EL when they recombine, indicating that electrons diffuse slowly in the plane of the organic layer. By combining these unique features of organic semiconductors, we succeeded in the high-resolution reproduction of photographs in the organics by writing them with irradiation and reading them as EL. Furthermore, we elucidated that the accumulation of optically-generated charge in the OLEDs influenced the OLED performance. As a result, a pulse-driven OLED with high-speed and high-power was demonstrated. We believe that the multifunctional devices combining photo-absorption, charge storage, and EL in the present study open up new possibilities for organic electronics in future imaging-related applications such as thin-film memory devices and storage devices for high-resolution X-ray imaging^{24, 25}.

4-4. Sample preparation and experimental methods

4-4-1. Materials

The molecules dipyrzino[2,3-f :20,30-h]quinoxaline-2,3,6,7,10,11-hexacarbonitrile (HAT-CN), 3,3-di(9H-carbazol-9-yl)biphenyl (mCBP), 7,10-bis(4-(diphenylamino)phenyl)-2,3-dicyanopyrazinophenanthrene (TPA-DCPP), 2,4,6-tris(biphenyl-3-yl)-1,3,5-triazine (T2T), and 2,7-bis(2,2'-bipyridine-5-yl)triphenylene

(BPy-TP2) were purchased from NARD Institute, Ltd. The molecules 1,1-bis[(di-4-tolylamino)phenyl]cyclohexane (TAPC) and 8-hydroxyquinolinolato-lithium (Liq) were purchased from Luminescence Technology Corp.

4-4-2. Sample preparation

All organic layers were formed by thermal evaporation under high-vacuum conditions ($< 10^{-4}$ Pa). The devices were fabricated on cleaned, ITO glass substrates and had effective device areas of 4 mm² or 112.5 mm² (EL imaging devices only) defined by polyimide insulation layer. HAT-CN, TAPC, mCBP, TPA-DCPP, BPy-TP2, and Liq were used as a hole injection material, hole transport material, host material, emitter, electron transport material, and electron injection material, respectively. T2T was used as either a hole or electron blocking material. After depositing aluminum on the organic layer, all the devices were immediately encapsulated with glass lids and epoxy glue in a dry N₂-filled glove box (H₂O > 0.1 ppm, O₂ > 0.1 ppm).

4-4-3. DCM characterization

DCM was conducted using a current input preamplifier (LI-76, NF Corporation), multifunction filter (3611, NF Corporation), oscilloscope (WaveRunner 640Zi, Teledyne Lecroy), and function generator (WaveStation2012, Teledyne Lecroy). In the synchronized DCM and EL measurement, a photosensor module (H10721-01, Hamamatsu Photonics) and an amplifier unit (C11184, Hamamatsu Photonics) were used as a photodetector. All DCM curves were measured with a sweep rate of 100 V s⁻¹ completely shielded from any ambient light. A 470 nm LED (NSPB500AS, Nichia Corporation) was used as the irradiation light source to match with the absorption band of the emitter. The power

density was fixed at 40 mW cm^{-2} .

4-4-4. Pulse-driven EL measurement

EL pulse characterization was conducted using the oscilloscope, function generator, photosensor module, amplifier unit, and excitation LED noted earlier. A long-pass filter with a cut-on wavelength of 635 nm and an optical density of 6 was used for extraction of the sample signal.

4-4-5. EL Imaging

Monochrome imaging was conducted by using a monochrome camera (BFS-U3-13Y3M-C, FLIR) and the function generator noted earlier. The aforementioned LED was driven using another function generator (T3AFG80, Teledyne Lecroy) as an excitation light source. Light irradiation through a USAF 1951 test pattern (Edmund Optics) was conducted for 20 milliseconds with a power density of 40 mW cm^{-2} before applying a 10 microsecond pulse voltage. Exposure time of the camera was adjusted to be 100 microseconds by aligning the timing of the electrical pulse to the device. Monochrome EL images were obtained by averaging 10 shots. For the grayscale imaging, an electron multiplying CCD camera (C9100-23B, Hamamatsu Photonics), a digital micromirror device (DLP2010, TEXAS INSTRUMENTS), a pulse generator (81160A, Agilent), and a function generator (AFG310, Tektronix) were used. The function generator was used as an external trigger source, and the pulse generator was used to drive the excitation LED as noted earlier and apply an electric field to the organic storage device. Light irradiation was conducted by reflecting the LED light on a 2D-arrayed micromirror, in which the pulse width was controlled from 0 to 10 milliseconds by adjusting the duty ratio of the

60-Hz-driven DMD. The offset voltage of the storage device was fixed at -3.3 V, and a turn-on voltage of 6 V was applied 2.4 milliseconds after light irradiation. EM-CCD acquisition was started 1.6 milliseconds after light irradiation, in which dwell time was fixed at 1.67 milliseconds. The grayscale EL images were obtained by averaging $1,000$ shots with maximum gain.

References

1. G. Garcia-Belmonte, A. Munar, E. M. Barea, J. Bisquert, I. Ugarte and R. Pacios, Charge carrier mobility and lifetime of organic bulk heterojunctions analyzed by impedance spectroscopy. *Org. Electron.* **9**, 847-851 (2008).
2. A. Rao, P. C. Y. Chow, S. Gélinas, C. W. Schlenker, C.-Z. Li, H.-L. Yip, A. K. Y. Jen, D. S. Ginger and R. H. Friend, The role of spin in the kinetic control of recombination in organic photovoltaics. *Nature* **500**, 435-439 (2013).
3. A. Classen, C. L. Chochos, L. Lürer, V. G. Gregoriou, J. Wortmann, A. Osvet, K. Forberich, I. McCulloch, T. Heumüller and C. J. Brabec, The role of exciton lifetime for charge generation in organic solar cells at negligible energy-level offsets. *Nat. Energy* **5**, 711-719 (2020).
4. J.-W. Seo, S.-H. Lee and J.-Y. Lee, Improved exciton dissociation and charge transport in energetically cascaded trilayer organic solar cells. *Curr. Appl. Phys.* **17**, 924-930 (2017).
5. J. Kosco, S. Gonzalez-Carrero, C. T. Howells, T. Fei, Y. Dong, R. Sougrat, G. T. Harrison, Y. Firdaus, R. Sheelamantula, B. Purushothaman, F. Moruzzi, W. Xu, L. Zhao, A. Basu, S. De Wolf, T. D. Anthopoulos, J. R. Durrant and I. McCulloch, Generation of long-lived charges in organic semiconductor heterojunction nanoparticles for efficient photocatalytic hydrogen evolution. *Nat. Energy* **7**, 340-351 (2022).
6. T. Yamanaka, H. Nakanotani and C. Adachi, Slow recombination of spontaneously dissociated organic fluorophore excitons. *Nat. Commun.* **10**, 5748 (2019).
7. Y. Ueda, H. Nakanotani, T. Hosokai, Y. Tanaka, H. Hamada, H. Ishii, S. Santo and C. Adachi, Role of Spontaneous Orientational Polarization in Organic Donor–Acceptor Blends for Exciton Binding. *Adv. Opt. Mater.* **8**, 2000896 (2020).

8. J. S. Bangsund, J. R. V. Sambeek, N. M. Concannon and R. J. Holmes, Sub-turn-on exciton quenching due to molecular orientation and polarization in organic light-emitting devices. *Sci. Adv.* **6**, eabb2659 (2020).
9. N. C. Giebink, B. W. D'Andrade, M. S. Weaver, P. B. Mackenzie, J. J. Brown, M. E. Thompson and S. R. Forrest, Intrinsic luminance loss in phosphorescent small-molecule organic light emitting devices due to bimolecular annihilation reactions. *J. Appl. Phys.* **103**, 044509 (2008).
10. R. Kabe and C. Adachi, Organic long persistent luminescence. *Nature* **550**, 384-387 (2017).
11. K. Jinnai, R. Kabe, Z. Lin and C. Adachi, Organic long-persistent luminescence stimulated by visible light in p-type systems based on organic photoredox catalyst dopants. *Nat. Mater.* **21**, 338-344 (2022).
12. T. Yamanaka, H. Nakanotani and C. Adachi, Significant role of spin-triplet state for exciton dissociation in organic solids. *Sci. Adv.* **8**, eabj9188 (2022).
13. Q. Burlingame, C. Coburn, X. Che, A. Panda, Y. Qu and S. R. Forrest, Centimetre-scale electron diffusion in photoactive organic heterostructures. *Nature* **554**, 77-80 (2018).
14. Y. Liu, R. C. I. MacKenzie, B. Xu, Y. Gao, M. Gimeno-Fabra, D. Grant, P. H. M. van Loosdrecht and W. Tian, Organic semiconductors with a charge carrier life time of over 2 hours at room temperature. *J. Mater. Chem. C* **3**, 12260-12266 (2015).
15. Y. Gao, R. C. I. MacKenzie, Y. Liu, B. Xu, P. H. M. van Loosdrecht and W. Tian, Engineering Ultra Long Charge Carrier Lifetimes in Organic Electronic Devices at Room Temperature. *Adv. Mater. Interfaces* **2**, 1400555 (2015).
16. M. Sakurai, R. Kabe, M. Fuki, Z. Lin, K. Jinnai, Y. Kobori, C. Adachi and T. Tachikawa, Organic photostimulated luminescence associated with persistent spin-correlated radical pairs. *Commun. Mater.* **2**, 74 (2021).
17. S. Wang, X. Yan, Z. Cheng, H. Zhang, Y. Liu and Y. Wang, Highly Efficient Near-Infrared Delayed Fluorescence Organic Light Emitting Diodes Using a Phenanthrene-Based Charge-Transfer Compound. *Angew. Chem. Int. Ed.* **54**, 13068-13072 (2015).
18. Y. Noguchi, W. Brütting and H. Ishii, Spontaneous orientation polarization in organic light-emitting diodes. *Jpn. J. Appl. Phys.* **58**, SF0801 (2019).
19. S. Egusa, N. Gemma, A. Miura, K. Mizushima and M. Azuma, Carrier injection characteristics of the metal/organic junctions of organic thin-film devices. *J. Appl. Phys.* **71**, 2042-2044 (1992).

20. Q. Zhang, J. Jiang, Z. Xu, D. Song, B. Qiao, S. Zhao, S. Wageh and A. Al-Ghamdi, The recombination zone adjusted by the gradient doping of TPA-DCPP for efficient and stable deep red organic light emitting diodes. *RSC Adv.* **11**, 24436-24442 (2021).
21. T. Yasuda, Y. Yamaguchi, D.-C. Zou and T. Tsutsui, Carrier Mobilities in Organic Electron Transport Materials Determined from Space Charge Limited Current. *Jpn. J. Appl. Phys.* **41**, 5626-5629 (2002).
22. Br, xe, J. L. das, J. P. Calbert, D. A. d. S. Filho and J. Cornil, Organic Semiconductors: A Theoretical Characterization of the Basic Parameters Governing Charge Transport. *Proc. Natl. Acad. Sci. USA* **99**, 5804-5809 (2002).
23. D. H. Huh, G. W. Kim, G. H. Kim, C. Kulshreshtha and J. H. Kwon, High hole mobility hole transport material for organic light-emitting devices. *Synth. Met.* **180**, 79-84 (2013).
24. T. J. Hajagos, E. Garcia, D. Kishpaugh and Q. Pei, Plastic scintillators based on thermally activated delayed fluorescence dyes. *Nucl. Instrum. Methods Phys. Res., Sect. A* **940**, 185-198 (2019).
25. W. Ma, Y. Su, Q. Zhang, C. Deng, L. Pasquali, W. Zhu, Y. Tian, P. Ran, Z. Chen, G. Yang, G. Liang, T. Liu, H. Zhu, P. Huang, H. Zhong, K. Wang, S. Peng, J. Xia, H. Liu, X. Liu and Y. Yang, Thermally activated delayed fluorescence (TADF) organic molecules for efficient X-ray scintillation and imaging. *Nat. Mater.* **21**, 210-216 (2022).

Chapter 5

Summary

5-1. Summary of this thesis

In this thesis, I focused on the spontaneous exciton dissociation event of CT excitons in a solid-state film based on organic polar materials to unveil the exciton dynamics and the role of excited spin-states.

In **Chapter 2**, I found that a CT exciton formed in a polar fluorophore dissociates spontaneously in a highly doped host-guest film. Charge carriers generated by exciton dissociation diffuse and slowly recombine in the solid-state film due to an internal electric field formed by their own polarization, i.e., SOP. The series of dissociation and recombination processes are observed as LLE and the charge carriers can recombine forcibly by an external electric field modulation. Moreover, the spontaneous dissociation acts as an unignorable quenching process for a polar emitter having a CT excited state in solid-state films.

In **Chapter 3**, a role of the spin-triplet state in an organic molecule with a small ΔE_{ST} for exciton dissociation was discussed. The exciton dissociation was suppressed in a solid-state film including a TADF guest molecule and a triplet scavenging host molecule. The result of an electric-field-modulated TRPL measurement in a triplet-activated film elucidated that the exciton dissociation after the formation of the lowest energy states occurs selectively via the long-lived 3CT_1 and the dissociation probability via 1CT_1 is quite low. Further, prolongation of charge carrier lifetime was suggested in the triplet activated film due to shutting off the DET loss channel, which is equivalent to the back-electron transfer channel in OPVs.

In **Chapter 4**, a novel charge storage device based on the exciton dissociation of CT excitons was demonstrated. The photo-generated charge carrier survived over one month in the device due to interfacial pinning of accumulated electrons by SOP and

suppression of recombination probability by extracting the holes. The charge carriers also retain spatial information over 1,000 seconds even though an active area in the device has no pixelized structure. The result indicates that electron diffusion is quite slow because the in-plane polarization of an emitter is expected to be significantly small. Furthermore, a linear relationship between irradiation power and EL intensity was obtained in addition to the spatial retention. By assembling the charge storage ability, unique gray-scale imaging based on the exciton dissociation of organic semiconducting material was demonstrated.

The findings related to the exciton dissociation not only contribute to the elevation of the OLED and OPV performance, but also open up possibilities for a novel multifunctional device with an organic semiconducting material exhibiting CT excited character in the future.

5-2. Future perspectives

As discussed in this thesis, exciton dissociation behaves as one of the quenching processes for polar TADF emitter used in OLEDs. Therefore, molecular polarity and exciton lifetime should be taken into account for achieving a high-performance OLED. On the other hand, the promotion of dissociation probability and subsequential long-lived charge carriers are a key strategy for improving photon-to-electron conversion efficiency in not only OPVs but also another photo-receiving devices. Also, a deeper understanding of exciton dissociation contributes to an OLPL system because charge separation in the OLPL is inherently the same as that in the TADF emitters except for a type of the CT exciton (i.e., intermolecular or intramolecular). Furthermore, the charge separation and

storage abilities in a solid-state film can realize other applications. For instance, W. Ma et al. demonstrated X-ray imaging using a TADF molecule as a scintillator in a fairly recent past¹, in which a secondary electron generated by high energy radiation ionizes the molecule and a hole-electron pair is formed (**Figure 5-1**). A large population of triplet excited states generated by recombination of the hole-electron pair can contribute to radiative relaxation due to spin-conversion to singlet excited states, resulting in highly effective scintillation. Here in applying the charge storage techniques based on the exciton dissociation, a novel X-ray detector with memory and storage ability would be achieved. The exciton dissociation on CT excitons has the potential to create a future imaging device.

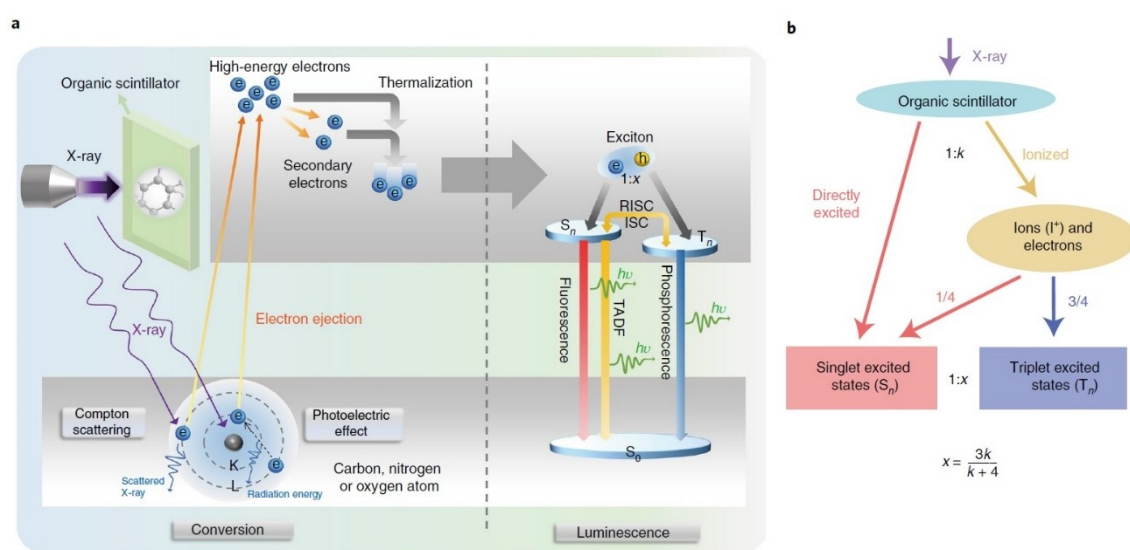


Figure 5-1. Mechanism illustrations and molecular structures of organic scintillators. (a) Schematic mechanism of the X-ray-induced scintillation process in organic scintillators. (b) Production ratio of singlet and triplet excited states in an organic scintillator under X-ray irradiation. (These figures were cited from W. Ma et al., *Nat. Mater.* **21**, 210-216 (2022)¹)

Here, I present future perspectives for an intramolecular CT exciton with high dissociation probability. As elucidated in **Chapter 2** and **Chapter 3**, the internal potential

slope induced by SOP is critical for the spontaneous exciton dissociation. However, the SOP in a host-guest film is determined by many factors such as intrinsic molecular characteristics such as permanent dipole moment, molecular shape, glass transition temperature, deposition rate in preparing the films, and interaction between host and guest molecules^{2, 3}. Indeed, as shown in **Figure 5-2**, the large GSP slope induced by the SOP was obtained in the device including 50-wt%-TPA-DCPP:T2T layer, where the elevation of dissociation probability and a decrement of PLQY are observed. Thus, if a solid-state film with a well-organized permanent dipole moment is achieved, a larger dissociation efficiency must be realized. Also, a comprehensive evaluation with a wide variety of polar emitters exhibiting intramolecular CT excited states is important for obtaining a detailed understanding of the correlation between the exciton dissociation and SOP.

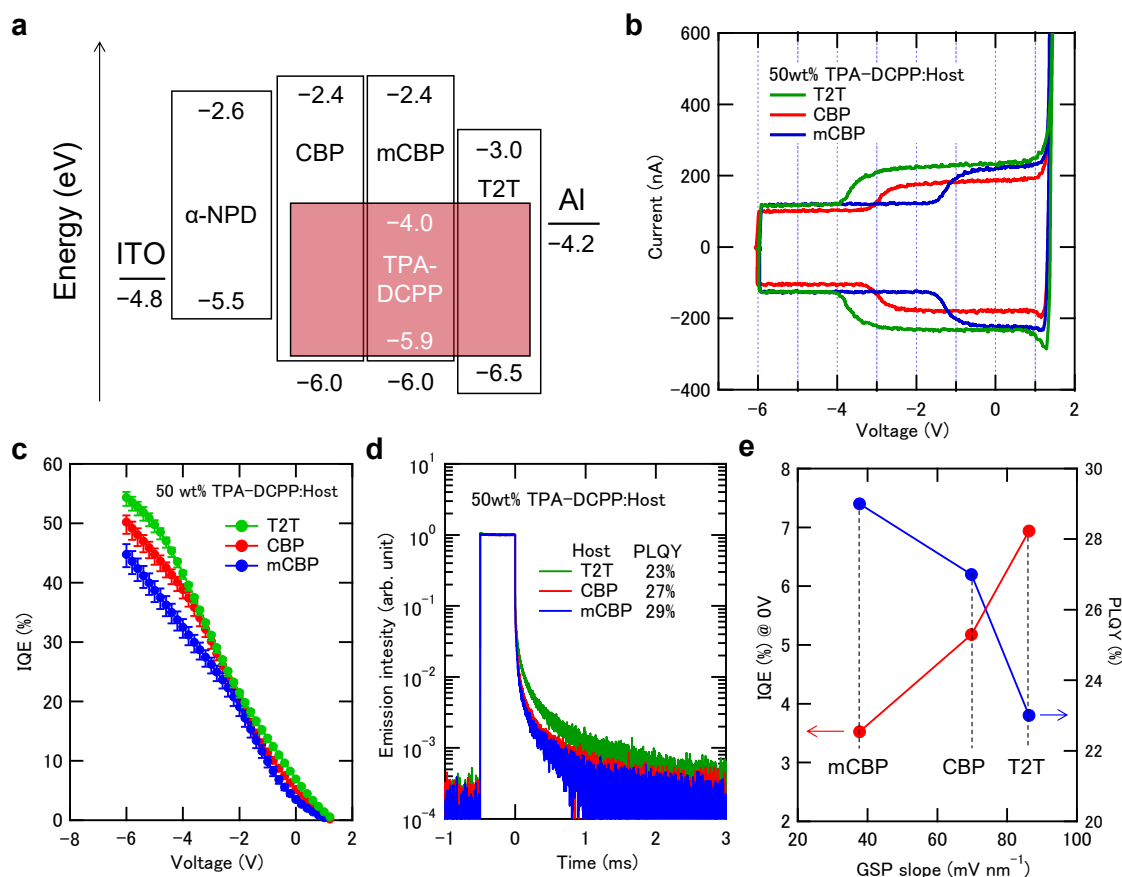


Figure 5-2. Device structure and characterization of exciton dissociation for a TPA-DCPP doped in various host matrices. (a) Energy level diagram of the TPA-DCPP based device. (b) DCM and (c) IQE properties in the device with 50 wt%-TPA-DCPP:Host EML. (d) TRPL in a 50 wt%-TPA-DCPP:Host co-deposited film. (e) Correlation between GSP slope and IQE or PLQY.

Triplet contribution is also important for effective exciton dissociation. As clarified in **Chapter 3**, the exciton dissociation occurs selectively via $^3\text{CT}_1$ after forming the lowest excited state. Therefore, a large k_{ISC} value is desirable since the radiative decay of photogenerated $^1\text{CT}_1$ disturbs the formation of highly dissociable $^3\text{CT}_1$ (**Figure 5-3**). Moreover, the dissociation efficiency is enhanced by extending the lifetime of $^3\text{CT}_1$. In fact, LLE originated from charge carrier recombination is hardly observed in an amorphous 4CzIPN film with a low $^3\text{CT}_1$ population. However, the LLE is drastically

enhanced in a 4CzIPN single crystal in which the $^3\text{CT}_1$ lifetime is significantly larger than the amorphous film (**Figure 5-4**). The increment of dissociation probability in the single crystal seems to include the effect of SOP enhancement due to the ideal molecular orientation. From these viewpoints, a polar TADF emitter with a large population of long-lived $^3\text{CT}_1$, which is unpreferable as an emitter for OLEDs, is suitable for an effective charge photogeneration.

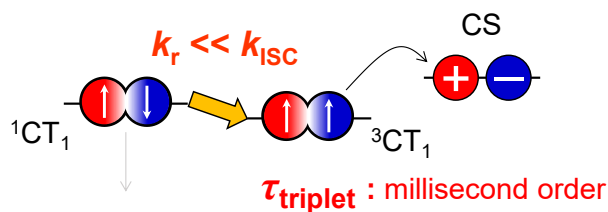


Figure 5-3. Possible photophysical process of CT exciton for its effective dissociation.

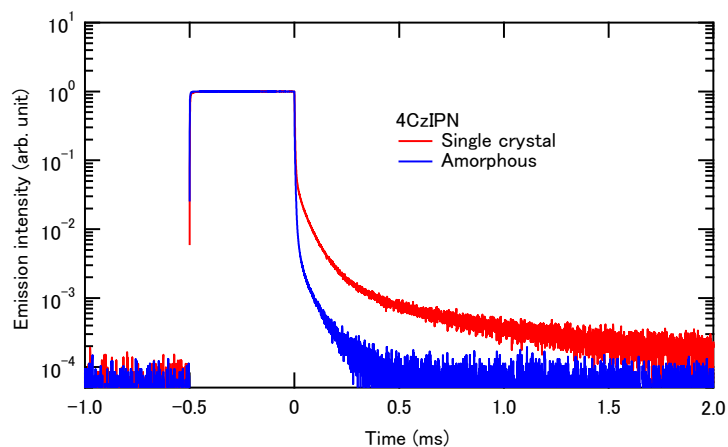


Figure 5-4. TRPL characteristic of amorphous and single crystal 4CzIPN films.

Finally, I mention the remaining study in the dissociation of CT excitons. To obtain a more accurate depiction of the charge carrier dissociation in a solid-state film, the photogenerated radical ion should be analyzed more precisely. Although an IQE measurement can evaluate the number of charge carriers generated in the solid-state film, several problems are incorporated. For example, charge separation occurs not only at the

lowest energy state but also at a higher-lying energy state, i.e., a hot excited state (**Figure 5-5**). Moreover, the charge separation via a multi-photon process would be also included, in which the long-lived triplet excitons in TADF molecules absorb the photons. Therefore, it is difficult to estimate the substantial contribution of relaxed CT states. In this case, direct observation for radical ion dynamics such as transient absorption measurement⁴ or time-resolved photoelectron emission microscopy⁵ would solve the problem. Furthermore, the exciton dissociation corresponds to nonadiabatic electron transfer between two different energy states, indicating that the observation of the activation energy, i.e., characterization of temperature dependence on exciton dissociation, is also a critical experiment to clarify the dissociation mechanism in detail. Additionally, an electric-field-modulated PLQY measurement is also helpful for the quantitative characterization of dissociation efficiency. These characterizations also contribute to achieving a comprehensive understanding of exciton dissociation for not only intramolecular but also intermolecular D-A systems.

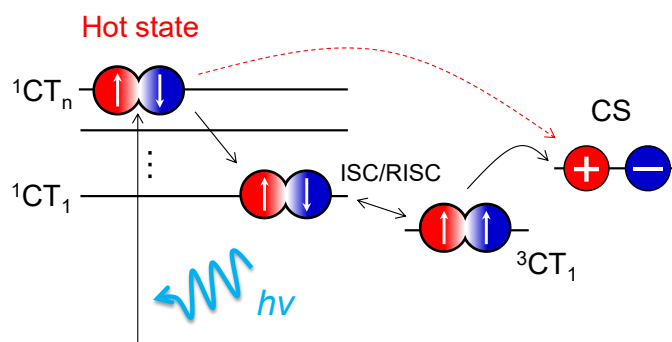


Figure 5-5. Exciton dissociation via a hot excited state.

With further considerations and advanced design of CT excited states, I strongly hope for the realization of organic excitonic devices controlling charge photogeneration, storage, and recombination for future imaging applications.

References

1. W. Ma, Y. Su, Q. Zhang, C. Deng, L. Pasquali, W. Zhu, Y. Tian, P. Ran, Z. Chen, G. Yang, G. Liang, T. Liu, H. Zhu, P. Huang, H. Zhong, K. Wang, S. Peng, J. Xia, H. Liu, X. Liu and Y. Yang, Thermally activated delayed fluorescence (TADF) organic molecules for efficient X-ray scintillation and imaging. *Nat. Mater.* **21**, 210-216 (2022).
2. L. Jäger, T. D. Schmidt and W. Brütting, Manipulation and control of the interfacial polarization in organic light-emitting diodes by dipolar doping. *AIP Adv.* **6**, 095220 (2016).
3. M. Tanaka, H. Noda, H. Nakanotani and C. Adachi, Molecular orientation of disk-shaped small molecules exhibiting thermally activated delayed fluorescence in host–guest films. *Appl. Phys. Lett.* **116**, 023302 (2020).
4. Y. Ueda, H. Nakanotani, T. Hosokai, Y. Tanaka, H. Hamada, H. Ishii, S. Santo and C. Adachi, Role of Spontaneous Orientational Polarization in Organic Donor–Acceptor Blends for Exciton Binding. *Adv. Opt. Mater.* **8**, 2000896 (2020).
5. Y. Fukami, M. Iwasawa, M. Sasaki, T. Hosokai, H. Nakanotani, C. Adachi, K. Fukumoto and Y. Yamada, Direct Observation of Photoexcited Electron Dynamics in Organic Solids Exhibiting Thermally Activated Delayed Fluorescence via Time-Resolved Photoelectron Emission Microscopy. *Adv. Opt. Mater.* **9**, (2021).

Appendix

TPA-DCPP: 7,10-bis(4-(diphenylamino)phenyl)-2,3-dicyanopyrazinophenanthrene

CBP: 4'-bis(carbazol-9-yl) biphenyl

T2T: 2,4,6-tris(biphenyl-3-yl)-1,3,5-triazine

HAT-CN: dipyrazino[2,3-f :20,30-h]quinoxaline-2,3,6,7,10,11-hexacarbonitrile

TAPC: 1,1-bis[(di-4-tolylamino)phenyl]cyclohexane

Bpy-TP2: 2,7-bis(2,2'-bipyridine-5-yl)triphenylene

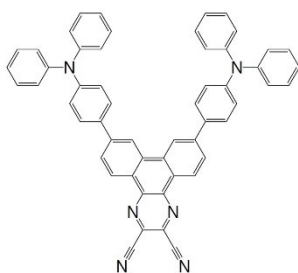
TBRb: 2,8-di-tert-butyl-5,11-bis(4-tert-butylphenyl)-6,12-diphenyltetracene

4CzIPN: 2,4,5,6-tetra(9Hcarbazol-9-yl)iso-phthalonitrile

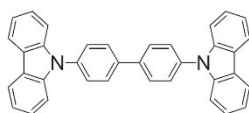
4CzTPN: 1,2,4,5-tetrakis(carbazol-9-yl)-3,6-dicyanobenzene

ADN: 9,10-bis(2-naphthyl)anthracene

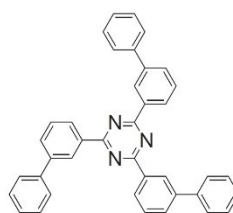
mCBP: 3,3-di(9H-carbazol-9-yl)biphenyl



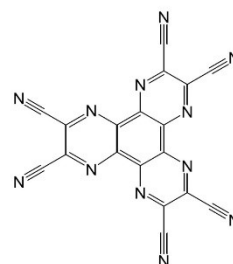
TPA-DCPP



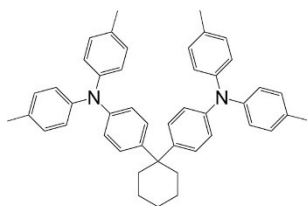
CBP



T2T



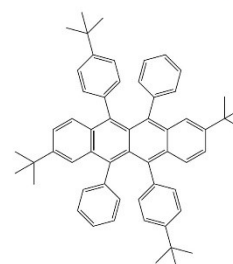
HAT-CN



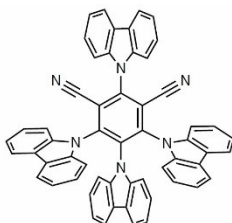
TAPC



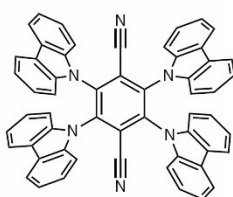
BPy-TP2



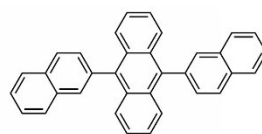
TBRb



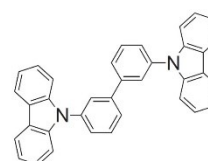
4CzIPN



4CzTPN



ADN



mCBP

Publication lists

- 1) **Takahiko Yamanaka**, Hajime Nakanotani, Shigeo Hara, Toru Hirohata, Chihaya Adachi, Near-infrared organic light-emitting diodes for biosensing with high operating stability. *Applied Physics Express* **10**, 074101 (2017). *Not described in this thesis.
- 2) **Takahiko Yamanaka**, Hajime Nakanotani, Chihaya Adachi, Slow recombination of spontaneously dissociated organic fluorophore excitons. *Nature Communications* **10**, 5748 (2019).
- 3) **Takahiko Yamanaka**, Hajime Nakanotani, Chihaya Adachi, Significant role of spin-triplet state for exciton dissociation in organic solids. *Science Advances* **8**, eabj9188 (2022).
- 4) **Takahiko Yamanaka**, Hajime Nakanotani, Katsuhiko Nakamoto, Chihaya Adachi, Electron lifetime of over one month in disordered organic solid-state films (Submitted).

Acknowledgements

The studies in this thesis were carried out at Adachi laboratory, Department of Chemistry and Biochemistry, Graduate School of Kyushu University from 2019-2022.

I am deeply grateful to Professor Chihaya Adachi for supervising this thesis, excellent experimental environment, helpful discussion, and advise for all of my works. I would also deeply grateful to Professor Ken Onda and Professor Noritada Kaji for co-supervising of this thesis. I would also like to appreciate Associate Professor Hajime Nakanotani for the discussion on exciton dissociation, insightful comments, and help in preparing this thesis.

I would like to acknowledge Mr. Yuuhi Ueda and Shintaro Kohata for the sample preparation in **Chapter 3**, and Mr. Katsuhiro Nakamoto for performing and analyzing an EL imaging in **Chapter 4**. I also appreciate Dr. William J. Potscavage Jr. for his assistance with preparing my paper in **Chapter 2** and **Chapter 4**. I would like to thank Dr. Toru Hirohata and Dr. Shigeo Hara for helpful discussion in **Chapter 2** and supporting my research activity.

I acknowledge Assistant Professor Masashi Mamada for giving me expert advice, and Dr. Ryo Nagata for sharing the condition of the experimental equipment. Ms. Keiko Kusuhara and Ms. Nozomi Nakamura also help in the synthesis and characterization of chemical compounds. I would like to thank Ms. Sachiko Higashikawa and other secretaries for kindly supporting my Ph. D. course. I also appreciate all the members of the Adachi Laboratory, the central research laboratory in Hamamatsu Photonics K.K., and all persons I met through my work for their support not only for my work but also for my daily life.

Finally, I would like to express my gratitude to my family for their moral support

and warm encouragement.

July, 2022

Takahiko Yamanaka